Localizing interseismic deformation around locked strike-slip faults

by

Yijie Zhu
B.Sc., University of Science and Technology of China, 2017

A Thesis Submitted in Partial Fulfillment
of the Requirements for the Degree of

MASTER OF SCIENCE

in the School of Earth and Ocean Sciences

Supervisory Committee

Localizing interseismic deformation around locked strike-slip faults

by

Yijie Zhu
B.Sc., University of Science and Technology of China, 2017

Supervisory Committee

Dr. Kelin Wang (School of Earth and Ocean Sciences)
Supervisor

Dr. Edwin Nissen (School of Earth and Ocean Sciences)
Co-Supervisor

Dr. Stan Dosso (School of Earth and Ocean Sciences)
Departmental Member

Abstract

Localized geodetic deformation of an approximately arctangent shape around locked strike-slip faults is widely reported, but there are also important exceptions showing distributed interseismic deformation. Understanding the controlling mechanism is important to the interpretation of geodetic observations for hazard assessment and geodynamic analysis. In this thesis, I use simple finite element models to separately study the two major contributors to the deformation: far-field loading and previous earthquakes. The models feature a vertical strike-slip fault in an elastic layer overlying a viscoelastic substrate of Maxwell or Burgers rheology, with or without weaknesses representing extensions of the fault either along strike or to greater depth. If the locked fault is loaded only from the far field without the effects of previous earthquakes, localized deformation occurs only if local mechanical weaknesses below the fault and/or somewhere along strike are introduced. I first show that the effects of far-field loading are rather limited even in the presence of extreme weaknesses. Then I use idealized earthquake cycle models to investigate the effects of past seismic events in a viscoelastic Earth. I demonstrate that, after a phase of fast postseismic deformation just after the earthquake, the localization of interseismic deformation is controlled mainly by the recurrence interval of past earthquakes. Given viscosity, shorter recurrence leads to greater interseismic localization, regardless of the rheological model used. The presence of a low-viscosity deep fault zone does not change this conclusion, although it tends to lessen localization by promoting faster postseismic stress relaxation. Distributed interseismic deformation, although less reported in the literature, is a natural consequence of very long recurrence and in theory should be as common as localized deformation. The apparent propensity of the latter is likely associated with the much greater quantity and better quality of geodetic observations from higher-rate and shorter-recurrence faults. Using viscoelastic earthquake-cycle models, I also explore the role of nearby earthquakes and creeping segments along the same fault. For faults of relatively short recurrence, frequent ruptures of nearby segments, modelled using a migrating rupture sequence with or without temporal clustering, further enhance localization. For faults of very long recurrence, faster near-fault deformation induced by a recent earthquake may give a false impression of localized interseismic deformation.

Table of Contents

List of Tables

List of Figures

List of Variables

Symbol	Definition	Unit
D	Locking depth	km
D_G	Geodetic locking depth	km
F	Fault-parallel boundary distance	km
H	Thickness of the elastic top layer	km
L	Fault length	km
L_C	Length of the creeping segment	km
t	Time since last earthquake	yr
T	Recurrence interval between earthquakes	yr
T_m	Migration interval between nearby earthquakes	yr
U	Fault-parallel displacement	m
U_o	Coseismic slip	m
U_2	Fault-parallel displacement caused by a single earthquake	m
V	Fault-parallel velocity	mm yr^{-1}
V_o	Fault strike-slip rate	mm yr^{-1}
V_{o_1}	V_o of the $T = \tau_M$ model	mm yr^{-1}
V_{o2}	Fault-normal rate	mm yr^{-1}
V_1	Fault-parallel velocity caused by far-field loading	mm yr^{-1}
V_2	Fault-parallel velocity caused by a single earthquake	mm yr^{-1}
W	Width of the weak zone or shear zone	km
x	Distance to fault	km
y	Along-strike distance	km
z	Depth	km
σ	Shear stress	Pa
$\dot{\sigma}$	Shear stress rate	Pa
μ_M	Rigidity (shear modulus) of Maxwell body	Pa
μ_K	Rigidity (shear modulus) of Kelvin body	Pa
ε_E	Elastic shear strain	-
$\dot{\varepsilon}_E$	Elastic shear strain rate	s^{-1}
$\dot{\varepsilon}_V$	Viscous shear strain rate	s^{-1}
$\dot{\varepsilon}$	Total shear strain rate	s^{-1}
η_M	Maxwell viscosity	Pa s
η_K	Kelvin viscosity	Pa s
η_{eff}	Effective viscosity	Pa s
τ_M	Maxwell relaxation time ($= \eta_M/\mu_M$)	yr
τ_K	Kelvin relaxation time ($= \eta_K/\mu_K$)	yr

Acknowledgments

I would like to thank all the people whose help made this thesis possible. Sincere thanks go to the Pacific Geoscience Centre (PGC), Geological Survey of Canada, for providing workspace and equipment for research, and to PGC colleagues for sharing their knowledge.

I would like to express my deepest appreciation to my supervisor, **Kelin Wang**, for his support, guidance, and patience throughout the project. His wealth of knowledge and passion for science always inspire me, and his insightful suggestions and kindness in reviewing and editing drafts are the most essential in bringing this work to a conclusion.

I thank my co-supervisor, **Edwin Nissen**, for his advice and help. His knowledge of global geology and geodesy provided solid contribution to this research. Special thanks go to my committee member **Stan Dosso**, and my external examiner, **Yajing Liu**, for their encouragement and suggestions.

Professor **Xueze Wen** of China Earthquake Administration led us to inspect the Xianshuihe Fault in eastern Tibetan plateau at the early stage of my MSc study. **Jiangheng He** developed the 3-D finite element mechanical modelling code PGCvesph and provided invaluable guidance in resolving technical problems. **Taizi Huang** developed a MATLAB code for an analytical solution that was used in the work described in Chapter 2. **Xin Zhou** provided timely support in benchmarking against analytical solutions. **Jianling Cao** did initial work on elastic models discussed in Chapter 3. I also thank **Yan Jiang** for sharing his knowledge of Global Navigational Satellite System (GNSS) and taking me to the field, **Haipeng Luo** for discussions on the use of PGCvesph, **Honn Kao** for suggestions on explaining modelling results, and **Yuji Ito** for recommending literature of related studies.

I gratefully acknowledge the help and encouragement from other friends and colleagues, such as **Dawei Gao**, **Matthew Sypus**, **Dong Man**, **Yuxuan Chen**, **Zeyu Jin**, **Bingrui Shi**, **Xiang Huang** and **Sen Li**.

Above all, I thank my parents **Naiyue Hong** and **Hongbing Zhu** and my girlfriend **Siyu Wang**, for their unwavering love, encouragement, and support.

Chapter 1. Introduction

1.1. Background

Strike-slip faults are commonly found on Earth, from fast-moving plate boundaries to relatively stable intra-plate areas. Different from subduction megathrusts that generate great earthquakes and tsunami that only threaten coastal cities at active continental margins, continental strike-slip faults can be very close to inland cities and can cause destructive earthquakes in many populated areas (Thatcher, 1975;Sylvester, 1988; Barka, 1999). Understanding how elastic strain is accumulated around a strike-slip fault during the interseismic period and at what rate is important to the assessment of the earthquake potential of the fault (Savage and Burford, 1973; Savage and Prescott, 1978a; Cohen and Kramer, 1984; Li and Rice, 1987; Meade et al., 2013; Wright et al., 2013; Vernant, 2015). Geological studies, including paleoseismic and geomorphological studies, can help constrain the long-term rate (V_o) of a fault over geological timescales (e.g., Molnar and Dayem, 2010). To understand interseismic strain accumulation, observations of contemporary deformation are required.

The contemporary interseismic strain field near strike-slip faults are measured mainly with geodetic methods. For the numerous strike-slip faults located in continental areas, the strain field around them can be delineated by Global Navigation Satellite System (GNSS) observations. Interferometric synthetic aperture radar (InSAR) line of sight (LOS) data or other types of geodetic observations such as triangulation and levelling can also help constrain the strain field, but they usually do not offer the spatiotemporal resolution required in this MSc study. Examples of the GNSS observations will be shown in Section 1.2.

For the purpose of understanding the fundamental physical process, we can consider a highly simplified system as shown in Figure 1.1 with a vertical strike-slip fault embedded in a laterally homogeneous, flat, elastic or viscoelastic Earth, although I will also discuss non-vertical faults later in the thesis. Ignoring complexities such as heterogeneous rock material and non-vertical and non-planar fault geometry helps us focus on the first-order process. Simple models of this type have met great success in

explaining surface deformation around real strike-slip faults. Knowledge learned by modelling such simple mechanical systems can provide guidance for the study of more complex systems of the real world.

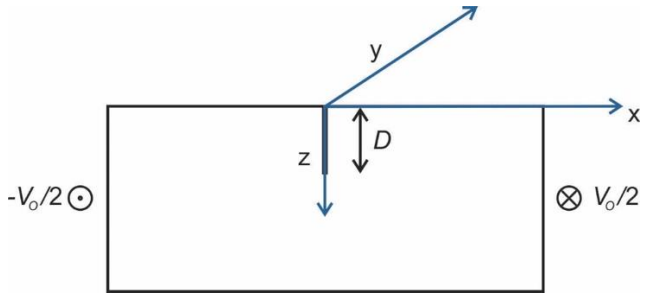

Figure 1.1. Schematic cross-section view of a highly simplified strike-slip fault. The locked strike-slip fault is shown using a thick black bar in the centre of the cross-section. The coordinate system applied is a left-hand coordinate system, where $\boldsymbol{x}$ denotes the fault normal direction, $\boldsymbol{y}$ denotes along-strike direction and $\boldsymbol{z}$ denotes vertically downward direction. $\boldsymbol{V_o}$ is the geological rate of relative motion of the two sides of the fault.

1.2. Interseismic Geodetic Observations Around Strike-slip Faults

Interseismic geodetic observations around locked large strike-slip faults reported in the literature often share a similar pattern of deformation as shown in Figure 1.2a. Along a profile perpendicular to the trace of the strike-slip fault, there is often a steep gradient of fault-parallel velocity near the fault, but it quickly diminishes as we move away from the fault. This is what we call the localization of deformation (Figure 1.2b). This pattern of localized deformation is widely reported for many major strike-slip faults. Near the San Andreas Fault (SAF) in California, where massive geodetic observations are available, localization of deformation is reported along different segments in many studies (e.g., Smith-Konter et al., 2011; Zeng and Shen, 2014; Bacques et al., 2018). Similar localized deformation is observed around the North Anatolian Fault (NAF) in Turkey (Reilinger et al., 2006; Tatar et al., 2012; Hussain et al., 2018), the Xianshuihe Fault (XSH) in Southwestern China (Shen et al., 05; Zheng et al., 2017; Wang and Shen, 2020), the Dead Sea Fault (DSF) in Israel and Jordan (Tarazi et al., 2011; Sadeh et al., 2012; Hamiel et al., 2018) and many other well monitored strike-slip faults (Jolivet et al., 08; Li et al., 2015). Vernant compiled GNSS velocities across many of these faults as

shown in Figure 1.3a. It is important to note that all the faults mentioned above have rather fast slip rates, some of which are summarized in Table 1.1, a characteristic that will be frequently visited in this thesis.

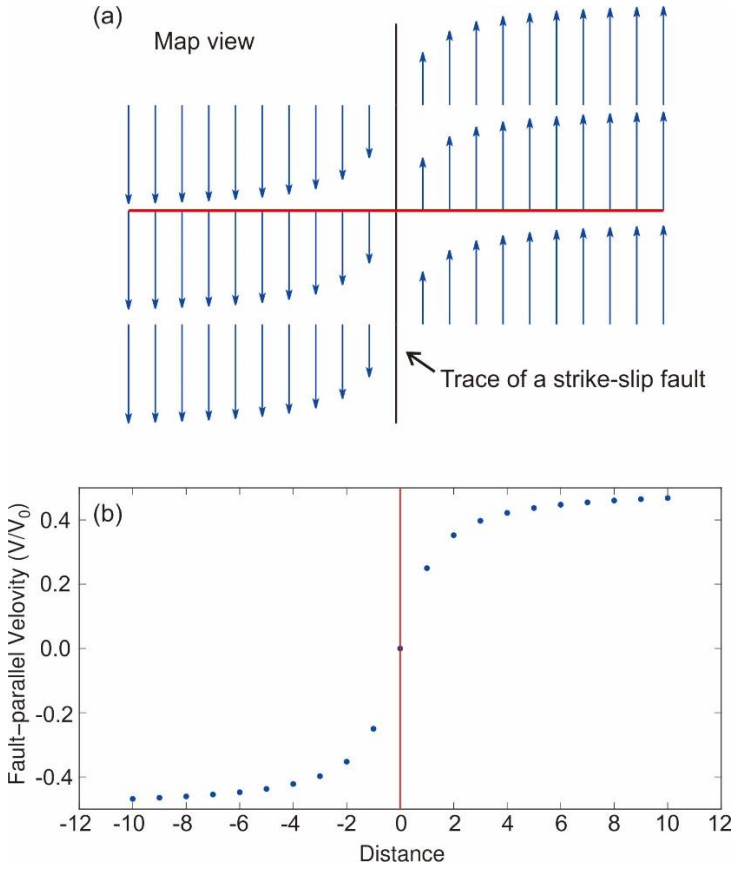

Figure 1.2. An illustration of localized deformation. (a) Map view of deformation around a locked strike-slip fault where localization of deformation is occurring. Blue arrows represent the velocity of surface deformation. (b) Fault-parallel velocities along the red line in (a).

Table 1.1. Slip rates of some strike-slip faults. Values of slip rates which are not from Vernant (2015) are specified with their own references.

Fault name	Geological slip rate (mm/yr)	Geodetic slip rate (mm/yr)	Localization of interseismic deformation
San Andreas Fault (Carrizo segment)	34	36.9	Yes
North Anatolian Fault	~20	26.4	Yes
East Anatolian Fault	8.85	8.8	Yes
Dead Sea Fault	4.7-5.1 (Ferry et al., 2007)	4.8	Yes
Xianshuihe Fault	15 (Allen et al., 1999)	11 (Wang et al., 2009)	Yes
Altyn Tagh Fault	9.4	9	Yes
Tanlu Fault	2.2-2.6 (Jiang et al., 2017)	-	No
Longmenshan Fault*	1 (Ma et al., 2005)	0.5 (Zheng et al., 2017)	No

* The Longmenshan Fault is in fact an oblique fault. The slip rates shown here are its strike-slip component.

The localization of interseismic deformation mentioned above is commonly interpreted using a model of screw dislocation (Savage and Burford, 1973). The model features an infinitely long (two-dimensional, 2-D) vertical strike-slip fault embedded in a uniform elastic half-space (Figure 1.4). The fault is locked from the surface to depth D and is loaded by a constant screw dislocation just below D that has the same rate as the geological slip rate V_o. For the 2-D fault, surface deformation is uniform along strike. The analytical solution for the fault-parallel surface velocity V as a function of distance x is:

$$V = \frac{V_o}{\pi} \arctan \frac{x}{D} \tag{1.1}$$

It is a common practice to derive the two parameters V_o and D by fitting equation (1.1) to geodetic observations. The value of D derived this way is referred to as the geodetic locking depth, which in this thesis is denoted D_G. Both V_o and D are important to hazard assessment because they control recurrence behaviour and rupture dimension. For example, Wright et al. (2013) estimated an average D_G = 14 km based on global observations by fitting geodetically observed velocities to equation (1.1). Vernant (2015)

similarly derived the values of D_G for the faults shown in Figure 1.3, as listed in Figure 1.3b. If the velocities are normalized by each fault's V_o and distances by D_G, the same function applies to observations around all these faults (Figure 1.3b). Despite the unresolved problems discussed in the following, the simple elastic dislocation model has met great success in interpreting geodetic observations.

Nonetheless, not all reported interseismic deformation around locked strike-slip faults show the same pattern of localization. There are rare exceptions in the literature that show little or no localization. Two examples are particularly worth showing. One of them is the dextral Tancheng-Lujiang fault (TLF) system, which is a major geological structure in eastern China accommodating a geological rate of $V_o = 2.2$~2.6 mm/yr (Jiang et al., 2017). Figure 1.5 shows two segments of the TLF separated by the Bohai Sea. The northern segment is called the Yilan-Yitong fault. The southern segment is called the Yishu fault, and it hosted a large earthquake in 1668 that is widely, but questionably, reported to have a magnitude 8.5. The GNSS measurements shown in Figure 1.5 consist of data collected under a number of Chinese national projects through multiple campaign surveys during 1995–2008, 1999–2015, and 2009–2015 and many continuous measurements from 1999 or 2009 to 2016 (Wang and Shen, 2020). The 6 to 17 yr observation time spans allow reasonable determination of velocities despite relatively large measurement errors.

Figures 1.5b and 1.5c show fault-parallel velocity profiles across the two segments of TLF derived by Wang and Shen (2020) from GNSS data. For the Yilan-Yitong segment, there is hardly any sign of deformation localization. For the Yishu segment, there are some fluctuations of fault-parallel velocities but mostly within measurement errors. Some of the secondary deformation signals for the Yishu segment may be related to the 1668 earthquake which will be discussed in **Chapter 5**.

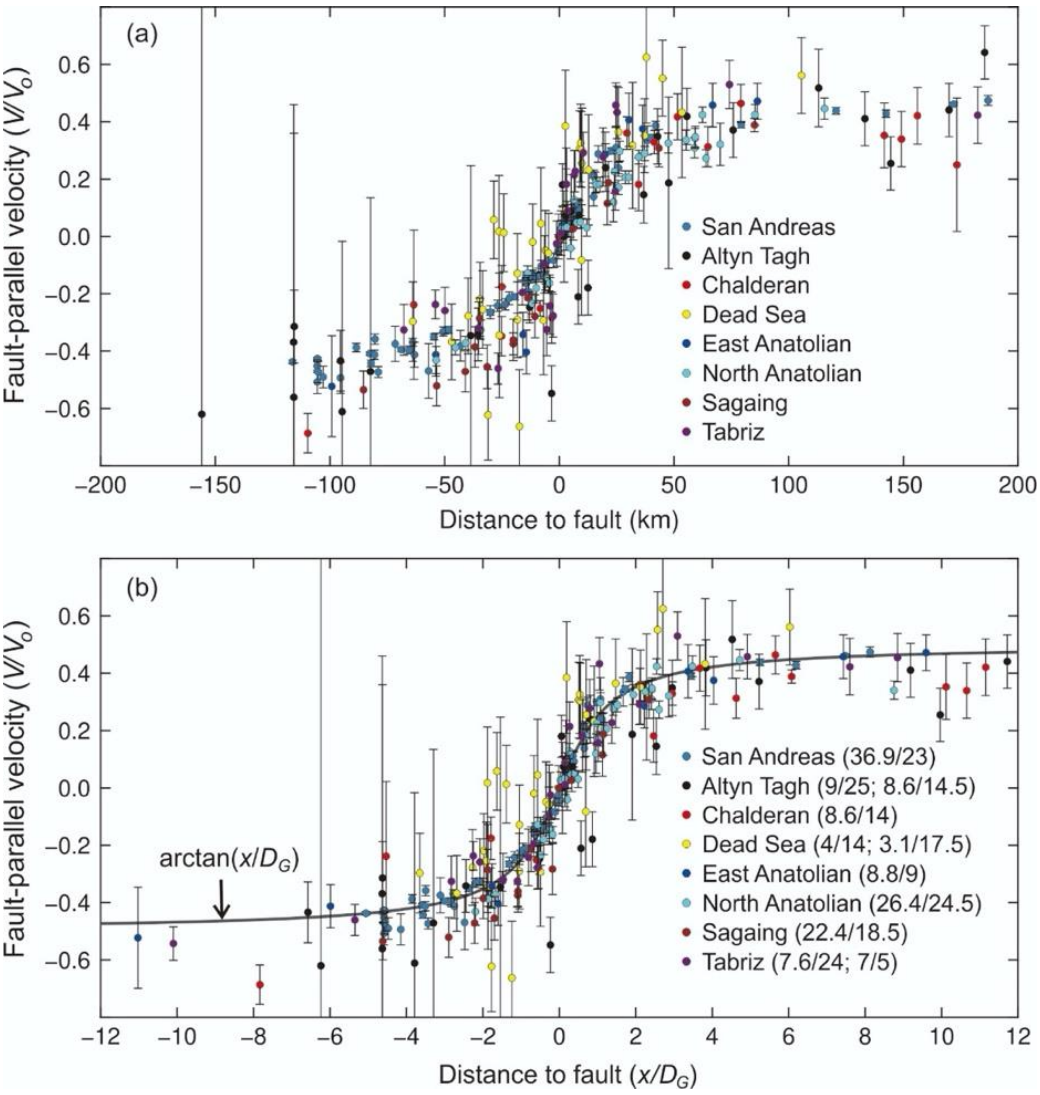

Figure 1.3. Geodetically observed deformation around locked strike-slip faults compiled by Vernant (2015). (a) Strike-parallel velocities vs. fault-normal distances. The velocities are normalized by the geological slip rate V_o of each fault. The Sumatra Fault was included in the original compilation but is not shown here, because its data and model have since been substantially revised (Bradley et al., 2017). All the faults are displayed as left-lateral, although some are actually right-lateral. (b) The same as (a) but with distances normalized by D_G of each fault that was derived by Vernant (2015) by fitting the elastic dislocation model (gray curve) to the data (equation (1.1)). In the legend, the values of V_o and D_G for each fault are shown in parentheses after the fault name in mm/yr and km, respectively. Some have two sets of values because two segments of the same fault are included in the compilation (with the same colour code).

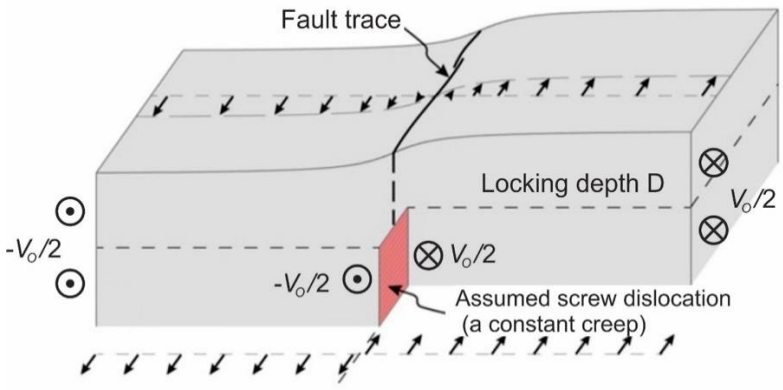

Figure 1.4. Schematic view of the elastic dislocation model (Savage and Burford, 1973), modified from Vernant (2015). The fault is locked from the surface to depth $\boldsymbol{D}$. Half of the geological slip rate ($\boldsymbol{V_o/2}$) is applied at distant boundaries and a screw dislocation with the same rate is applied beneath $\boldsymbol{D}$.

Another potentially relevant example is the Longmenshan Fault zone (LFZ) in southwestern China between the Sichuan Basin and the Tibetan Plateau (Figure 1.6a). It is an oblique fault that exhibits both thrust and dextral motion and produced the 2008 Mw 7.9 Wenchuan earthquake. Geological studies yielded a low strike-slip rate of ~1.0 mm/yr and a thrust rate less than 3.0 mm/yr (e.g., Ma et al., 2005). Here, for discussion purpose, I only focus on the strike-slip component, although I will later (Section 5.2) show models including the thrust component as well. GNSS observations around the LFZ before the 2008 earthquake showed no signal of localized deformation (e.g., Gan et al., 2007; Wang et al., 2015), causing the scientific community to overlook the potential of a devastating earthquake (Chen and Wang, 2010). Figure 1.6 shows better quality GNSS data more recently provided by Wang and Shen (2020). In addition to measurements under the same national projects over the same observation time spans as those shown in Figure 1.5, the GNSS measurements in Figure 1.6 contain more regional continuous sites from 2004 or 2010 to 2016. As detailed by Wang and Shen (2020), these data have been corrected for the effects of recent great earthquakes, including the 2008 Wenchuan event, and therefore the deformation field can be regarded to reflect late-interseismic formation before the 2008 earthquake. Figure 1.6b shows fault-parallel velocities across the LFZ. The area west of the fault is seriously influenced by permanent deformation associated with another fault system parallel to LFZ (Wang and Shen, 2020) and should be excluded

from this discussion. The area east of the fault is the stable Sichuan Basin and better represents elastic interseismic deformation associated with the LFZ. Unfortunately, because of the extremely low slip rate, the GNSS data cannot distinguish between localized or distributed deformation, consistent with what was reported before the 2008 earthquake.

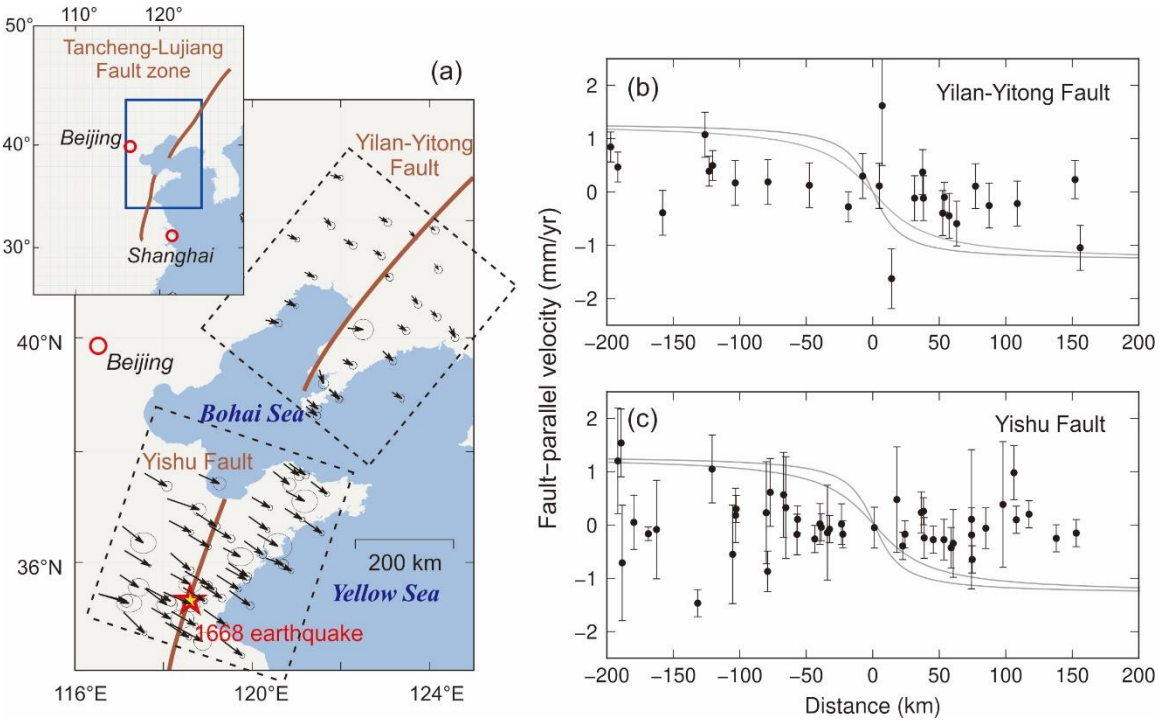

Figure 1.5. GNSS observations over various time periods during 1998–2015 around the Yilan-Yitong and Yishu faults. (a) Map view of the simplified fault trace and GNSS velocities. Multiple parallel strands, likely associated with flower structures, are not shown here. Inset shows the location of the map area and the Tancheng-Lujiang dextral fault system. (b) Fault-parallel component of the GNSS velocities in the Yilan-Yitong box in (a) projected to a fault normal profile. Gray curves are based on equation (1.1) assuming $D_G = 15$ km (more localized) or 30 km (less localized) and $V_o = 2.6$ mm/yr. (c) Similar to (b) but for the Yishu fault.

Other exceptions are also reported in the literature. For example, Dolan and Meade (2017) cited examples showing late-interseismic deformation faster than $V_o/2$ or less localized than that shown in Figure 1.3a. However, they considered these cases anomalous deviations from the more commonly reported pattern of Figure 1.3a due to various special geological circumstances, such as temporal clustering of past earthquakes,

transient changes in fault slip rate at depth, interaction with other faults, and so forth. We question whether all these cases, as well as those shown in Figures 1.5 and 1.6, are truly anomalous and explore if some of them can be explained by the same mechanical process as for those in Figure 1.3a.

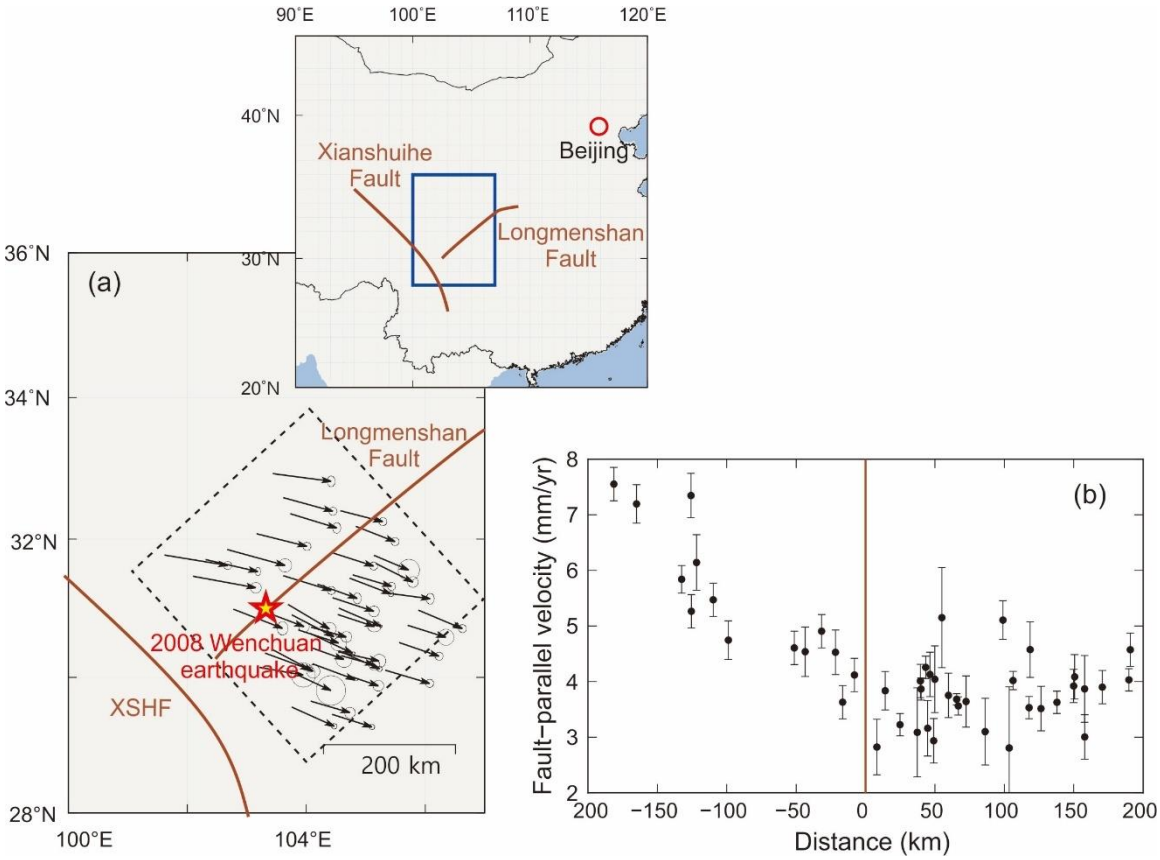

Figure 1.6. Similar to Figure 1.5 but for the Longmenshan Fault. (a) The star denotes the epicentre of the 2008 Wenchuan earthquake. Inset shows the location and the major fault systems of the map area. (b) Fault-parallel component of the GNSS velocities in the dashed box across the Longmenshan Fault in (a) projected to a fault normal profile.

1.3. Motivation of This Study

A theoretical challenge for the elastic dislocation model is to explain the driving force for the constant creep below the fault. Usually large faults are loaded by far-field tectonic forces, and the creep beneath the locked zone cannot be as fast as the far-field geological rate because of impedance by the stress shadow of the locked segment. If the

model can explain data from many faults (Figure 1.3b), there must be some real-Earth mechanism that drives the creep to achieve such a high rate.

As mentioned in Section 1.2, there are locked strike-slip faults that do not exhibit localized interseismic deformation. It is not possible to fit the geodetic observations around these faults with equation (1.1) with any geologically reasonable value of D. Here a geologically reasonable value can be defined by observed seismicity or knowledge of the geothermal field. Earthquakes and fault locking occur only in the shallow, cold, and hence brittle part of the crust, which in most continental settings rarely exceeds 30 km depth (Watts and Brov, 2003; Wright et al., 2013). For both segments of the TLF shown in Figure 1.5, the dislocation models with a geologically reasonable value of $D = 15$ or 30 km and geological slip rate $V_o = 2.6$ mm/yr are far from fitting the observations (Figures 1.5b and 1.5c). Exceptions like this prompted us to question the perceived universal applicability of the elastic dislocation model. Any mechanism that can explain the widely reported localized deformation shown in Figure 1.3 must also explain the distributed deformation shown in Figure 1.5.

The real Earth exhibits a viscoelastic behaviour, as has been demonstrated by Glacial Isostatic Adjustment (GIA) and postseismic deformation studies (e.g., James et al., 2000; Wang et al., 2012; Hu and Freymueller, 2019). The elastic dislocation model does not address the effect of time-dependent deformation due to viscoelasticity, especially the ongoing deformation due to previous earthquakes. I will demonstrate in this thesis that viscoelasticity is the key to finding a common mechanism that can explain both the localized and distributed deformation. Another issue worth mentioning is an often noticed inconsistency between the geodetic locking depth D_G and the value of D derived from seismological studies (e.g., Smith-Konter et al., 2011; Wright et al., 2013). This inconsistency may be associated with the neglect of time-dependent viscoelastic deformation by the elastic dislocation model. Although I will not discuss the seismologically derived D in this thesis, I will briefly discuss problems in the definition and determination of the geologic locking depth D_G in **Chapter 4**.

Leaving aside along-strike variations, the deformation shown in Figures 1.2 through 1.6 reflects a combination of two contributions: (1) steady tectonic loading from the far

field and (2) lasting deformation caused by past seismic ruptures of the same fault in a viscoelastic Earth. For a laterally homogeneous system with an infinitely long strike-slip fault symmetrically driven by far-field velocity $V_o/2$ at two fault-parallel boundaries at distance F from the fault, the steady tectonic loading component is the solution of a simple shear problem, with velocity V proportional to distance to the fault x:

$$V = \frac{V_o}{2F}\, x \tag{1.2}$$

In this situation, the velocity field is time-independent, regardless of rheology, and depicts no localization of deformation. Localization of deformation can be brought about only by local weaknesses around the fault. Elastic or viscoelastic models that emphasize steady loading invoke such local mechanical weaknesses as low viscosity beneath or low stiffness around the locked fault (e.g., Chéry, 2008; Traoré et al., 2014; Lindsey et al., 2014; Yamasaki et al., 2014). In these models, localization of deformation occurs only to a limited degree as will be detailed in **Chapter 3**.

In comparison, previous earthquakes play a more important role in localizing deformation. An earthquake induces shear stress in the underlying viscoelastic asthenosphere. The relaxation of the induced shear stress is accompanied with viscous shear flow in the same sense, which continues to drive surface deformation from below. If the interval between earthquakes is short, the viscous shear is repeatedly reinvigorated by subsequent earthquakes before it is fully relaxed. Viscoelastic models that emphasize the role of past earthquakes rely on such sustained and localized viscous deformation of the asthenosphere (e.g., Takeuchi and Fialko, 2012; Johnson, 2013; Meade et al., 2013; Hearn and Thatcher, 2015). These models have met greater success in explaining localization. Besides, they well explain postseismic deformation within years to decades after an earthquake that features near-fault velocities well exceeding $V_o/2$.

In this study, I will use numerical models to study how and to what degree the two contributors affect the interseismic deformation in order to identify the physical mechanism that can explain both localized and distributed interseismic deformation as shown in Figures 1.3, 1.5 and 1.6.

1.4. Structure of This Thesis

After this introduction, **Chapter 2** describes the geometry and rheology of the finite element model, delineates the earthquake cycle model, compares the finite element model (FEM) with analytical solutions, and clarifies the term “localization”. **Chapter 3** illustrates that far-field loading alone cannot explain the observed localized deformation even in the presence of extreme local weaknesses. **Chapter 4** demonstrates the effects of previous earthquakes, highlights the fundamental mechanism that controls the deformation pattern, and tests the effects of various types of shear zones below the fault. **Chapter 5** explores the three-dimensional (3-D) effects on the deformation pattern, such as the effects of a recent earthquake, nearby ruptures and creeping segments, and extends what is learned from strike-slip faults to oblique faults. **Chapter 6** addresses conclusions and proposals for future studies.

Some of the materials in this thesis, particularly those in **Chapters 3**, **4**, and **5**, have been presented in a Journal of Geophysical Research paper (Zhu et al., 2020). In this thesis, I enrich the materials with more technical details that could not be included in the journal paper because of space limits. Some of the text is thus directly from that paper.

Chapter 2. Modelling Methods

In this chapter, I will first introduce the model geometry and the linear viscoelastic rheology used in this study. I will then describe the finite element models for a strike-slip fault, for both a single earthquake and periodic earthquake cycles. I will also discuss the meaning of "localization" in observations of velocities versus displacements and recommend a quantitative measure of velocity localization.

2.1. The Finite Element Model

I employ a model as comparable as possible to the classical viscoelastic model of Nur and Mavko (1974) and Savage and Prescott (1978a). It consists of a uniform elastic layer of thickness H overlying a uniform viscoelastic substrate and is driven by constant velocity $V_o/2$ at far-field boundaries (Figure 2.1). From the surface to depth D, the fault is locked between earthquakes but slips uniformly during earthquakes. The displacement and stress singularity at depth D is purposely retained in order to be similar to the classical model and is numerically handled by using very fine elements. All distances in this thesis are measured in terms of D unless otherwise specified. Earlier models of this type tend to focus on the situation of $D < H$, with the section of the fault between $z = D$ and H assumed to be creeping at V_o (Savage and Prescott, 1978a), frictionless (Li and Rice, 1987), or a viscous shear zone (Johnson and Segall, 2004). More recent models tend to assume $D \geq H$, with the bottom edge of the fault touching or penetrating into the viscoelastic substrate (Takeuchi and Fialko, 2012; Meade et al., 2013; Yamasaki et al., 2014; Hearn and Thatcher, 2015). Except for some test models, I assume $D = H$.

For numerical modelling, I use a Cartesian version of the finite element code PGCvesph developed by Jiangheng He, Pacific Geoscience Centre, Geological Survey of Canada. Mathematical and numerical details of the code have been provided in Hu (2004, 2011) and Wang et al. (2012), and numerical results have been compared with analytical solutions such as surface and internal displacements due to shear and/or tensile faulting in an elastic half-space (Okada, 1985, 1992) and postseismic deformation in a spherical layered Earth (Pollitz, 1992, 1997).

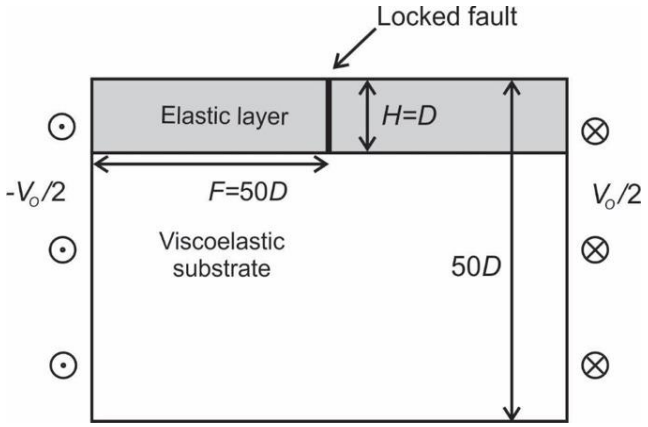

Figure 2.1. A cross-section view of the strike-slip fault model with viscoelastic rheology employed in this study.

I set the bottom boundary of the model to $50D$ and the two strike-normal boundaries to be very far apart ($> 140D$), and I have verified that these choices have little influence on surface results in the central part of the model. However, the model results can never be free of the influence of the strike-parallel boundaries where $V_o/2$ is applied. Vastly different boundary-to-fault distances (F) have been used in previous models and affected localization of deformation to variable degrees, such as $\sim 3D$ (Zhang and Sagiya, 2018), $\sim 20D$ (Takeuchi and Fialko, 2012; Hearn and Thatcher, 2015), $50D$ (Yamasaki et al., 2014), or $120D$ (Hetland and Hager, 2006) (Table 2.1). F represents the dimension of the material that accommodates the shear strain loaded by far-field tectonic forces. Neither a very small nor an infinitely large F is geologically reasonable, although the optimal value cannot be easily quantified. For the purpose of this study, I set $F = 50D$, adequately distant to be considered far-field.

Table 2.1. Model geometry in previous 2-D strike-slip fault models.

Reference	Locking depth D (km)	Elastic thickness H (km)	Fault-parallel boundary distance F (km)	Maximum model depth (km)	Fault length L (km)
Takeuchi and Fialko (2012)	17	12 (~0.7D)	300 (~18D)	75 (~4.4D)	100 (~6D)
Yamasaki et al. (2014)	16	12 (0.75D)	200 (12.5D) 400 (25D)	40 (2.5D) 80 (5D)	1000 (62.5D)
Hearn and Thatcher (2015)	14	14 (1D)	325 (~23D)	320 (~23D)	200 (~14D) 1150 (~82D)
Traoré et al. (2014)	12	12 (1D)	100 (~8.3D)	162 (13.5D)	100 (~8.3D) 200 (~16.7D)
Hetland and Hager (2006) *	D	D	120D	120D	∞

* In Hetland and Hager (2006), all distances are measured in terms of D without certain values.

2.2. Viscoelastic Rheology

In this work, I employ linear rheology (strain or strain rate proportional to stress) for all the viscoelastic models. The linear rheology allows us to separately model the deformation components due to far-field tectonic loading and due to past earthquakes, as discussed in Section 1.3, and then combine the results to obtain the total deformation field. Besides, the use of the linear rheology also enables us to model deformation due to multiple earthquakes by linearly combining the effects of individual earthquakes in both space and time. Details of the mathematical operations for multi-earthquake modelling will be given in Section 2.4 for 2-D earthquake cycle models.

2.2.1. Maxwell and Burgers Rheology

Linear viscoelasticity is a combination of linear elastic (Hooke solid) and linear viscous (Newtonian fluid) elements (Burgmann and Dresen, 2008). Two commonly used linear viscoelastic materials are Maxwell and Burgers materials (Figure 2.2a). The Maxwell material can be envisioned as a Hooke solid (spring) in series with a Newtonian fluid (dashpot). Its immediate response to loading is controlled by the elastic component, but the later response is increasingly controlled by the viscous component. To illustrate

the behaviour of the Maxwell material, let us consider only the shear stress and shear strain as follows.

The relationship between the elastic shear strain ε_E and the shear stress σ is given by the Hooke's law:

$$\varepsilon_E = \frac{\sigma}{2\mu_M} \tag{2.1}$$

where μ_M is the shear modulus (i.e., rigidity) of the Maxwell material. For a Newtonian fluid, the viscous shear strain rate $\dot{\varepsilon_V}$ is related to the shear stress σ by:

$$\dot{\varepsilon_V} = \frac{\sigma}{2\eta_M} \tag{2.2}$$

where η_M is the viscosity of the Maxwell material, and the dot at the top denotes time derivative (rate). The total shear strain rate of a Maxwell material is the sum of the elastic and viscous components:

$$\dot{\varepsilon} = \dot{\varepsilon_E} + \dot{\varepsilon_V} = \frac{\dot{\sigma}}{2\mu_M} + \frac{\sigma}{2\eta_M} \tag{2.3}$$

With a suddenly imposed constant stress σ_o and zero strain ($\dot{\varepsilon} = 0$), the solution for (2.3) is

$$\sigma = \sigma_o \exp\left(-\frac{\mu_M}{\eta_M} t\right) \tag{2.4}$$

which shows exponential relaxation of stress with time. After $\tau_M = \eta_M/\mu_M$, the stress relaxes to only $1/e$ of the initial value. τ_M is the Maxwell relaxation time.

The Burgers rheology is a more realistic description of the rock materials in the mantle, consisting of a Kelvin solid in parallel with a Maxwell fluid (Figure 2.2a) (Peltier et al., 1981; Pollitz, 2003; Burgmann and Dresen, 2008; Wang et al., 2012). Upon a suddenly imposed loading, the Burgers material exhibits two phases of deformation: a phase of transient creep followed by a phase of steady-state flow (Figure 2.2b). The Maxwell fluid describes the steady-state flow after the initial transient phase. The transient creep is represented by the Kelvin solid, which can be envisioned as a Hooke solid in parallel with a Newtonian fluid (Figure 2.2a). Similar to the Maxwell fluid, the

Kelvin solid also has a relaxation time referred to as the Kelvin relaxation time $\tau_K = \eta_K/\mu_K$, where η_K and μ_K are the viscosity and rigidity, respectively, of the Kelvin body (Figure 2.2a). More complex linear viscoelastic rheology can be described by combining multiple Maxwell and Kelvin elements (e.g., Hetland and Hager, 2005).

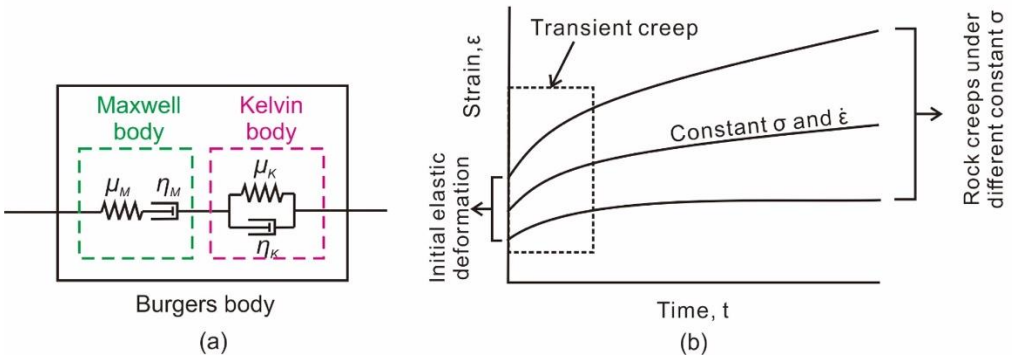

Figure 2.2. Illustration of the linear rheology and two phases of rock creep. (a) Schematic illustration of Maxwell body, Kelvin body and Burgers body. Springs and dashpots represent elastic and viscous components, respectively. (b) Strain evolution of a rock specimen in creep experiments under constant stress, showing transient creep followed by steady-state flow. Modified from Wang et al. (2012).

All the models in this thesis are assigned a uniform rigidity 31.7 GPa and Poisson's ratio 0.25 for both the elastic layer and viscoelastic substrate. With this value of μ_M, we have $\tau_M = 10$ yr if $\eta_M = 10^{19}$ Pa s. Since the focus of this study is on the interseismic deformation after the transient phase in Figure 2.2b, I mainly employ the Maxwell rheology so that fewer parameters need to be considered. Burgers bodies are also considered in some of the earthquake cycle models to illustrate the effects of transient rheology.

2.2.2. On Viscosity Evolution after an Earthquake

Right after a large earthquake, postseismic deformation is fast and rapidly decays with time, suggesting a low viscosity in the viscoelastic asthenosphere. However, the interseismic deformation, which is the focus of this study, is slower and more stationary, indicating a high viscosity later in the earthquake cycle. Models with a constant viscosity cannot reconcile the two patterns of deformation, leading to the recognition that the

viscosity of the asthenosphere must increase with time after an earthquake. For example, after the 1999 Izmit-Düzce earthquake, GNSS observations captured a fast and rapidly decaying signal of postseismic deformation within several months, and later the deformation was more stable (Ergintav et al., 2009). To reconcile these different deformation patterns, Hearn et al. (2009) employed the Burgers rheology to describe both the early and later deformation. Table 2.2 lists viscosities used in some previous studies to accommodate postseismic and interseismic deformation.

The viscosity increase has also been modelled using the nonlinear power-law rheology (Takeuchi and Fialko, 2012; Hearn and Thatcher, 2015). This represents different physics from the linear transient rheology. With the linear transient rheology, such as the Burgers rheology, the viscosity simply increases with time. In the power-law rheology, the shear strain rate is represented by the following equation:

$$\dot{\varepsilon} = C\sigma^n \exp(-(Q + PV)/RT) \qquad (n > 1) \tag{2.5}$$

where parameter C depends on the material composition, grain size and content of fluid, and n, Q, V and R are all material constants (Bürgmann and Dresen, 2008). An effective viscosity can be defined as $\eta_{eff} = \sigma/\dot{\varepsilon}$, which decreases with increasing shear strain rate. In particular, the higher strain rate beneath the rupture zone just after an earthquake causes lower effective viscosity. As explained above, non-linear rheology is not invoked in this study. Instead, some shear zone models will be designed to assess the impact of the non-linear effects in Section 4.4.

Table 2.2. Examples of Kelvin viscosity η_K and Maxwell viscosity η_M values used in previous strike-slip fault deformation modelling.

Reference	Kelvin viscosity η_K (Pa s)	Maxwell viscosity η_M (Pa s)	Related earthquake
Hearn et al. (2009)	$2\sim5\times10^{19}$	2×10^{20}	1999 Izmit-Düzce, Mw 7.6
Pollitz (2005)	$\sim1\times10^{17}$	$\sim2.8\times10^{18}$	2002 Denali, Mw 7.9
Ryder et al. (2011)	$\sim9\times10^{17}$	$\sim1\times10^{19}$	2001 Kokoxili, 7.8
Ryder et al. (2011)	$\sim5\times10^{17}$	$\sim1\times10^{19}$	1997 Manyi, 7.4

2.3. A Single 2-D Earthquake and Comparison with Analytical Solution

Before explaining in the next section how earthquake cycles are modelled, here I describe the model for a single earthquake in a 2-D strike-slip (i.e., infinitely long) fault with coseismic slip U_o from the surface to depth D. For all the 2-D models used in this study, I set the length of the strike-slip fault (L), i.e., the distance between two fault-normal boundaries, to be > $140D$, adequate to be considered infinitely long. Owing to the symmetry of the 2-D system, there is no strike-normal displacement, the displacement of the fault relative to the fixed remote boundary is either $\pm V_o/2$ (earthquake) or zero (interseismic), and the displacement of the same vertical surface below the fault stays identically zero. Therefore, it can be modelled by using only half of the model domain, with the plane of symmetry containing the fault being a side boundary of the model mesh (Figure 2.3). 3-D models involving full-domain meshes will be used in **Chapter 3** (without earthquakes) and **Chapter 5** (with earthquakes).

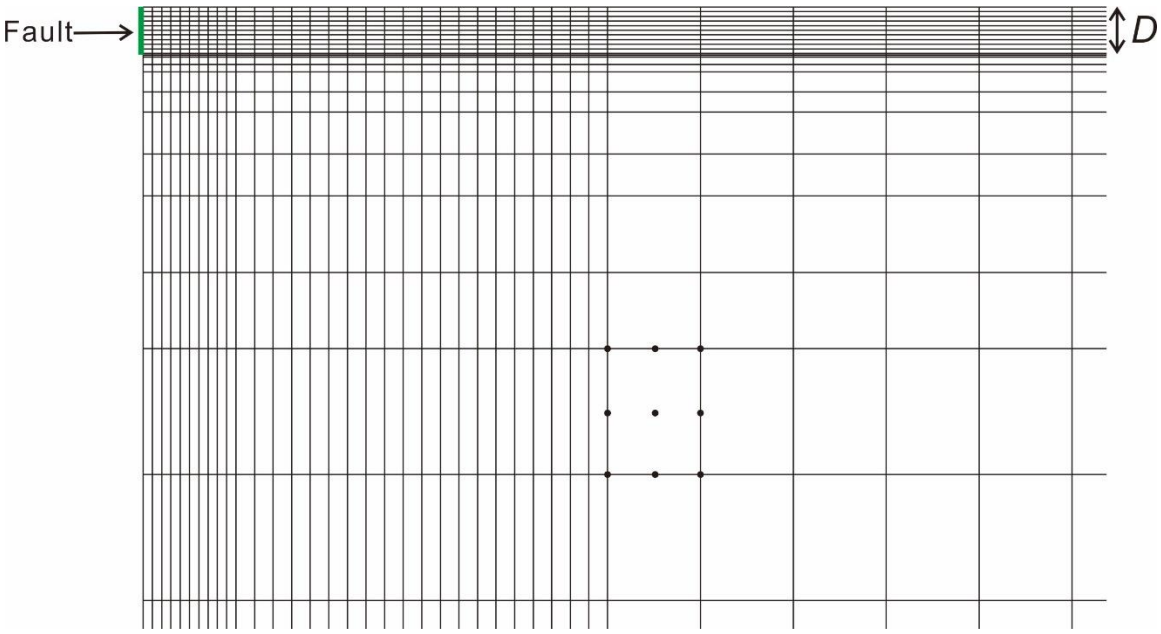

Figure 2.3. Cross-section view of the near-fault part of the finite element model along a fault-normal profile. In 3-D, each element has 27 nodal points. Nine of them can be seen in this side view, as illustrated here using a randomly selected element.

I have compared the numerical results for a single earthquake with an analytical solution (Nur and Mavko, 1974; Savage and Prescott, 1978b) which features the same

system except with infinitely distant bottom and side boundaries. The solution is (Savage and Prescott, 1978b):

$$U = \frac{U_o}{\pi}\left[\arctan\left(\frac{x}{D}\right) + \sum_{n=1}^{\infty} A_n(\tau)\arctan(W_n)\right] \tag{2.6}$$

where the normalized time τ and coefficients A_n and W_n are given by:

$$\tau = \mu t/2\eta = t/2\tau_M \tag{2.7}$$

$$W_n = \frac{2xD}{4n^2H^2 - D^2 + x^2} \tag{2.8}$$

$$A_1 = 1 - \exp(-\tau) \tag{2.9}$$

$$A_{n+1}(\tau) = A_n(\tau) - \left(\frac{\tau^n}{n!}\right)\exp(-\tau) \tag{2.10}$$

As explained in Section 2.1, I assume H/D = 1. A comparison between the FEM and analytical solutions is shown in Figure 2.4. As expected, the difference between the two models increases as we move away from the fault because of the different side-boundary conditions. The fault-parallel boundaries are at $x = F = 50D$ in the FEM model (see Section 2.1) but are infinitely far away in the analytical model. Increasing F from $50D$ to $100D$ in the FEM model reduces the difference from the analytical model (results not displayed).

Other small differences between the two types of solutions are also expected, given the finite size of the elements used in the numerical model. In particular, in the analytical model, the displacement across the bottom edge of the fault at $z = D$ has a sudden jump from U_o to zero during the earthquake, featuring a singularity in displacement and stress. The FEM cannot precisely model this singularity even if we make the mesh very dense around this depth.

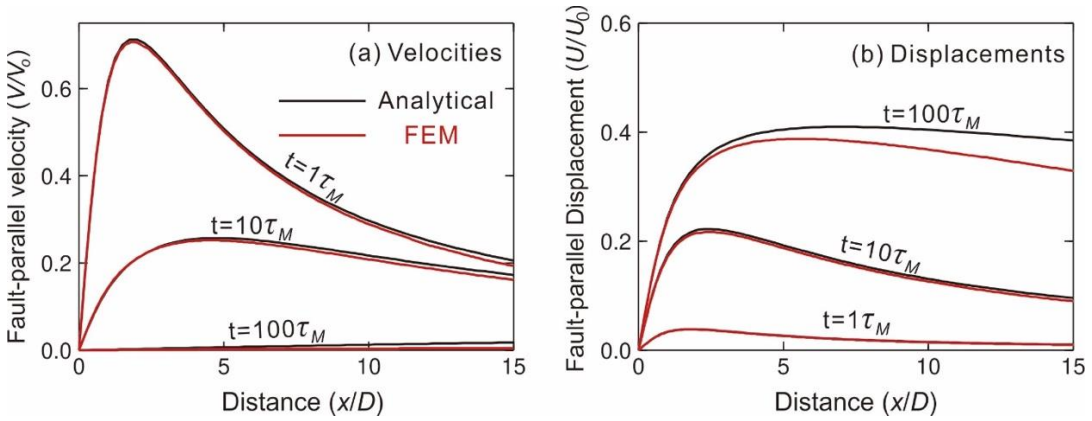

Figure 2.4. Comparison of postseismic deformation after a single strike-slip earthquake predicted by the analytical solution of Nur and Mavko (1974) (black) and the FEM solution (red) for a 2-D fault. (a) Velocities. (b) Displacements.

2.4. Earthquake Cycle Modelling

2.4.1. Method of Superposition

Most previous viscoelastic earthquake-cycle studies employ periodic earthquakes with a constant recurrence interval. For most of the models in this work, I also use periodic earthquake cycles, and I use the same finite element mesh as shown in Figure 2.3. As mentioned in Section 2.2, owing to the linear rheology, the two contributions to interseismic deformation mentioned in the Introduction are linearly combined in the modelling. The far-field loading gives rise to a steady velocity field $V_1(x)$ as described by equation (1.2). Given $F = 50D$, $V_1(x) = xV_o/2F = xV_o/100D$. The past earthquakes in the model are simulated by assuming uniform slip $U_o = TV_o$ from the surface to depth D at a regular interval T (Figure 2.5), similar to some of the previous studies (e.g., Savage and Prescott, 1978a). Because all the earthquakes share the same viscoelastic relaxation processes due to the linear rheology, the total displacement U is a combination of the displacements caused by identical individual earthquakes that occur at different times:

$$U(x,y,z,t) = V_1(x)t + \sum_{m=0}^{\infty}[U_2(x,y,z,t+mT) - U_2(x,y,z,mT)] \qquad (2.11)$$

The first term is the far-field contribution, and the second term is the past-earthquake contribution with U_2 being displacement caused by a single earthquake. The corresponding velocity is:

$$V(x,y,z,t) = V_1(x) + \sum_{m=0}^{\infty} [V_2(x,y,z,t+mT)] \tag{2.12}$$

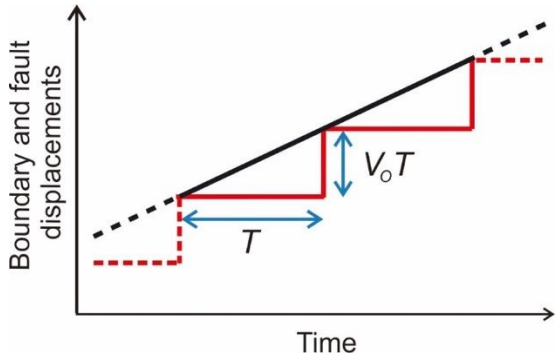

Figure 2.5. Displacements assigned to the far-field boundary (black) and to the fault (red) in 2-D models of periodic earthquake cycles.

A model with no along-strike variations will be 2-D and independent of y (Cohen and Kramer, 1984). I use the finite element model only to obtain the viscoelastic response of the system to a single earthquake (akin to a Green's function). The multi-cycle results are obtained by analytically convolving this response with the fault slip history shown in Figure 2.5 following equations (2.11) and (2.12).

2.4.2. "Spin-up" of the Earthquake Cycle Deformation

There is a technical issue to be considered that is commonly referred to as the "spin-up" of the earthquake cycle deformation (e.g., Hetland and Hager, 2006). In models of kinematically assigned identical earthquakes, only after a number of cycles (m in equation (2.11) and (2.12) large enough to approximate infinity), will the effect of the initial condition be fully diminished to allow the deformation to be cycle-invariant. Some researchers have also considered models in which earthquake recurrence is not kinematically assigned but is governed by a specified strength of the fault. For such stress-controlled earthquake cycle models, earthquakes will essentially occur at regular intervals with cycle-invariant deformation after a longer time of "spinning-up" (e.g., Takeuchi and Fialko, 2012).

Figure 2.6 shows the velocity timeseries at various distances x after different

numbers of cycles to illustrate the spin-up process. For models with a recurrence interval $T = 2\ \tau_M$, the difference between velocities after 25 cycles and those after 50 cycles becomes less than $0.003V_o$ over the distance range 0 – $20D$ (Figures 2.6a and 2.6b, blue curves well overlap black curves). Therefore, deformation after 25 cycles (50 τ_M) can be regarded as being cycle-invariant. For $T = 10\ \tau_M$, invariance is achieved after 5 cycles (Figures 2.6c and 2.6d, green curves overlap both blue and black curves). I have tested many different lengths of T, and the results suggest that cycle invariance is achieved within about $50\tau_M$, whatever number of cycles is included in this time span. Employing the Burgers rheology with a small Kelvin relaxation time such as $\tau_K = 0.1\tau_M$ does not change the "spin-up" time, as illustrated by the examples in Figure 2.7.

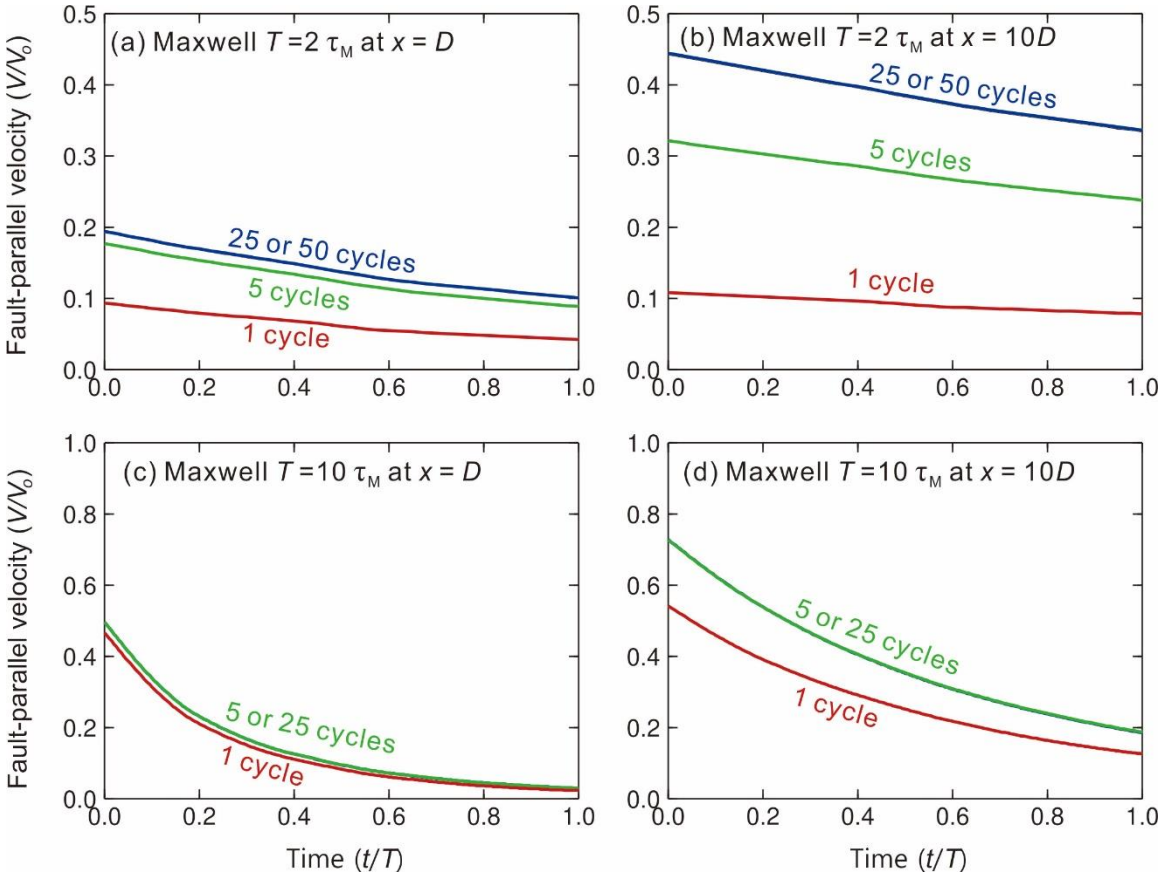

Figure 2.6. An illustration of earthquake cycle spin-up using velocity time histories at $x = 1$ and $10D$ for a 2-D Maxwell model with $T = 2\tau_M$ or $10\tau_M$. (a) Fault-parallel velocity timeseries at $x = D$ of the Maxwell model with $T = 2\tau_M$. Cycle-invariance is achieved after 25 cycles, such that the results after the 25th and 50th earthquakes are nearly identical. (b) Similar to (a) but for $x = 10\ D$. (c) Similar to (a) but for a Maxwell

model with $T = 10\tau_M$. Cycle-invariance is achieved after 5 cycles, such that the results after the 5th and 25th earthquakes are nearly identical. (d) Similar to (c) but for $x = 10D$.

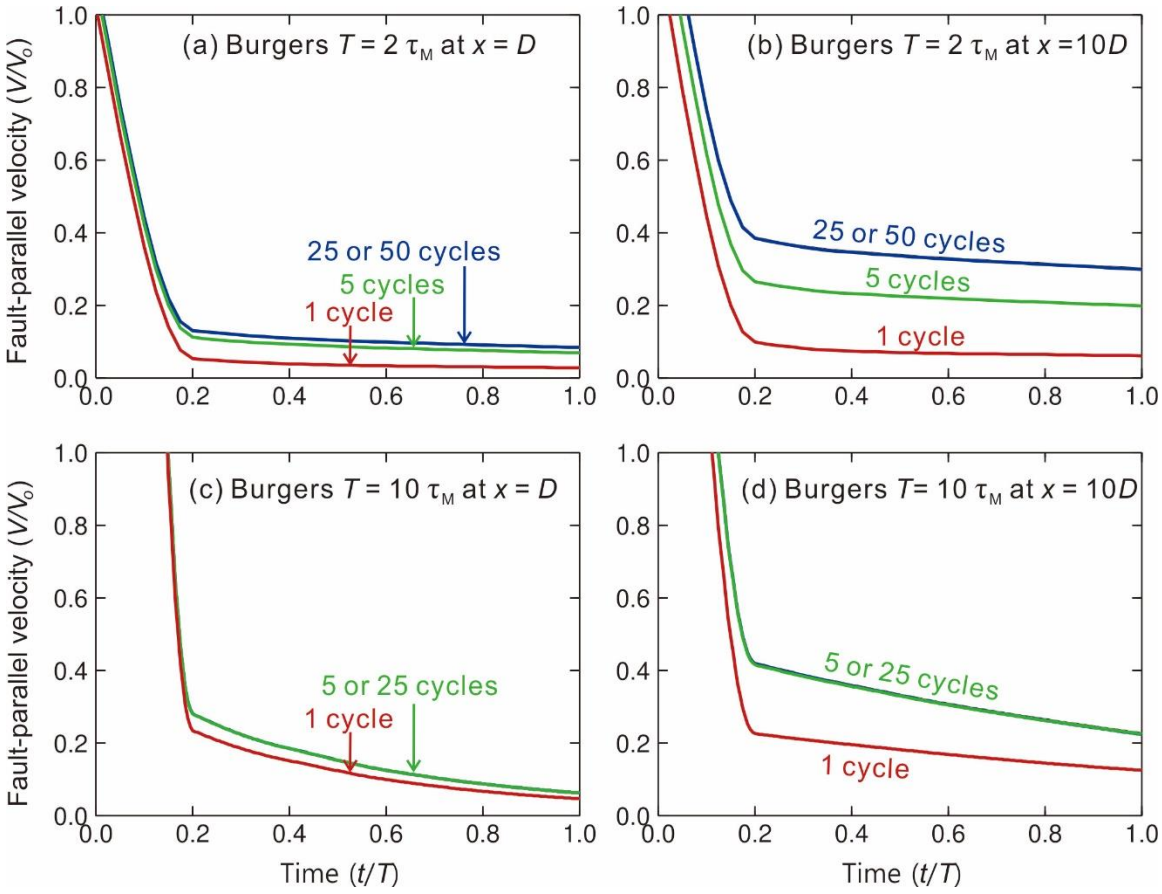

Figure 2.7. "Spin-up" for Burgers models with $\tau_K = 0.1\tau_M$. Legends and labels are the same as Figure 2.6.

Cycle-invariant surface velocities as a function of distance from the fault for the Maxwell model in comparison with the Burgers model with $\tau_K = 0.1\tau_M$ are shown in Figure 2.8 at three different time steps since the last earthquake, representing postseismic ($0.05\ T$), mid-interseismic ($0.5\ T$), and late-interseismic (T, just before the next earthquake) stages. For $T = 5\ \tau_M$, the Burgers model features faster deformation than the Maxwell model at the postseismic stage ($t = 0.05T = 0.25\tau_M$) due to the low viscosity of Kelvin body (Figure 2.8a). For $T = 10\ \tau_M$ at $t = 0.05T = 0.5\ \tau_M$, the Burgers model features slower deformation than the Maxwell model. This only reflects the fact that the postseismic deformation depends on the Kelvin time, regardless of the earthquake cycle

length. However, the difference between the Maxwell and Burgers models at mid-interseismic ($t = 0.5T$) and late-interseismic ($t = T$) period is much smaller (Figure 2.8). Therefore, knowledge learned from the simpler Maxwell models regarding mid- and late-interseismic deformation also applies to the Burgers models.

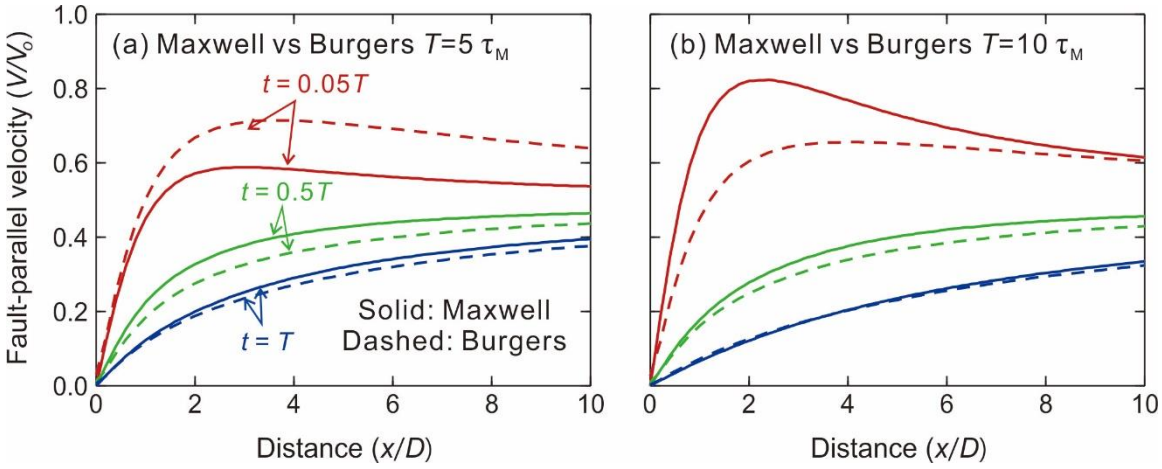

Figure 2.8. Comparison of Maxwell and Burgers models ($\tau_K = 0.1\tau_M$) to show their similarity at the late-interseismic stage. (a) Velocities along a fault-normal profile at different stages in the cycle for $T = 5\tau_M$. (b) Similar to (a) but for models with $T = 10\tau_M$.

2.4.3. Comparison with Analytical Solution

I have compared my FEM earthquake cycle models with an analytical solution from Savage and Prescott (1978a) which is based on the Nur and Mavko (1974) solution for a single earthquake discussed in Section 2.3. The total displacement due to periodically occurring earthquakes of uniform slip U_o from surface to depth D can be written as:

$$u(x,t)/U_o = \pm\tau/2\tau_o + \sum_{m=0}^{N} u_2(x, \tau - m\tau_o) \tag{2.13}$$

where τ and τ_o are defined as:

$$\tau = \frac{t}{2\tau_M} \tag{2.14}$$

$$\tau_o = T/2\tau_M \tag{2.15}$$

and $u_2(x,\tau)$ is the displacement caused by an elementary earthquake cycle (Figure 2.5)

given by:

$$u_2(x,\tau)/\Delta u = \begin{cases} 0 & \tau < 0 \\ \pi^{-1}\{\left(\frac{\tau}{\tau_o}\right)\left[\arctan\left(\frac{x}{D}\right) - \frac{\pi}{2}\right] - \sum_{n=1}^{\infty} B_n(\tau)\arctan\left(W_n\right)\} & 0 < \tau < \tau_o \\ \pi^{-1}\sum_{n=1}^{\infty}(B_n(\tau-\tau_o) - B_n(\tau) + A_n(\tau-\tau_o)\arctan(W_n) & \tau > \tau_o \end{cases} \quad (2.16)$$

where A_n and B_n are defined by the following equations:

$$A_1(\tau) = 1 - \exp(-\tau) \quad (2.17)$$

$$A_n(\tau) = A_{n-1}(\tau) - \tau^{n-1}\exp(-\tau)/(n-1)! \quad (2.18)$$

$$B_1(\tau) = [\tau - A_1(\tau)]/\tau_o \quad (2.19)$$

$$B_n(\tau) = B_{n-1}(\tau) - A_n(\tau)/\tau_o \quad (2.20)$$

If $D < H$, the elastic material between D and H moves at rate V_o, in this regard similar to the elastic dislocation model (Figure 1.6). Because I assume $D = H$ (Section 2.1), this imposed creep is not present.

Because $\tau/\tau_o = t/T$ (equation (2.14) and (2.15)), equation (2.13) can be written in the following form:

$$u\left(x,\frac{t}{T}\right)/U_o = \pm\frac{t}{2T} + \sum_{m=0}^{N} u_2\left[x,\tau_o\left(\frac{t}{T} - m\right)\right] \quad (2.21)$$

Therefore, results derived at t measured as a fraction of T are identical for the same τ_o value, i.e., the same T/τ_M ratio.

Figure 2.9 shows a comparison between the analytical solution and cycle-invariant FEM results using an example with $\tau_M = 20$ yr and $T/\tau_M = 10$. The surface displacements and velocities are evaluated at various stages in one cycle. As explained in Section 2.3, small differences between the two types of models are always expected. The main differences arise because of the distance to the fault-parallel boundaries, which is infinite in the analytical solution but finite (e.g., $F = 50D$) in the numerical solution. Compared to the analytical results, surface deformation of the FEM model is slower at the beginning of the cycle but faster later in the cycle (Figure 2.9b), which is also

reflected in the displacement profiles (red curves in Figure 2.9a). This is because the fault-parallel boundaries in the finite element models limit the initial postseismic relaxation. Increasing distance F will bring the FEM results closer to the analytical solution (not displayed), similar to the single-earthquake solutions in Section 2.3.

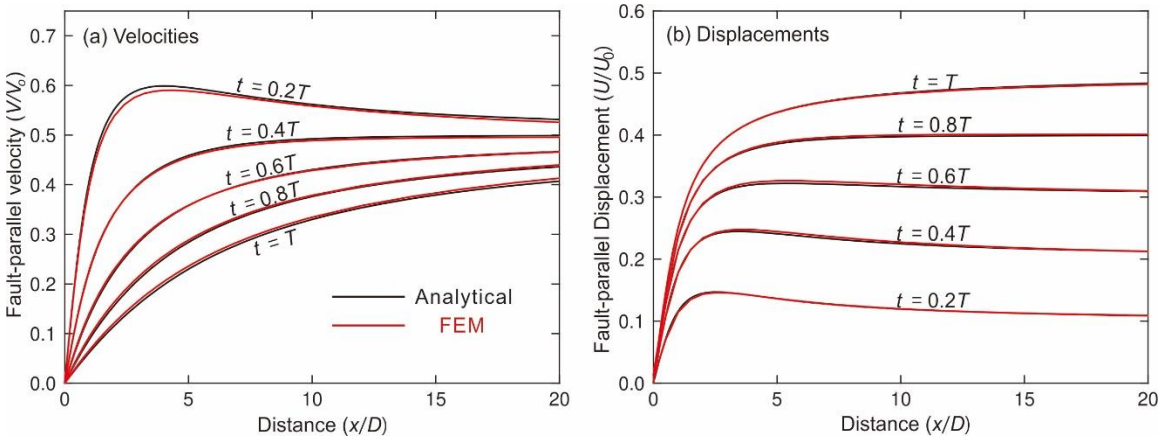

Figure 2.9. Surface deformation produced by the FEM earthquake cycle models (red) compared with the analytical solutions (black) from Savage and Prescott (1978a) for $T/\tau_M = 10$ at different stages during one earthquake cycle. (a) Surface velocities along a fault-normal profile. (b) Similar to (a) but for surface displacements.

I should mention two other minor issues. First, that the results derived at t as a fraction of T only depend on the T/τ_M ratio (equation 2.21) holds true also for the 2-D FEM model. For example, as shown in Figure 2.10a, a model with $\tau_M = 20\ yr$ and $T = 100\ yr$ or with $\tau_M = 200\ yr$ and $T = 1000\ yr$ have identical results at the same t/T. Second, as discussed in Section 2.1, some previous studies have employed various H/D ratios, but I assume $H/D = 1$ for this study. An FEM earthquake cycle model is shown in Figure 2.10b to illustrate the effects of the choice of H/D. The difference between velocity profiles for $H/D = 0.8$ (dashed curves in Figure 2.10b) and $H/D = 1$ (solid curved in Figure 2.10b) is rather small. However, if H/D = 1.2, the deformation is much slower because of the separation between the earthquake slip segment and the viscoelastic substrate. Most finite-element based, far-field loaded earthquake cycle models employ $H/D \leq 1$ (e.g., Takeuchi and Fialko, 2012; Yamasaki et al., 2014; Hearn and Thatcher, 2015).

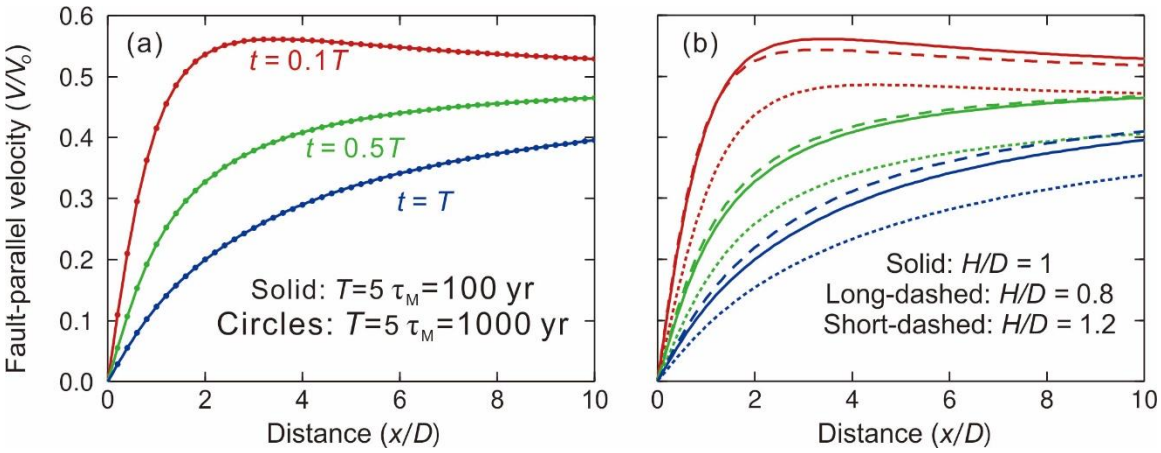

Figure 2.10. Examples of viscoelastic FEM earthquake cycle models. (a) An illustration to show that what is reflected by equation (2.21) is also true for the 2-D FEM model. (b) Models with different ratios of H/D, evaluated at different stages of the cycle (red: $t = 0.1T$, green: $t = 0.5T$, and blue: $t = T$).

2.5. What is Localization?

2.5.1. Velocities vs. Displacements

Before investigating the physical mechanism that controls the localization pattern, we should further clarify the meaning of "localization". The commonly reported localization of deformation is based on geodetic observations, which only constrain temporal changes in deformation. The useful data are velocities over a time window, not absolute positions at a given time. Localized deformation means that interseismic strain is increasing at a fast rate near the locked fault over the observation time span. It does not address how much strain is already accumulated since the last earthquake. For the elastic dislocation model described by equation (1.1), the velocity does not change with time, so that the velocity over any time interval can be used to infer the total displacement since the last earthquake. However, in the real Earth which exhibits a viscoelastic behaviour, the velocity changes with time, so that presently observed velocities do not contain unique information on the total displacement since the last earthquake. To estimate earthquake risk, we are concerned with the total accrued strain energy, not how fast it is accruing today.

This is illustrated by the FEM results shown in Figure 2.11 which compares late-interseismic surface deformation between two models with the same slip rate V_o, seismic

slip U_0, and T = 100 yr, but different $\tau_M = 20$ yr or 200 yr. At $t = T$, the velocity distribution for the model with a larger τ_M is more localized (Figure 2.11a), but the total displacements are the same in the two models (Figure 2.11b), indicating the same potential for earthquakes. Because the main purpose of the thesis is to explain the physical mechanism of localization of deformation in terms of velocities, I do not extensively discuss surface displacements and their hazard implications, although I will still show displacement results together with velocities for some examples.

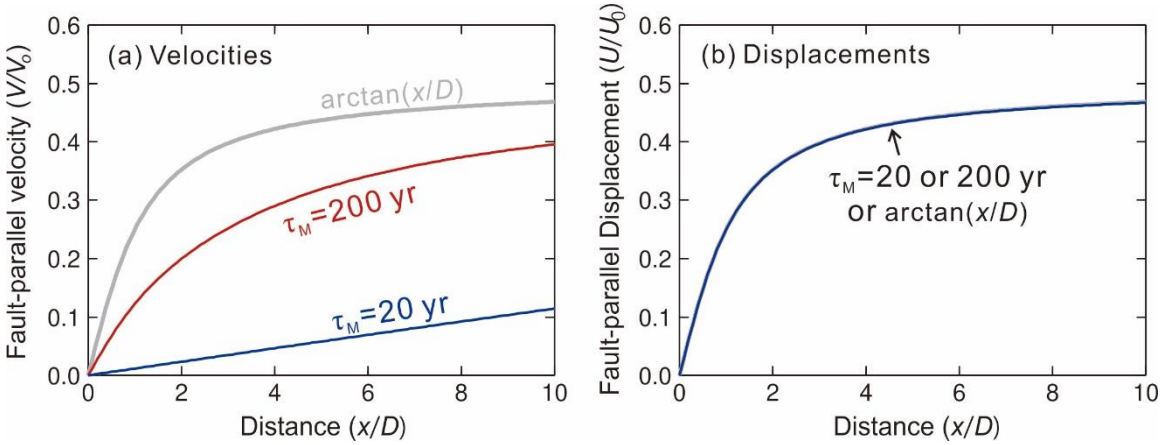

Figure 2.11. Comparison between velocity patterns and displacement patterns for two Maxwell earthquake cycle models with the same V_o, U_o and T (= 100 yr) but different τ_M as labelled. (a) Late-interseismic ($t = T$) velocities along a fault-normal profile. The elastic dislocation model (equation (1.1), grey curve) is shown for comparison. (b) Late-interseismic displacements.

2.5.2. A Quantitative Measure of Localization

In this study, I employ a parameter Γ_1, the normalized engineering shear strain rate averaged between the fault trace and $x/D = 1$, to measure the degree of localization. The engineering shear strain rate on the surface (x-y plane) $\dot{\gamma}_{xy}$ is given by:

$$\dot{\gamma}_{xy} = 2\dot{\varepsilon}_{xy} = \frac{\partial V_x}{\partial y} + \frac{\partial V_y}{\partial x} \tag{2.22}$$

where V_x and V_y are the fault-normal and fault-parallel velocities, respectively. Based on equation (2.22), Γ_1 can be written as:

$$\Gamma_1 = \frac{\partial V_y/V_o}{\partial x/D} = \frac{D}{V_o}\frac{V(D,0,0,t)}{D} = \frac{V(D,0,0,t)}{V_o} \tag{2.23}$$

where $V(D,0,0,t)$ is the fault-parallel surface velocity at $(x,y,z) = (D,0,0)$. As shown in Figure 2.12, Γ_1 represents the average slope of the velocity profile within $x/D = 0{\sim}1$. For the elastic dislocation model (equation (1.1)), Γ_1 is $V(D,0,0,t)/V_o = \arctan(1)/\pi = 0.25$ (Figure 2.12). This is the commonly used norm for localized deformation. In a system that is driven by far-field loading only, without previous earthquakes, equation (1.2) gives $V(D,0,0,t) = V_o/2$. With $F = 50D$, Γ_1 is only $D/2F = 0.01$ (Figure 2.12). The late-interseismic deformation of the Maxwell earthquake-cycle model with $T = 5\tau_M$ (Figure 2.12) lies between the two end-member cases, with $\Gamma_1 = 0.1226$.

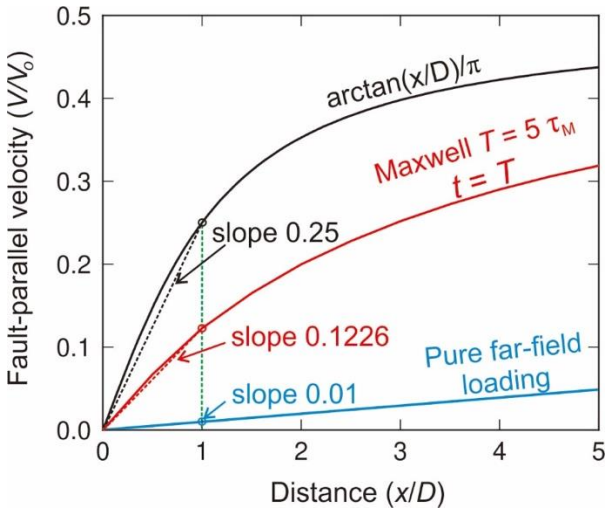

Figure 2.12. Illustration of the definition of Γ_1 (equation (2.23)). The arctan function is from equation (1.1) (black line). The pure far-field loading model is for $F = 50D$ (equation (1.2)). The Maxwell earthquake-cycle model is at $t = T = 5\tau_M$ (red curve).

Chapter 3. Limited Effects of Far-field Loading

It is useful to investigate separately the role of far-field loading and the role of previous earthquakes in localizing interseismic deformation. As mentioned in **Chapter 1**, surface deformation around a strike-slip fault in a laterally homogeneous system loaded only from the far-field shows a distributed pattern (e.g., Figure 2.12, blue curve). In this chapter, I will investigate the effects of local weaknesses that have been previously proposed by other researchers as mechanisms of localizing deformation. My model results demonstrate that the effect of far-field loading alone is very limited even in the presence of these weaknesses.

Since previous earthquakes are not considered here, it is convenient to consider a 2-D fault in a system in which the viscosity of the viscoelastic substrate is extremely high or low to maximize and minimize, respectively, the effects of local weaknesses. The elastic half-space model represents the scenario of $\tau_M \gg T$ so that the system stays elastic over the earthquake cycles, while the elastic plate model approximates the situation of $\tau_M \ll T$ so that the asthenosphere is fully relaxed in the later part of the interseismic period. The H/D ratio is > 1 and flexible only in this chapter so that the model can represent an elastic plate of any thickness ($H > D$) or an elastic half-space ($H \gg D$).

3.1. Weakness Below the Fault

In this section, I focus on weaknesses below the fault. As has been discussed in **Chapter 1**, the elastic dislocation model relies on the fast and constant creep imposed beneath the locked fault to localize surface deformation. Without the fast creep, the velocity field generated by far-field loading alone is distributed as described by equation (1.2) with the lowest value of Γ_1 as mentioned at the end of Section 2.5.2.

In the first set of models, I consider a frictionless fault (the weakest possible) below the shallow locked segment from depth D to the bottom of the model (Figure 3.1a). The frictionless deep segment can freely creep under far-field tectonic loading and therefore helps to localize surface deformation around the locked segment above. The frictionless fault under the locked segment in the elastic plate model ($H = 4D$) causes very slight localization of surface deformation compared to the model of no local weakness, but the

degree of localization is not comparable to that of the elastic dislocation model (Figure 3.2a). Increasing the elastic thickness causes greater localization (Figure 3.2b). However, even when $H >> D$ (e.g., $50D$), representing an elastic half-space, the effect is still much less than in the dislocation model (Figure 3.2a). The reason is that the deep free segment creeps too slowly because of impedance by the locked segment, in contrast with the full-rate (V_o) creep in the elastic dislocation model. Increasing the elastic thickness can enhance the creep rate, but even in a half-space, the creep rate is much lower than V_o.

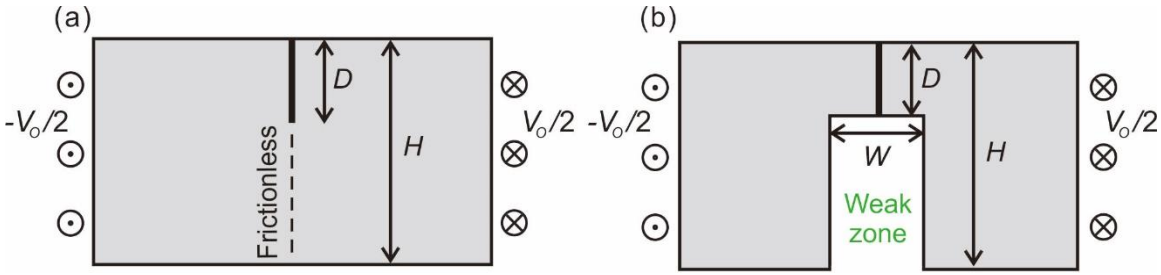

Figure 3.1. Cross-section view of model with a frictionless fault (dashed line) (a) or a weak zone of width W (b) below the locked fault (thick black line).

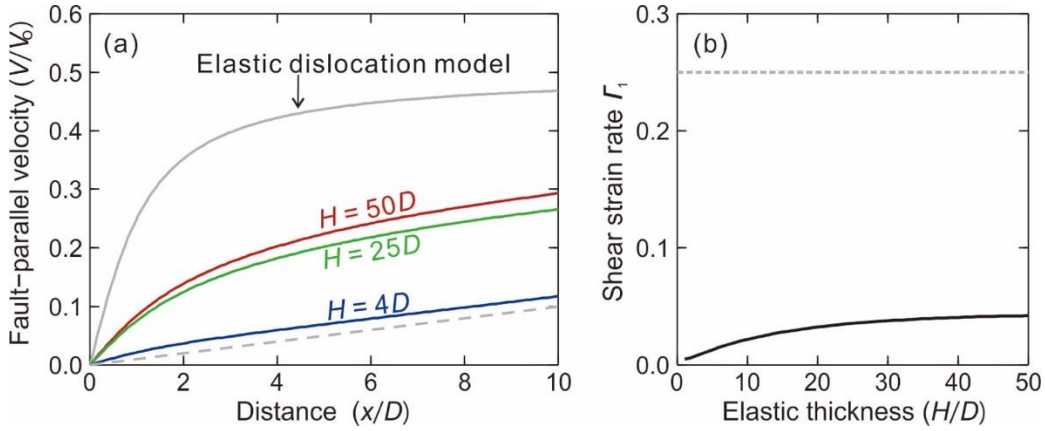

Figure 3.2. Effects of the frictionless fault below the locked fault. (a) Velocity profiles with different H. The grey solid line is the elastic dislocation model, and the grey dashed line is the far-field loading model without the frictionless fault. (b) The relationship between Γ_1 and H. The Γ_1 value for the elastic dislocation model is marked with a grey dashed line.

In another set of models, the local weakness is a broad weak zone below the fault, as proposed in a number of previous studies (Chéry, 2008; Vaghri and Hearn, 2012; Traoré et al., 2014; Yamasaki et al., 2014). Evidence for the presence of a weak zone has been reported for different faults. For example, Papaleo et al. (2018) reported a low-velocity anomaly beneath NAF using S-wave tomography. Chéry (2008) proposed that lateral variations of elastic thickness can influence the strain distribution and that a thin plate associated with a weak zone below the fault can be responsible for the localization of deformation. The role of the weak zone is to reduce the stiffness of the system around the fault. Decreasing crustal rigidity around the fault above the locking depth can also reduce the stiffness and lead to a similar effect (Lindsey et al., 2014). The shape of the weak zone can be variable along strike or among different geological settings, but a uniform 2-D weak zone captures the first-order effect. I use a strengthless "notch" to represent the weak zone (Figure 3.1b). The notch is inviscid and of zero-rigidity and extends from depth D to the bottom of the model, with height $H - D$.

The introduction of the inviscid notch indeed leads to greater localization compared to the frictionless fault models, but still to a much lesser degree than the dislocation model (Figure 3.3a). Similar to the frictionless fault models, increasing H can result in faster near-fault deformation (Figure 3.3b), but again, even in a half space ($H \gg D$), the degree of localization is much less than predicted by the dislocation model. The width of the weak zone does influence the deformation pattern. A wider notch can widen the zone of more localized deformation but decrease Γ_1 very near the fault (Figure 3.4).

The inviscid-notch models here are actually similar to the viscoelastic models of Traoré et al. (2014) and Yamasaki et al. (2014). Traoré et al. (2014) proposed a "notch" model to explain GNSS velocities across the Carrizo segment of SAF. The total thickness of their model is $H = 16D$, and a notch of $W = 5D$ extends from D to the bottom of the model. The notch is filled with a viscoelastic material with $\tau_M \approx 8$ yr, which is essentially inviscid at the late-interseismic stage for a typical SAF recurrence interval of 200 – 300 years (25 - 37.5 τ_M). The rest of the model below the elastic plate is assumed to have $\tau_M \approx 8 \times 10^6$ yr, which is effectively elastic over the earthquake cycles. Therefore, Traoré et al.'s (2014) model can be accurately represented by the elastic half-

space notch model (Figure 3.3a, green solid curve). The main reason why their model features higher localization is that they set the fault-parallel boundary to be not very far to the fault ($F \sim 20D$). The contribution to Γ_1 from the boundary is $D/2F = 0.025$.

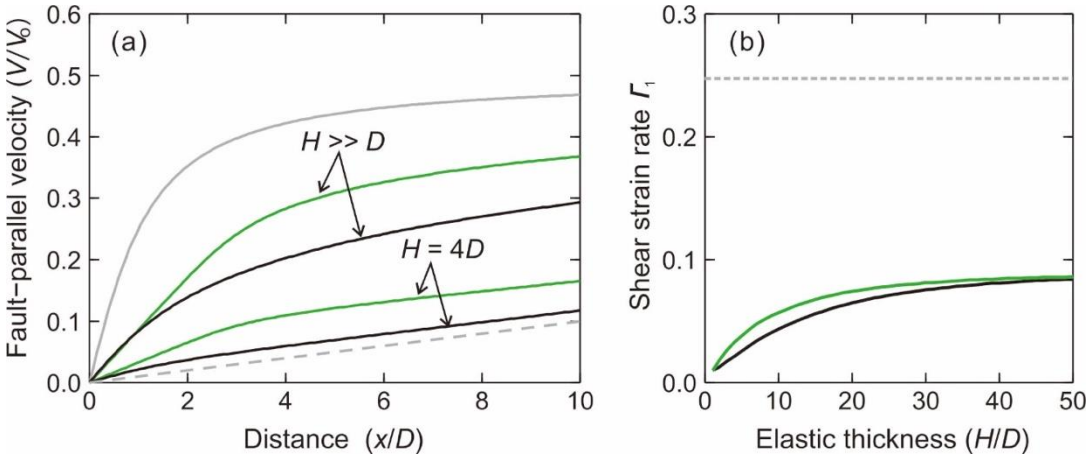

Figure 3.3. Similar to Figure 3.2 but for the strengthless-notch models (Figure 3.1b). (a) Velocity profiles for $W = 5D$ (green curves) in comparison with the frictionless fault models (black solid curves). (b) The relationship between Γ_1 and H for the notch models (green) in comparison with that of the frictionless fault model (black). Grey dashed line marks Γ_1 of the elastic dislocation model.

Similar to Traoré et al (2014), Yamasaki et al. (2014) introduced a notch-like weak zone in a viscoelastic model to explain late-interseismic deformation around NAF before the 1999 İzmit and Düzce earthquakes. However, the total thickness of their model including an elastic layer and a viscoelastic asthenosphere is only $2.5D$ or $5D$. The weak notch is filled with materials of $\tau_M \approx 1$ or 2 yr, and the surrounding asthenosphere is assumed to have $\tau_M \approx 200$ yr. Considering a typical T for NAF of 200~300 yr, the weak notch behaves like our inviscid notch at the late-interseismic stage. Regardless of the numerous earthquake cycles simulated through the modelling, the high-viscosity asthenosphere tends to behave elastically. Therefore, the late-interseismic results of the model closely reflect the response of an elastic plate with an inviscid notch to far-field loading (Figure 3.3a).

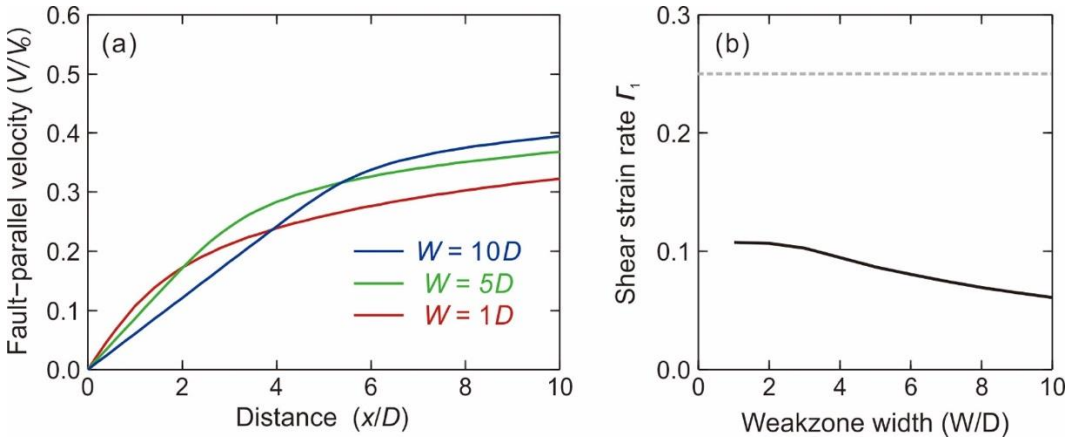

Figure 3.4. The influence of the width of the strengthless notch (Figure 3.1b) on surface deformation. (a) Velocity profiles for different W values. (b) The relationship between Γ_1 and W. Grey dashed curve marks Γ_1 of the elastic dislocation model.

3.2. Weakness Along Strike

The presence of creeping segments seems to be common in real faults, including some of the faults in Figure 1.3, such as SAF (Titus et al., 2006, 2011), NAF (Kaneko et al., 2013; Cetin et al., 2014; Bilham et al., 2016) , the Dead Sea Fault (Hamiel et al., 2016), and the Altyn Tagh (Shen et al., 2018). I employ frictionless faults, the weakest possible, to represent freely creeping segments and investigate how they affect the deformation around locked segments under far-field loading ($V_1(x)$). The effect on V_1 can be illustrated using elastic models similar to those in Section 3.1.

In the first example, only a central segment (locking length L) of the fault is locked from the surface to depth D, and the rest of the fault is frictionless and free to creep under far-field loading (Figure 3.5a). The locking–creeping transition causes some fault-normal displacements, and therefore, strictly speaking, the model is no longer symmetric with respect to the fault. However, the fault-normal displacements are much smaller than the fault-parallel displacements. The comparison with a full-domain model (Figure 3.5c) shows that the half-domain model still yields reasonable results in the fault-parallel direction. I therefore continue to use half of the model domain for the modelling in this section.

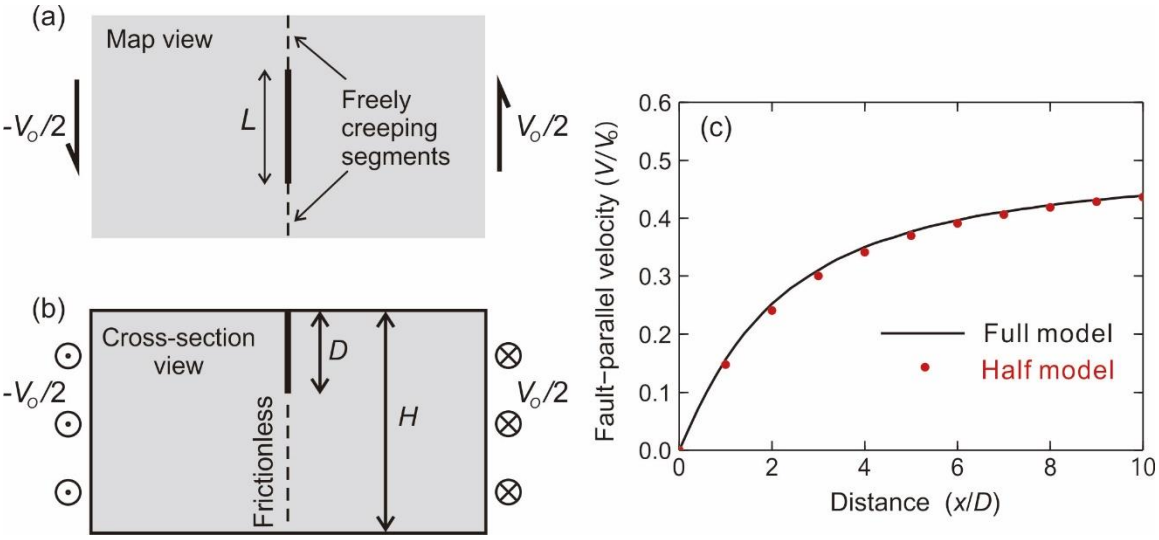

Figure 3.5. One locked segment between two extremely long freely creeping segments. (a) Map view of the model. (b) Cross-section view of the model (through the locked fault). (c) Comparison between results obtained with the full-domain and half-domain models. For both models, $L = 10D$, and the velocity profile is through the centre of the locked segment.

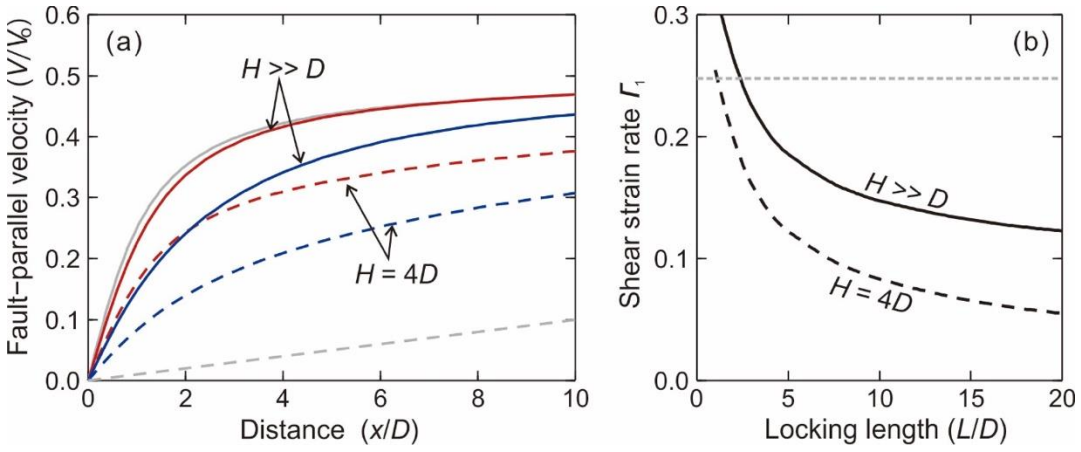

Figure 3.6. 3-D models of elastic half-space ($H \gg D$) and plate ($H = 4D$) to show the effects of two freely creeping segments sandwiching a locked segment (Figure 3.5). (a) Velocities along a profile crossing the centre of the locked segment of different L values (red for $L = 3D$ and blue for $L = 10D$). Grey curves are the same as in Figures 3.2 and 3.3. (b) The plot of Γ_1 vs. L/D. Grey dashed line marks Γ_1 of the elastic dislocation model.

As shown in Figure 3.6, the extremely long creeping segments (extending to fault-normal model boundaries) serve to load the locked segment in the near field but only to a limited degree unless the locking length L (Figure 3.5a) is very short. For example, the surface deformation of the $L = 10D$ model in a half space (solid blue curve in Figure 3.6a) is more localized than the 2-D frictionless fault model in Section 3.1 (Figure 3.2). However, it is still not as localized as the dislocation model. Decreasing L to $3D$ in a half space (red solid curve in Figure 3.6a) can match the dislocation model, but it may not be a representative situation in real Earth.

The type of model discussed above (Figure 3.5) is an end-member scenario, in which the creeping segments are "infinitely long" (extending to fault-normal model boundaries). In an opposite end-member scenario, a frictionless creeping segment is located between two infinitely long locked segments (Figure 3.7a). Again the fault below depth D is frictionless (Figure 3.5b). Figure 3.7b shows deformation along fault-normal profiles at distances $B = 1D$ and $10D$ from the locking-creeping transition. The results show very limited influence of the relatively short creeping segment on the nearby locked segments (Figure 3.7). The influence is smaller farther away from the locking-creeping transition, as illustrated by the comparison between the deformation profiles at $B = 1D$ (red curves in Figure 3.7b) and $B = 10D$ (blue curves in Figure 3.7b). Increasing the length of the central creeping segment does not significantly enhance localization (Figure 3.7c).

In the third type of model, I consider an infinitely long creeping segment abutting an infinitely long locked segment (Figure 3.8a). The results also show the limited effect of the creeping segment on the locked segment (Figure 3.8b). Close to the creeping-locking transition (e.g., $B = D$), near-field loading from the creeping segment has a greater impact (Figure 3.8c), but the effect is too small to match the dislocation model.

There are many arrangements of locking and creeping segments and combinations of their lengths, but the physical process is already adequately illustrated by the three selected cases. In a system loaded by far-field motion alone, provided the locked fault is long, freely creeping of nearby segments cannot localize the deformation to a high degree.

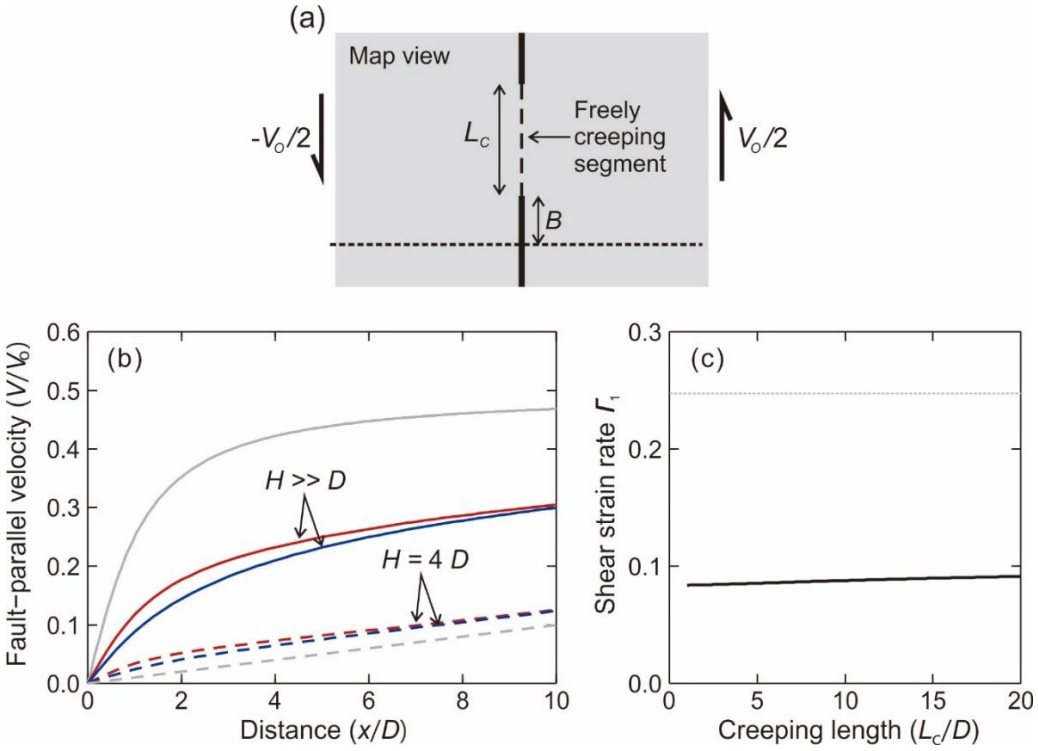

Figure 3.7. Effects of a freely creeping segment of length L_c on deformation around adjacent infinitely long locked segments. (a) Map view. (b) Velocities along profiles at different distances B from the locking-creeping transition, with red and blue for $B = 1$ and $10D$, respectively. Grey curves are the same as in Figures 3.2 and 3.3. (c) Plot of Γ_1 vs. L_c/D for the models of elastic half-space ($H \gg D$). Grey dashed line marks Γ_1 of the elastic dislocation model (0.25).

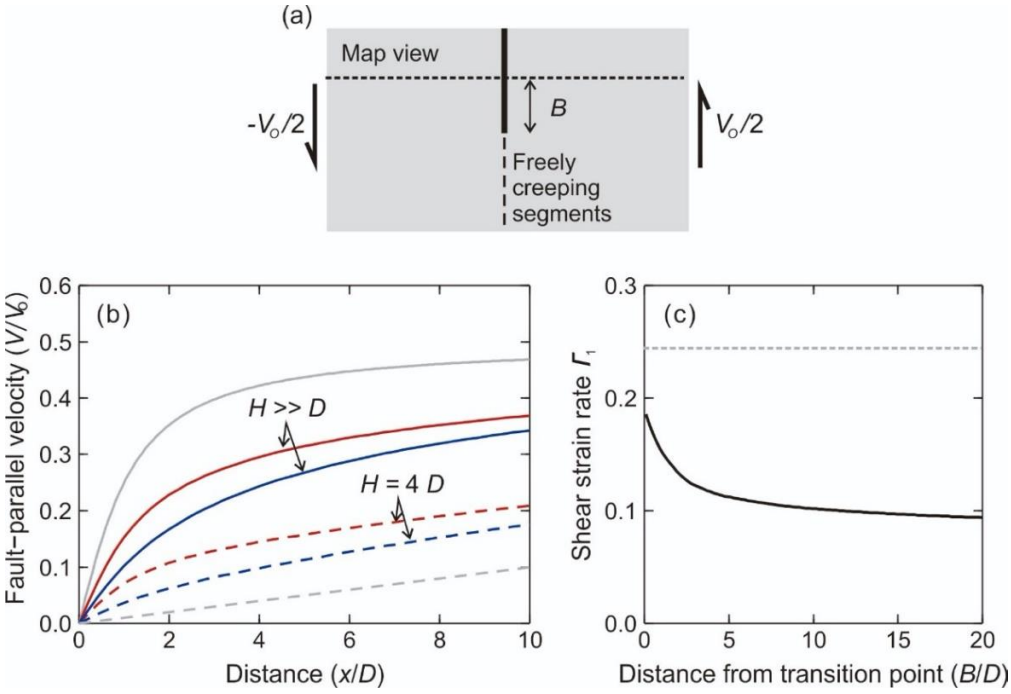

Figure 3.8. Effects of an infinitely long creeping segment on deformation around its neighbouring infinitely long locked fault. (a) Map view. The dashed line indicates profile shown in Figure 3.8 (b). (b) Velocities along profiles at different distances B from the locking-creeping transition, with red and blue for $B = D$ and $10D$, respectively. Grey curves are the same as in Figures 3.2 and 3.3. (c) Plot of Γ_1 vs. B/D for models of elastic half-space ($H \gg D$). Grey dashed line marks Γ_1 of the elastic dislocation model (0.25).

Chapter 4: Earthquake Cycles in Viscoelastic Earth

On the basis of the modelling results discussed in **Chapter 3**, it is clear that contributions from far-field loading generally cannot explain the widely reported localized interseismic deformation represented by the arctangent curve in Figure 1.3, even in the presence of weaknesses below and /or along strike. In this chapter, I will use simple models to demonstrate that the localization of deformation depends mainly on the contribution from previous earthquakes. I will explore the general mechanical process of earthquake cycles of strike-slip faults and identify key factors that control the deformation pattern.

4.1. Recurrence Interval and Localization

Previous studies have incorporated earthquake cycles in a viscoelastic Earth to investigate the effects of past earthquakes using analytical and semi-analytical mathematical models (e.g., Savage and Prescott 1978a; Cohen and Kramer, 1984; Savage, 2000; Smith and Sandwell, 2004; Hetland and Hager, 2005) or using the finite-element method (e.g., Takeuchi and Fialko, 2012; Meade et al., 2013; Yamasaki et al., 2014; Hearn and Thatcher, 2015). These models predict much more localized interseismic deformation than can be induced by far-field loading alone. In this section, I will use simple Maxwell models to demonstrate that, given viscosity, the recurrence interval T of earthquakes plays a dominant role in controlling the degree of localization.

The superposition method I use to obtain solutions for the earthquake cycle models from that of the single-earthquake model has been described in Section 2.4. Different from the models in **Chapter 3**, the earthquake-cycle models combine the contributions from both far-field loading and previous earthquakes (equations (2.12) and (2.13)). Similar to some of the previous studies, I employ periodic earthquakes with a regular recurrence interval T (Figure 2.6). The surface deformation of the earthquake-cycle models shown in here is cycle-invariant, and technical details about the "spin-up" process to achieve cycle invariance have been presented in Section 2.4.2. In the real Earth, faults with a greater recurrence interval T usually are accompanied with a slower geological slip rate V_o. If we assume that faults with different T values have the same slip $U_0 =$

$V_o \times T$ in each earthquake, T is then inversely proportional to slip rate V_o. For generality, velocities in this chapter are normalized by each model's own V_o unless otherwise specified.

Figure 4.1 shows how velocity profiles evolve with T in Maxwell earthquake cycle models at the mid-interseismic ($t = 0.5T$) and late-interseismic ($t = T$) stages. For these models, τ_M is taken to be 10 yr, but other τ_M values will yield identical results because results at t as a fraction of T depend only on the T/τ_M ratio (Section 2.4.3 and Figure 2.11). It is clear that T controls the pattern of localization in interseismic deformation (Figure 4.1): A small T brings the velocity profiles closer to the arctangent curve of the elastic dislocation model, but a very large T results in widely-distributed interseismic deformation. Results of the Burgers models with $\tau_K = 0.1\tau_M$ show a similar pattern (Figure 4.2), but the deformation is less localized because the lower viscosity just after the earthquake leads to faster stress relaxation and hence more distributed deformation.

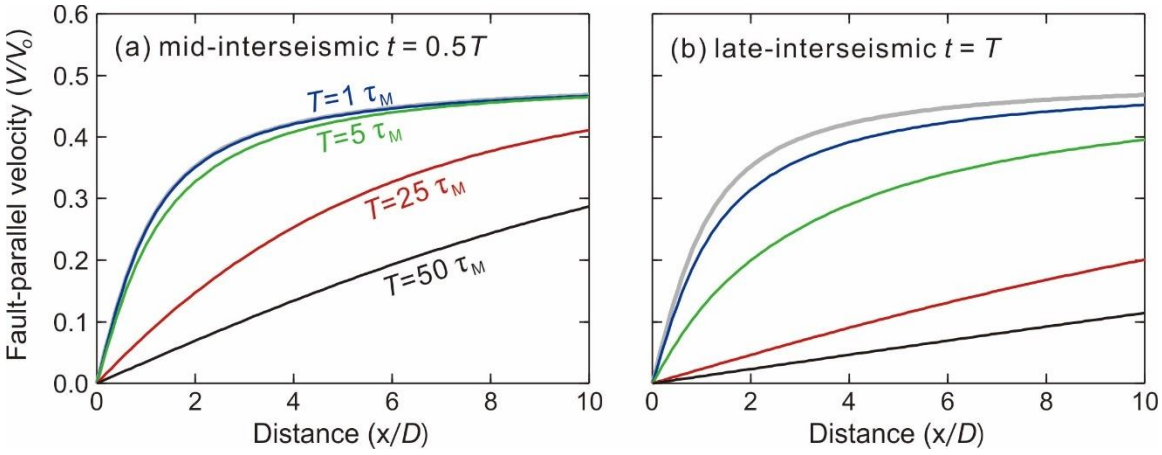

Figure 4.1. Surface deformation in Maxwell models at different stages of the earthquake cycle. Models of different recurrence intervals are shown in different colours as labelled in (a). The elastic dislocation model is shown for comparison (gray line). (a) and (b) Mid-interseismic, and late-interseismic deformation, respectively.

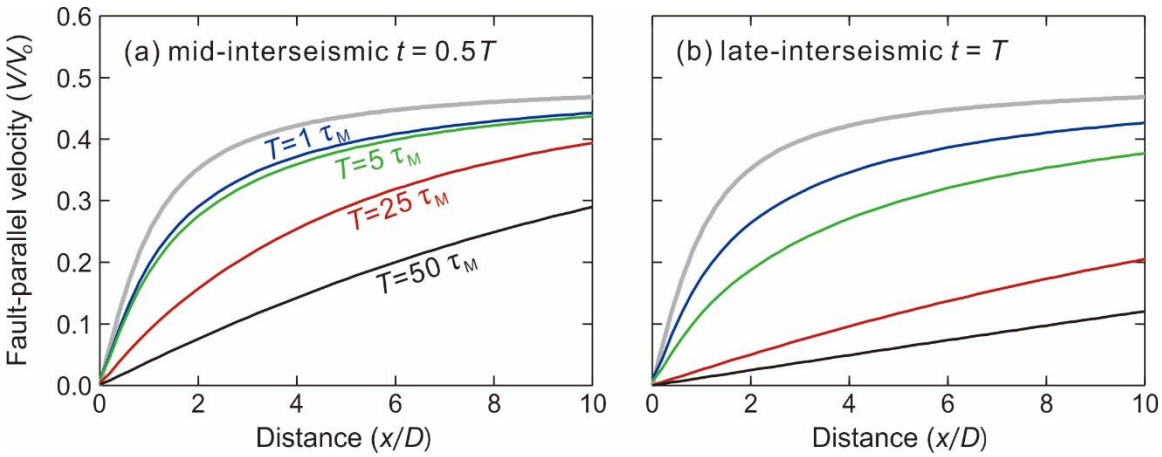

Figure 4.2. Similar to Figure 4.1 but for Burgers models ($\tau_K = 0.1\tau_M$).

For both the Maxwell and Burgers rheology, models with a short T (e.g., $T = 1\ \tau_M$) resemble the elastic dislocation model (gray curve in Figures 4.1 and 4.2). Even with a moderately long T (e.g., $T = 5\ \tau_M$), the mid-interseismic deformation can still be approximated by the elastic dislocation model if a $D_G > D$ and a V_o smaller than the actual value are used (equation (1.1)). For a very long T (e.g., $T = 50\ \tau_M$), the effects of previous earthquakes are almost fully relaxed before the next earthquake ($t = T$) so that the contribution from far-field loading is dominant (equation (1.2)), leading to very widely distributed deformation. The Γ_1 values shown in Figure 4.3 illustrate how the degree of localization at the mid- and late-interseismic stages systematically decrease with increasing T. Introducing transient rheology only slightly modifies this behaviour but does not change the basic pattern (Figure 4.3).

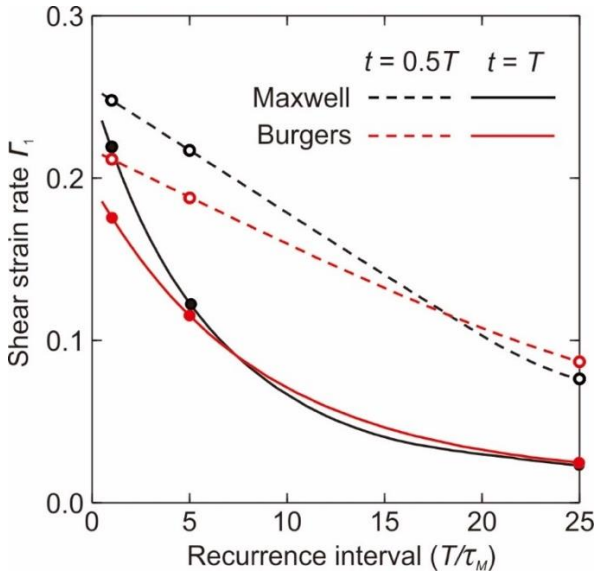

Figure 4.3. Mid- and late-interseismic $\dot{\Gamma}_1$, defined in Section 2.5, for the same types of models as in Figures 4.1 and 4.2 but for a range of T values. Models displayed in Figures 4.1 and 4.2 (except for $T = 50\ \tau_M$) are marked with cycles.

As mentioned earlier in this section, velocities in Figures 4.1 and 4.2 are normalized by each model's own V_o, and the two time points are chosen to represent mid- and late-interseismic stages regardless of the length of T. To provide a sense of the actual differences between the models with different T (or V_o), velocities in Figure 4.4 are not separately normalized by each model's own V_o value but all by a common value V_{o_1} which is the V_o of the $T = \tau_M$ model, and time in this plot is measured in τ_M instead of a fraction of T. All solid curves in Figure 4.4a are the same coloured results as in Figures 4.1b but shown at the actual scale with respect to V_{o_1}. At $t = 5\tau_M$, the models of $T = \tau_M$ and $T = 5\tau_M$ are both in the late-interseismic stage (for $T = \tau_M$, $V(t + 4\tau_M) = V(t)$ because of cycle invariance), but the $T = 25\tau_M$ model is still early in its interseismic period ($t = 0.2T$) and therefore shows rather fast near-fault deformation despite its extremely low V_o. In the same fashion, Figure 4.4b redisplays the results shown in Figure 4.2b.

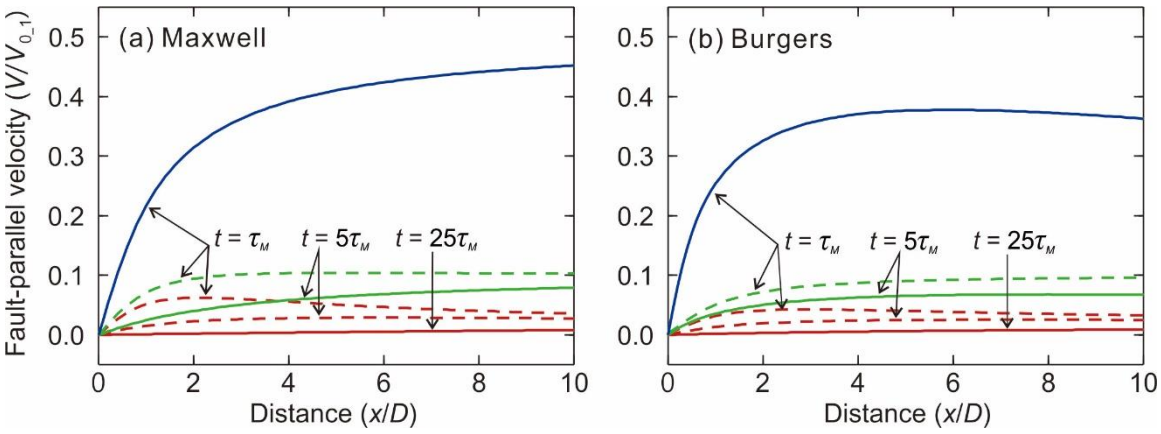

Figure 4.4. Velocities for models of different T (except $T = 50\tau_M$) shown in Figures 4.1 and 4.2 redisplayed at the same scale. (a) Results of the Maxwell models (Figure 4.1) shown at different times measured in τ_M, with all the velocities normalized by the same far-field velocity of the $T = \tau_M$ model V_{o_1}. The solid curves are the same as in Figure 4.1b with the same colours**.** (b) The same as (a) but for Burgers models, and solid coloured curves are the same as in Figure 4.2b.

Because we normalize time by τ_M, the results shown in Figures 4.1 and 4.2 also illustrate the effects of viscosity. For example, the scenario of $T = \tau_M$ represents T = 50 yr if $\eta_M = 5 \times 10^{19}$ Pa s but T = 100 yr if $\eta_M = 10^{20}$ Pa s. Because the results at t/T depends only on the T/τ_M ratio (Section 2.4.1), a high viscosity has the same effects a short T. Viscosity may indeed differ between tectonic settings depending on the geothermal regime, but T still exerts a much greater control on deformation localization. For example, the terrestrial heat flow around the Bohai Sea region shown in Figure 1.5a is about 60 mW/m^2 (Tao and Shen, 2008), no higher than much of the SAF region (Lachenbruch, 1980). On the basis of the heat flow values, we do not expect the viscosity in the Bohai Sea region to be systematically lower than that of the SAF region. The widely distributed deformation represented by the near-zero background velocities 200 km from the Yilan-Yitong and Yishu faults (Figure 1.5) is much better explained by its long T (~4000 yr). For the Yishu fault, here we focus only on the background low velocities (Figure 1.5c) but will explain the second-order higher velocities near the fault in Section 5.1, after discussing the effect of a recent earthquake.

For the sake of argument, if we assume $\eta_M = 5 \times 10^{19}$ Pa s and hence $\tau_M = 50$ yr, T should be ~3 τ_M for SAF but ~80 τ_M for the Yilan-Yitong and Yishu faults. Since the last

major rupture of the SAF Carrizo segment was the M ~ 7.9 1857 Fort Tejon earthquake, about $1T$ ago (Zielke et al., 2010), a deformation pattern between those of the $T = \tau_M$ (blue) and $5\tau_M$ (green) curves in Figure 4.1b or 4.2b should apply to its contemporary deformation, rather similar to what is predicted by the dislocation model (Figure 1.3b). The red curve in Figures 4.5a or 4.5b is late-interseismic ($t = T$) velocity for a Maxwell model of $T = 80\tau_M$ and $V_o = 2.6$ mm/yr. The other model curve in Figure 4.5b will be explained in Section 5.1.

As mentioned in Section 2.5, understanding how the displacement since the last earthquake evolves during one earthquake cycle may help to understand earthquake potential. Figure 4.6 shows displacements for Maxwell and Burgers models with different T at postseismic, mid-interseismic, and late-interseismic stages normalized by the seismic slip U_0. At the postseismic and mid-interseismic stages (Figure 4.6, $t = 0.1T$ and $0.5T$), models with larger T values accumulate more displacements than models with small T values. However, the total displacements of all the models are identical at the end of the interseismic period and are the same as what is predicted by the elastic dislocation model (Figures 4.6d and 4.6f). For models with a large T (e.g., $T = 50\ \tau_M$), most of the displacement is accumulated at an early stage of the cycle. For models with small T (e.g., $T = \tau_M$), the accumulation of displacement is more evenly distributed throughout the cycle.

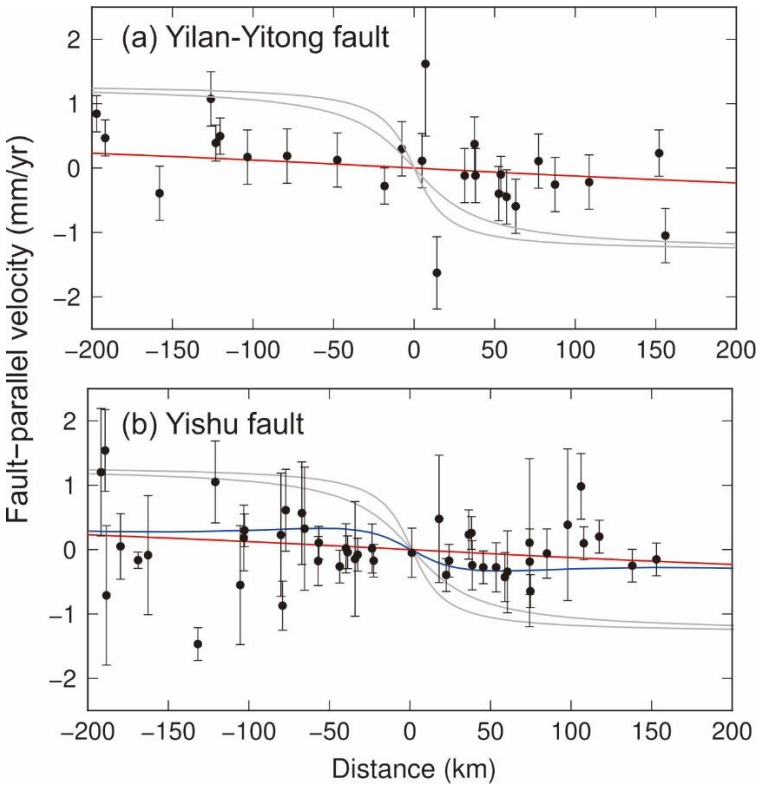

Figure 4.5. GNSS velocity profile across the Yilan-Yitong fault (a) and Yishu fault (b) as has been shown in Figure 1.5 compared with various models. Grey curves are based on the elastic dislocation model (equation (1.1)) assuming $D = 15$ km or 30 km (less localized) and $V_o = 2.6$ mm/yr. The red model curves are based on our earthquake cycle model with $T = 80\tau_M$ and $V_o = 2.6$ mm/yr. The blue model curve will be explained in Section 5.1.

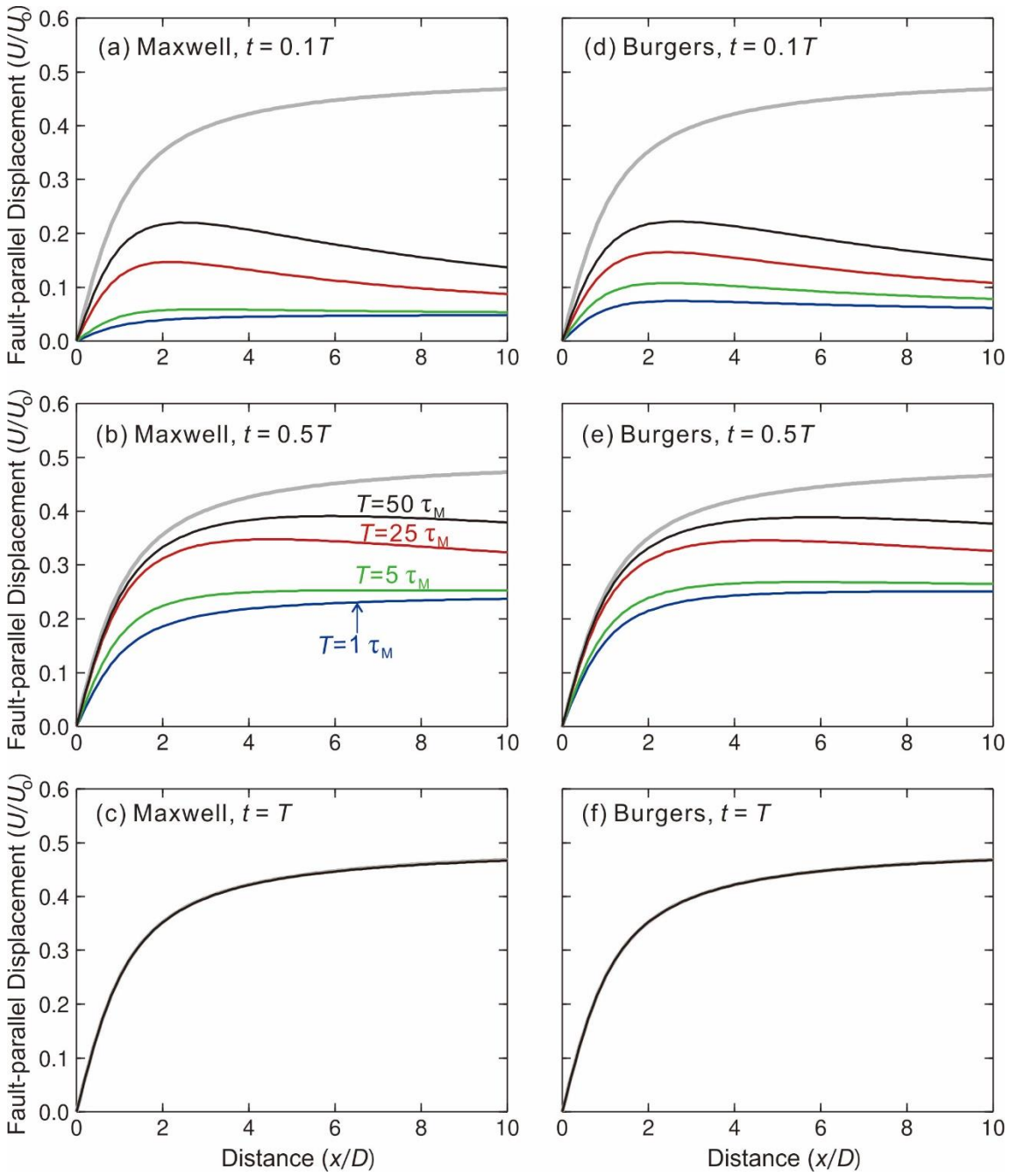

Figure 4.6. Displacements since the last earthquake along a fault-normal profile for Maxwell and Burgers models with different T as labelled in (a). The displacements are normalized by the same U_o which is assumed for all the models. The end-of-cycle displacement predicted by the elastic dislocation model is shown for comparison (grey line). (a), (b), and (c) Postseismic, mid- interseismic, and late-interseismic, respectively, displacement profiles for models with a Maxwell substrate. In (c), all displacement profiles are identical to that of the elastic dislocation model. (d), (e), and (f) The same as (a), (b), and (c), respectively, but for Burgers models ($\tau_K = 0.1\tau_M$).

4.2. Mechanism of Localization

No matter what type of viscoelastic rheology is assumed for the asthenosphere, past earthquakes localize present interseismic deformation for the same reason. The key is that much of the incremental stress induced by these earthquakes has not been relaxed. Note that the induced stress is not to be confused with the background tectonic stress that loads the fault to cause earthquakes. Owing to the linear rheology, we are able to discuss the incremental stress change in earthquake cycles independent of the background stress. The mechanism has been explicitly or implicitly addressed in all previous viscoelastic earthquake-cycle models (e.g., Savage and Prescott, 1978a; Johnson and Segall, 2004; Li and Rice, 1987; Hearn and Thatcher, 2015; Vaghri and Hearn, 2012), but it is useful to clarify it in simple terms as follows.

Coseismic slip in an earthquake induces shear stress in the viscoelastic substrate below depth D in the sense of the fault motion. Relaxation of this induced stress is accompanied with viscous shear flow in the same sense. When the shallow fault is locked after the earthquake, the viscous shear continues, and it loads the locked fault from below to cause localized deformation. The induced stress is high and the shear flow is fast just after the earthquake, responsible for fast postseismic deformation, especially if the postseismic viscosity is low as discussed Section 2.2. If the induced stress is fully relaxed before the next earthquake, due to a long recurrence interval or low viscosity, there is no more viscous shear flow to localize deformation. If each earthquake occurs before the stress induced by its predecessor is fully relaxed, due to a short recurrence interval or high viscosity, the viscous shear is sustained.

To illustrate this process, Figures 4.7a and 4.7b, for Maxwell and Burgers ($\tau_K = 0.1\tau_M$) models, respectively, show fault-parallel velocities at depths below the fault in comparison with those at the surface at various stages of the earthquake cycle with $T = 5\tau_M$. Within about $x = 1.5D$ of the fault, the velocities just below the fault (at depth $1.2D$) are always faster than those at the surface, indicating that the surface localization is driven from below the fault. Figures 4.7c and 4.7d show that, within the same distance range from the fault, displacements below the fault ($1.2D$) are ahead of the displacements at the surface throughout the cycle. This behaviour is independent of T, as illustrated by

the comparison between models with $T = 5\tau_M$ (Figure 4.7) and $T = 10\tau_M$ (Figure 4.8). At greater depths such as $2D$, the effect of the seismic rupture in driving sustained viscous flow is much less, and therefore the velocities are slower than at the surface.

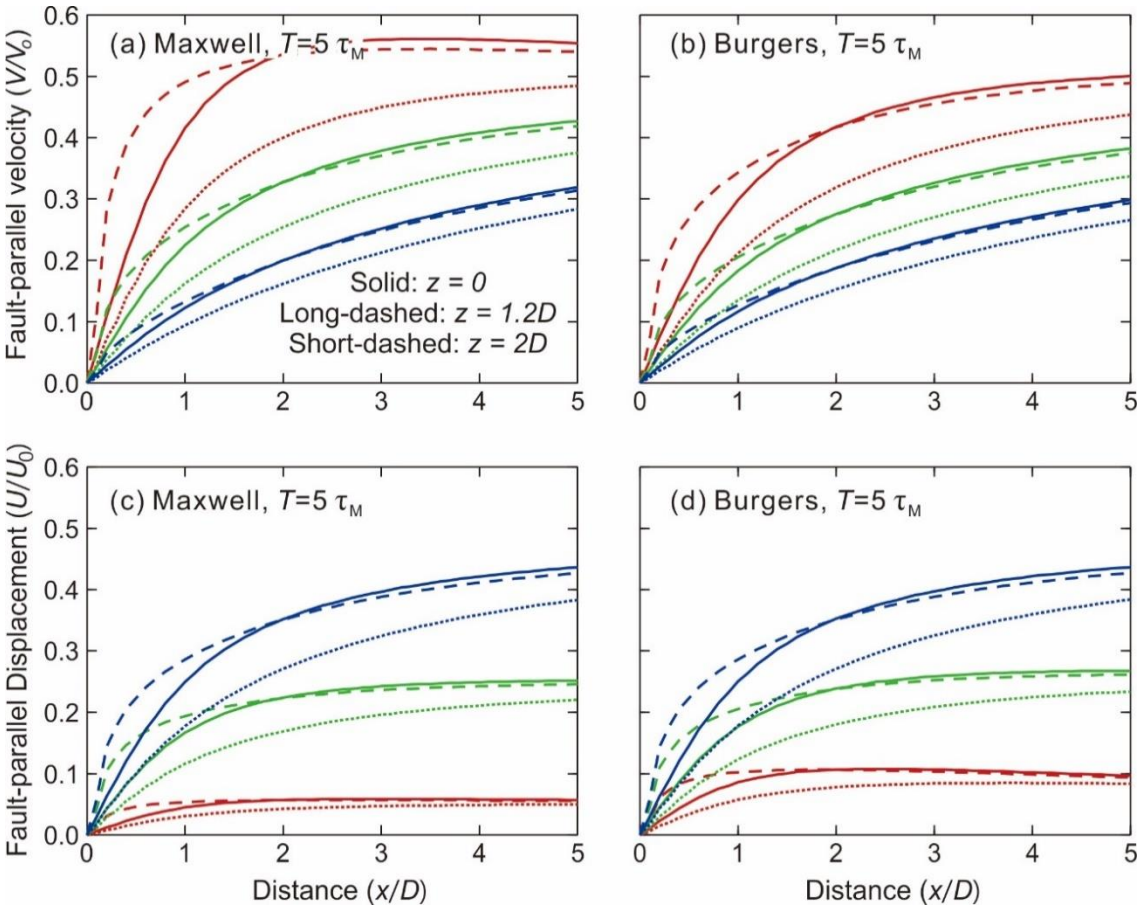

Figure 4.7. Comparison between deformation at the surface (solid lines) and below depth D for models of $T = 5\tau_M$. Red, green, and blue lines are for $t = 0.1T$, $0.5T$, and T, respectively. (a) and (b) Fault-parallel velocities in the Maxwell and Burgers ($\tau_K = 0.1\tau_M$) models, respectively. (c) and (d) Displacements in the Maxwell and Burgers models, respectively.

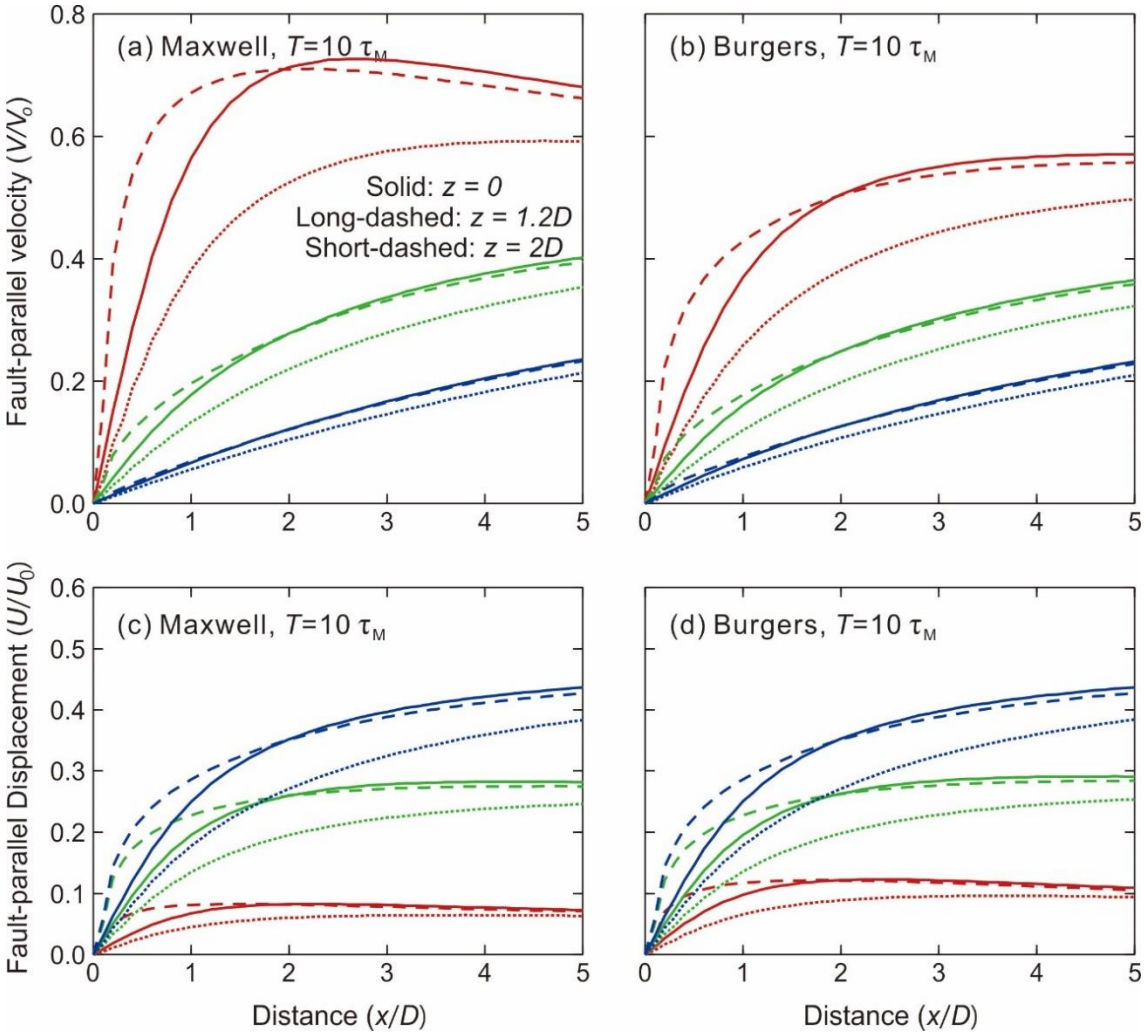

Figure 4.8. The same as Figure 4.7 but for $T = 10\tau_M$.

4.3. Effects of a Weak Shear Zone

The model structure so far considered is the simplest possible for the purpose of this work. Some of the previous viscoelastic earthquake-cycle models included the effect of a weak fault below D by applying nonlinear friction laws or by using a nonlinear rock rheology. We cannot accommodate the nonlinear behaviour using our isothermal linear viscoelastic rheology, but we have designed a number of models to test the effects of including a weak shear zone (Figure 4.9). Six representative models encompassing a moderate range of complexity are listed in Table 4.1.

For simplicity, we only consider a Maxwell substrate (relaxation time τ_M). Mechanical properties in the shear zone not specified in Table 4.1 are the same as the rest

of the viscoelastic substrate. In the first two models in Table 4.1, ShearM and ShearB, a uniform shear zone extends from depth D to the bottom of the model (Figure 4.9a), with Maxwell and Burgers rheology, respectively. In the two "shallow shear zone" models S-ShearM and S-ShearB, the shear zone has the same properties as in ShearM and ShearB, respectively, but extends only to depth $2D$ (Figure 4.9b). The two "double-segment shear zone" models D-ShearM and D-ShearB are modified from S-ShearM and S-ShearB, respectively, by adding a lower shear zone below $2D$ with somewhat different properties (Figure 4.9c). The width of the shear zone W has a minor effect on the results, as illustrated in Figure 4.10 using model ShearM. I fix W to be $0.2D$ for all six shear zone models listed in Table 4.1.

Table 4.1. Maxwell relaxation time τ_{M-S} and Kelvin relaxation time τ_{K-S} for the six shear-zone models, both measured in τ_M of the viscoelastic substrate. The width of the shear zone is $0.2D$. The "upper" part of the shear zone extends from D to $2D$, and the "lower" part from $2D$ to model bottom.

Model name	Description	τ_{M-S} upper	τ_{K-S} upper	τ_{M-S} lower	τ_{K-S} lower
ShearM	Uniform Maxwell	0.1	-	0.1	-
ShearB	Uniform Burgers	1	0.1	1	0.1
S-ShearM	Shallow Maxwell	0.1	-	-	-
S-ShearB	Shallow Burgers	1	0.1	-	-
D-ShearM	Double-segment Maxwell	0.1	-	0.5	-
D-ShearB	Double-segment Burgers	1	0.1	1	0.5

Velocities along fault-normal profiles for models with $T = \tau_M$, $5\tau_M$, and $25\tau_M$ are shown in Figure 4.11. Models with a broader range of T values are summarized in Figure 4.12 using the Γ_1 values. The results show that, regardless of the fault zone complexity, the key controlling factor for the localization of late-interseismic deformation is still the recurrence interval. The interseismic velocities shown in Figure 4.11 are not fundamentally different from those without the shear zone (Figure 4.1), except that

deformation is slightly less localized. In Figure 4.12, all the shear zone model curves are below the gray reference Γ_1 curve for the Maxwell model of no shear zone.

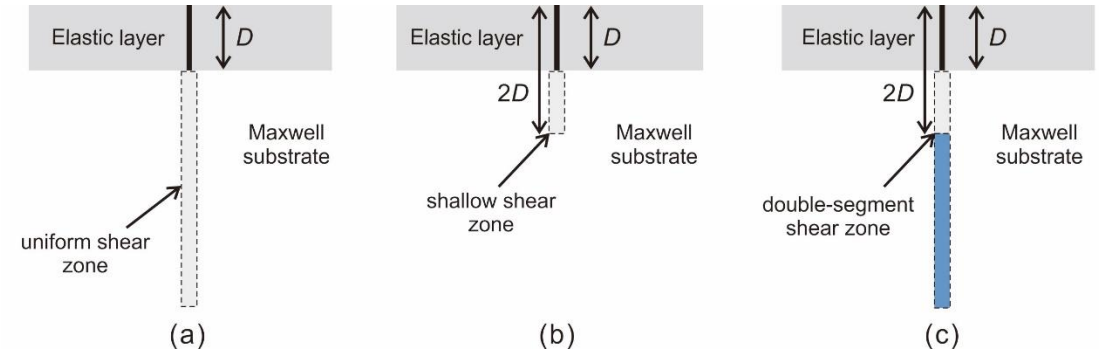

Figure 4.9. Schematic illustrations of three types of shear zone in cross-section views. (a) Uniform shear zone that extends from D to the bottom of the model (ShearM and ShearB in Table 4.1). (b) Shallow shear zone from D to $2D$ (S-ShearM and S-ShearB in Table 4.1). (c) Double-segment shear zone that has two segments ($D-2D$ and below $2D$) with different rheological parameters (D-ShearM and D-ShearB in Table 4.1).

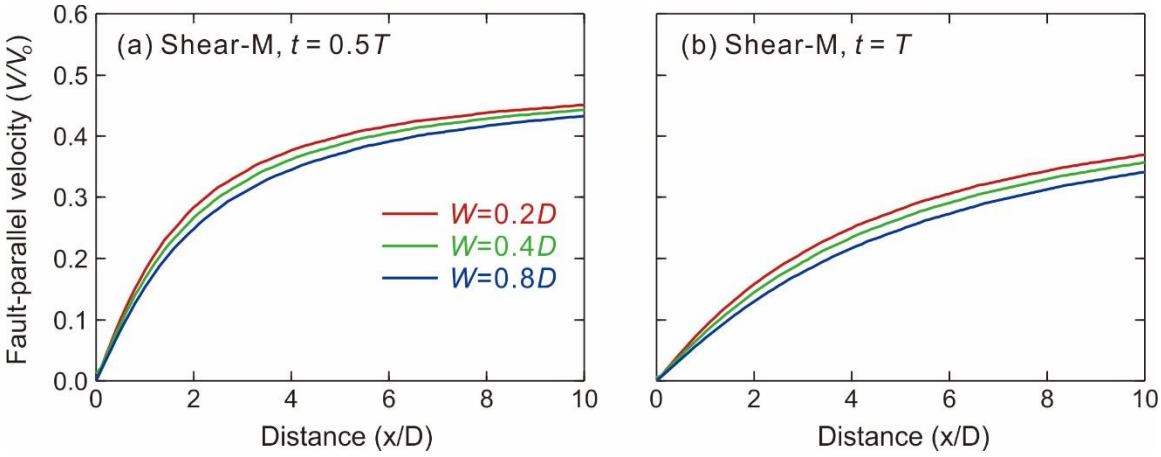

Figure 4.10. Effects of shear zone with W in the uniform Maxwell shear zone model ($T = 5\tau_M$). (a) and (b) Mid- and late-interseismic, respectively, velocity profiles.

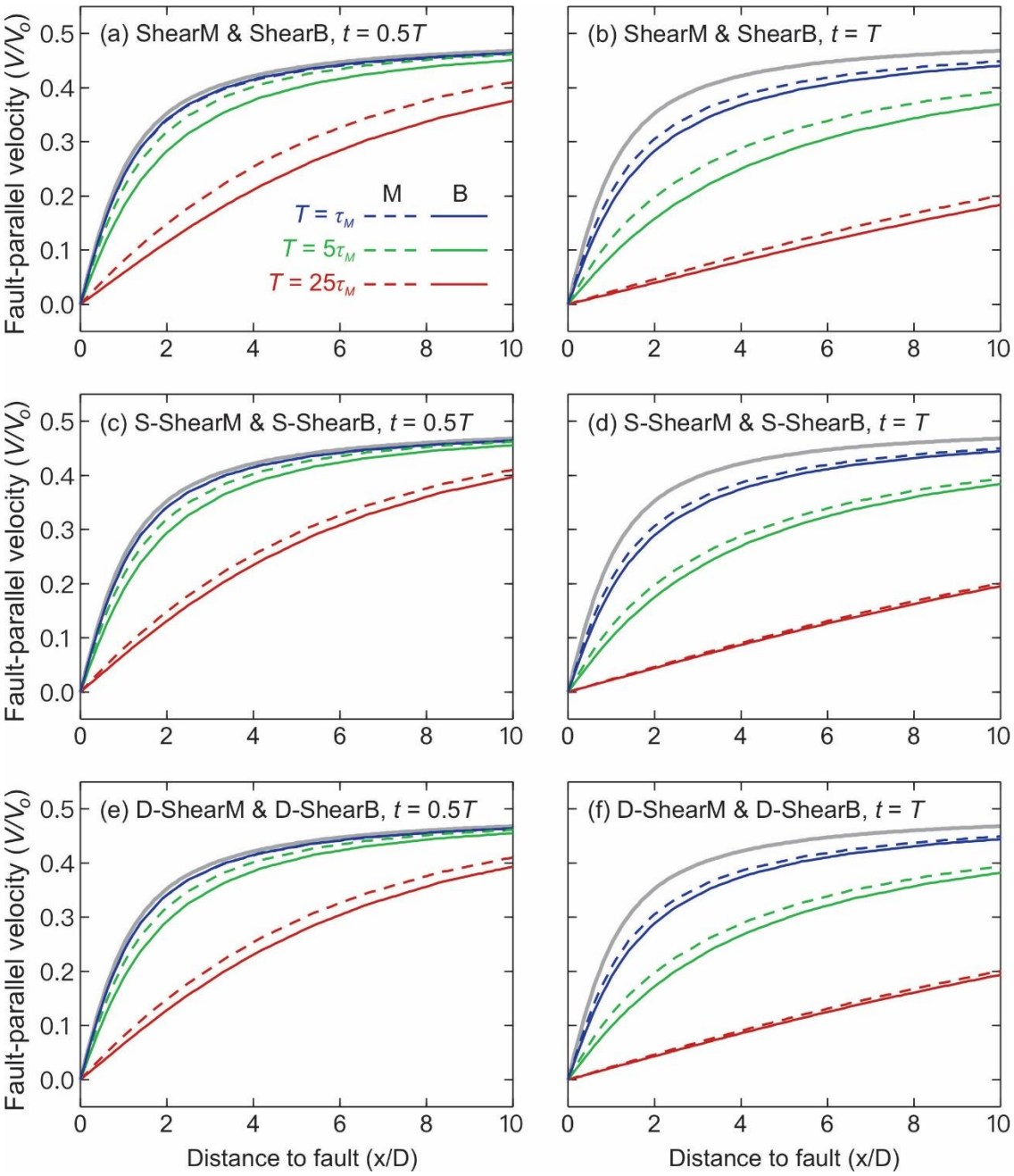

Figure 4.11. Fault-parallel surface velocities along a fault-normal profile for 2-D shear zone models as defined in Table 4.1. The dislocation model (equation (1.1)) with $D_G = D$ is shown for comparison (gray line). Line colour represents T value, and line style represents model type, as defined in the legend in (a), where M and B respectively stand for Maxwell and Burgers rheology of the shear zone. (a) and (b) Mid- and late-interseismic deformation, respectively, for the two uniform shear zone models. (c) and (d) The same as (a) and (b), but for the two shallow shear zone models. (e) and (f) The same as (a) and (b), respectively, but for the two double-segment shear zone models.

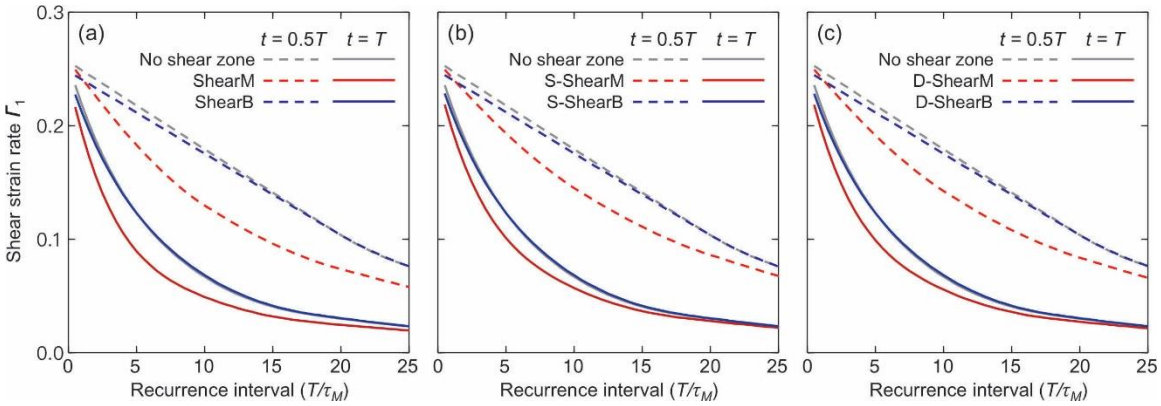

Figure 4.12. Similar to Figure 4.3 but for 2-D Maxwell earthquake-cycle models with different types of shear zones (Figure 4.9). Model names and rheological parameters for the shear zone are given in Table 4.1. Results for models with no shear zone are shown for comparison. (a) Uniform shear zone that extends from D to model bottom. (b) Shallow shear zone that extends from D to $2D$. (c) Double-segment shear zone that has two segments ($D-2D$ and below $2D$) with different rheological parameters.

In localizing mid- and late-interseismic deformation, the presence of a weak deep fault enhances the effect of far-field loading (V_1 in equation (2.12)) as discussed in Section 3.1 but reduces the effect of past earthquakes (V_2 in equation (2.12)). The latter is because the low-viscosity shear zone gives rise to faster relaxation of the earthquake-induced stress. As shown in Figures 4.13a, , 4.13c, and 4.13e, for the Maxwell shear zone models, the viscous flow just below the fault (velocity profiles at depth $1.2D$) is faster than in models without the shear zone at $t = 0.1$ due to the faster relaxation. For the Burgers shear zone models, this effect is not explicit in Figures 4.13b, 4.13d, and 4.14f. This is because of the very small Kelvin relaxation time of the shear zone $\tau_{K-S} = 0.1\tau_M = 0.01T$. By time $t = 0.1T$, the earliest time shown in these figures, this phase of early stress relaxation had long been completed.

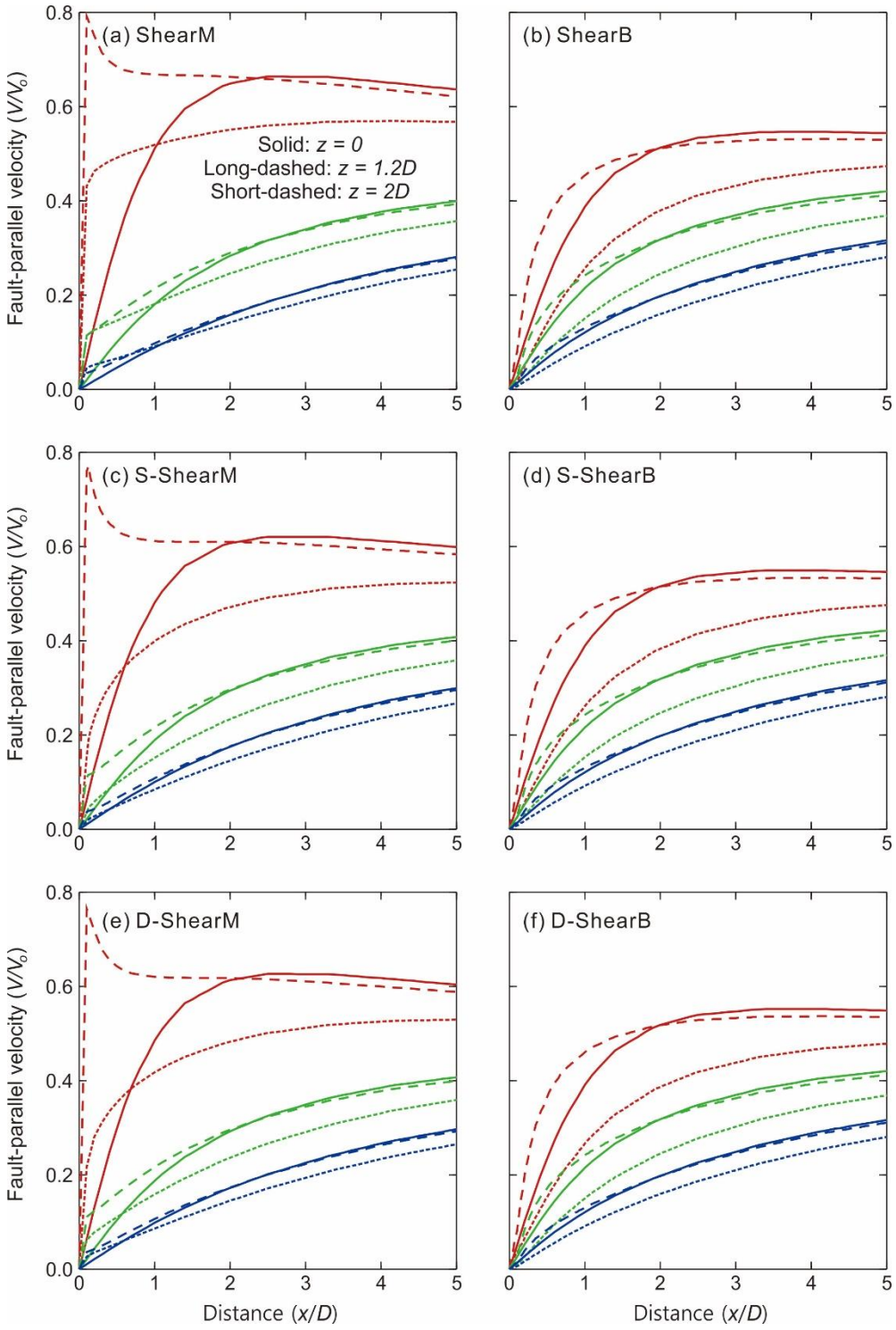

Figure 4.13. Velocity profiles at depths (dashed) to compare with those at the surface (solid lines) for the six shear zone models with $T = 5\tau_M$. Red, green, and blue lines are for $t = 0.1T$, $0.5T$, and T, respectively. (a) through (f) Results for different shear zone models as labelled.

4.4. Implications

4.4.1. Why is Localization Widely Observed?

Although I make no effort to scrutinize site-specific processes of individual faults, the generic results based on the simplest models can explain first-order observations in Figure 1.5 as well as the more commonly reported pattern in Figure 1.3. If localized (Figure 1.3) and distributed (Figures 1.4 and 1.5) interseismic deformation are consequences of the same mechanical process, why is the former much more widely observed? It may largely reflect a bias in geodetic observations.

- Faults with faster V_o allow a better geodetic signal-to-noise ratio. They attract more research and yield better data, but they also tend to be associated with shorter T and hence feature more localized deformation.
- Faults that recently produced large earthquakes also attract more research. Many reported interseismic data may actually depict mid-interseismic deformation, so that the results in Figures 4.1a and 4.2a may be more applicable than those in Figures 4.1b and 4.2b. Even for a fault with very long T, a single earthquake a few hundred years ago may still leave a geodetic signal, as will be discussed in Section 5.1, that could be misidentified as localized late-interseismic deformation.
- Faults that have very low V_o such as the vast majority of short continental faults that extend tens of kilometres do not produce significant geodetic signals even if they are closely monitored. They thus are rarely considered in the discussion of localization.

4.4.2. Understanding Geodetic Locking Depth

The commonly used geodetic locking depth D_G is derived by fitting equation (1.1) to geodetic observations. It is a useful parameter that characterizes complex reality using a single constant, just like the effective elastic thickness of the lithosphere, the coefficient of friction of a fault, the Newtonian viscosity of the asthenosphere, the permeability of a geological formation, and so forth. However, the value of D_G should not be taken literally and applied directly to hazard assessment and geodynamic analysis.

A D_G can be obtained by fitting equation (1.1) to many of the velocity profiles such

as in Figures 4.1, especially if V_o is not independently constrained by reliable geological observations. For example, the mid- and late-interseismic deformation of the $T = \tau_M$ and $5\tau_M$ models in Figure 4.1 can all yield a geologically reasonable D_G if V_o is simultaneously determined by fitting geodetic data. In a viscoelastic Earth, the D_G obtained this way may be larger or smaller than D, depending on the earthquake history of the region. It would be difficult to obtain a D_G value from Figures 1.4b and 1.4c or the $T = 25\tau_M$ curves of Figure 4.1. Practical difficulties caused by the viscoelastic Earth rheology to the interpretation of geodetic observations have also been addressed by other workers, especially with regard to the determination of V_o in the absence of quality geological constraints (e.g., Chuang and Johnson, 2011; Johnson, 2013). Even in an elastic Earth model, the depth of full locking decreases with time over the interseismic period if the fault obeys a rate-and-state dependent friction law (e.g., Shimamoto and Noda, 2014), an issue that is beyond the scope of this study.

Chapter 5. Along-strike Variations and Oblique Faulting

In **Chapter 4**, we have only considered a 2-D strike-slip fault that is uniform along strike in terms of structure and slip kinematics. In this chapter, I will investigate 3-D effects of earthquakes that are not addressed in previous chapters. The fault structure is still 2-D, the same as in Chapter 4, but three different situations of slip kinematics are considered in this chapter: A recent single earthquake of short rupture length (L), a migrating rupture sequence along the same fault, and an earthquake segment surrounded by full-rate creeping segments. I make no effort to sweep the parameter space but only provide a few examples to illustrate the important points. For this purpose, it is adequate to use only the Maxwell model. I use the same model structure as that for **Chapter 4**. However, because finite-length rupture causes fault-normal displacements, I use the full system as shown in Figure 5.1 for the calculation instead of only half of the system as for the 2-D models. In reality, many faults are not vertical, and there may be an additional thrust- or normal-motion component in fault slip. At the end of this chapter, I will briefly discuss models of oblique faulting.

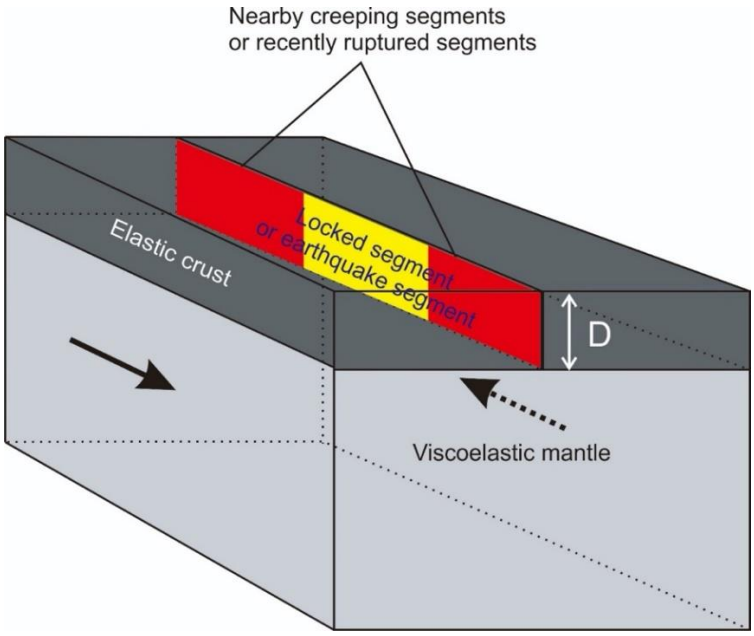

Figure 5.1. Schematic view of a 3-D strike-slip fault loaded from far-field. The yellow part of the fault represents the locked segment of our interests, which is surrounded by along-strike variations (red) including nearby creeping segments and nearby locked segments of different rupture time.

5.1. Recent Single Earthquake of Short Rupture Length

Obviously, stress induced by a short rupture is limited to a smaller area than a 2-D rupture, and therefore its relaxation process takes less time. If all the segments of a fault have a very long recurrence, and large earthquakes in or near the region of interest all occurred a long time ago, the late-interseismic results of a 2-D model of long T such as the black curve in Figure 4.1. can approximately apply. However, if an earthquake of short rupture length occurred recently, its effect can be pronounced. In Figure 5.2, I show fault-parallel velocities along fault-normal profiles at selected time points ($t/\tau_M = 1$, 5, and 10) after single earthquakes of the same slip $U_o = 10$ m but different rupture lengths $L/D = 1$, 5, and 10 in a system with $\tau_M = 20$ yr. The results are anti-symmetric with respect to the centre of the rupture. With no surprise, the rate, duration, and affected area of deformation after an earthquake all increase with L.

Results similar to those in Figure 5.2 can be used to predict possible second-order higher velocities near the Yishu fault due to the 1668 Tancheng earthquake (Figure 4.5b). This earthquake ruptured the southernmost portion of the segment shown in Figure 1.5a. It caused significant damage, but its magnitude, rupture area, and average slip are very poorly known. Given its estimated ~130 km rupture length, its magnitude can be nowhere near the commonly quoted 8.5, as also pointed out by Jiang et al. (2017). A slip of up to ~8 m has been inferred from limited paleoseismic studies with large uncertainties (Huang, 1993; Jiang et al., 2017). If we assume that the earthquake occurred 7 τ_M ago ($\tau_M = 50$ yr) with average slip $U_o = 5$ m and $L = 5D$ ($D = 15$ km), we can predict deformation due to this event as seen today. Adding the predicted deformation along a fault-normal profile at $y = 5D$ from the centre of the rupture to the background deformation (red line), I obtain the pattern illustrated using a blue line in Figure 4.10b, but other combinations of parameters can lead to similar results. Here I use $y = 5D$ because most of the GNSS measurements shown in Figure 4.10b are at some distance from the reported epicentral area in the strike direction (Figure 1.5a). The effect of the 1668 earthquake is largely within the errors of the GNSS observations.

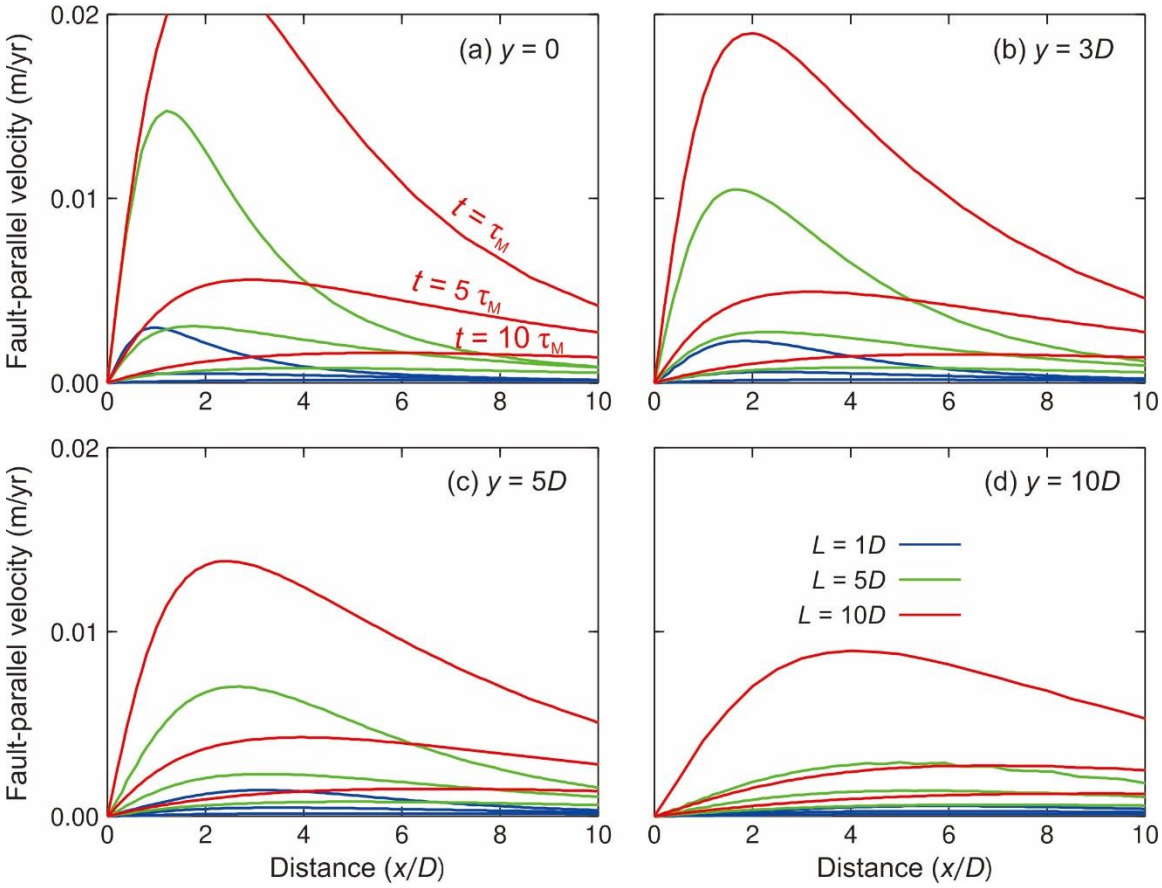

Figure 5.2. Surface velocity profiles following a single earthquake of finite rupture length L. Results for different rupture lengths are colour coded as shown in (d). For each L, the three lines are for $t = 1\tau_M, 5\tau_M,$ and $10\tau_M$ in order of decreasing amplitude, as illustrated in (a) using the $L = 10D$ example. (a), (b), (c) and (d) Results along fault-normal profiles at shown distances from the centre of the rupture.

5.2. Migrating Rupture Sequence

It is important to consider how the seismic rupture of nearby segments of the same fault affects localization around a locked segment. For a fault of very long T such as $> 50\tau_M$, this effect is somewhat addressed by the single-earthquake examples in Section 5.1. Here I use three types of migrating-rupture models to illustrate the effect for faults of moderately long T. More common is the rupture of different segments at different times without a clear spatiotemporal pattern of migration. The use of idealized migrating-rupture sequences is for the convenience of modelling, but the results convey a general message. Besides, migrating rupture is indeed documented along some large faults, most notably NAF (Şengör et al., 2005).

In the first of the three types, the fault consists of 10 equal-length ($L = 10D$) segments (Figure 5.3a). They all have the same T but rupture one after another with a regular migration interval T_m. I use the finite element model to simulate the response of the system to a single "Green's function" earthquake and accomplish migration and spin-up by convolution, similar to the method of superposition described in Section 2.4. I assume $T_m = 0.1T$, such that the length of the "super cycle" of 10 earthquakes is also T. After completing the super cycle, the migration sequence repeats itself. I test models with $T = 5\tau_M$ and $10\tau_M$.

I use the fifth segment (white in Figure 5.3a) as the observation segment and examine fault-parallel velocities along a fault-normal profile crossing its centre. In Figures 5.3b and 5.3d, time counting starts from the last rupture of the observation segment ($t = 0$), and each curve is the deformation pattern $0.1T$ after the rupture of the segment of the same colour in Figure 5.3a, just before the rupture of the next segment. For example, the green curve in Figure 5.3b shows deformation $0.1T$ after the rupture of the green segment in Figure 5.3a which ruptured at $t = 0.3T$ after the last rupture of the observation segment itself. For comparison, Figures 5.3c and 5.3e show the results of 2-D models in which the observation segment is infinitely long without any other segments.

The comparison between the migrating-rupture model (Figure 5.3b or 5.3d) and the corresponding 2-D model (Figure 5.3c or 5.3e) shows that the rupture of nearby segments of the same fault enhances localization around the observation segment. The earlier, receding earthquakes (e.g., red and green) are less impactful, because the deformation field is still dominated by the effect of the last rupture of the observation segment itself. The later, approaching events (e.g., orange and light-blue) are more impactful. In contrast, at the same stages in the 2-D case, there is no neighbouring earthquake to reinforce localization (orange and light-blue dashed lines in Figure 5.3c or 5.3e).

The comparison between the migrating-rupture results for $T = 10\tau_M$ (Figure 5.3b) and $5\tau_M$ (Figure 5.3d) further illustrates that a shorter recurrence interval leads to greater localization.

The second type of migrating-rupture model has the same spatial segmentation of the fault as the first type as shown in Figure 5.3a, but it features temporally clustered

ruptures. Each segment still shares the same T as in the first type of model, but T_m is assumed to be $0.05T$ - half of that in the first type. Starting from the observation segment, it takes only $0.5T$ to rupture all the 10 segments. The entire fault will then stay locked for another $0.5T$. One "super cycle" still takes time T, but all the 10 earthquakes are clustered in the first half. The fifth segment (colour in Figure 5.3a) is still the observation segment. The surface velocities of the clustered-rupture model and the corresponding 2-D model, both with $T = 10\tau_M$, along the profile crossing the centre of the observations segment are shown in Figure 5.4. The 2-D models are identical to those shown in Figure 5.3, but the results are evaluated at a different suite of time steps.

In the earlier phase ($0.1\sim0.5T$) when earthquakes happen at short migration intervals, surface velocities are more localized compared to those in the 2-D model, similar to the results shown in Figure 5.3, especially for those impacted by the approaching events (e.g., orange and light-blue curve in Figure 5.4a). After the quiescent phase of $0.5T$ at the end of the cycle, the surface deformation is still more localized due to the contribution of the recent ruptures (e.g., black curves in Figures 5.4a and 5.4b). Regardless of the clustering, a shorter T still leads to more localized deformation as illustrated by the comparison between Figures 5.4a and 5.4c.

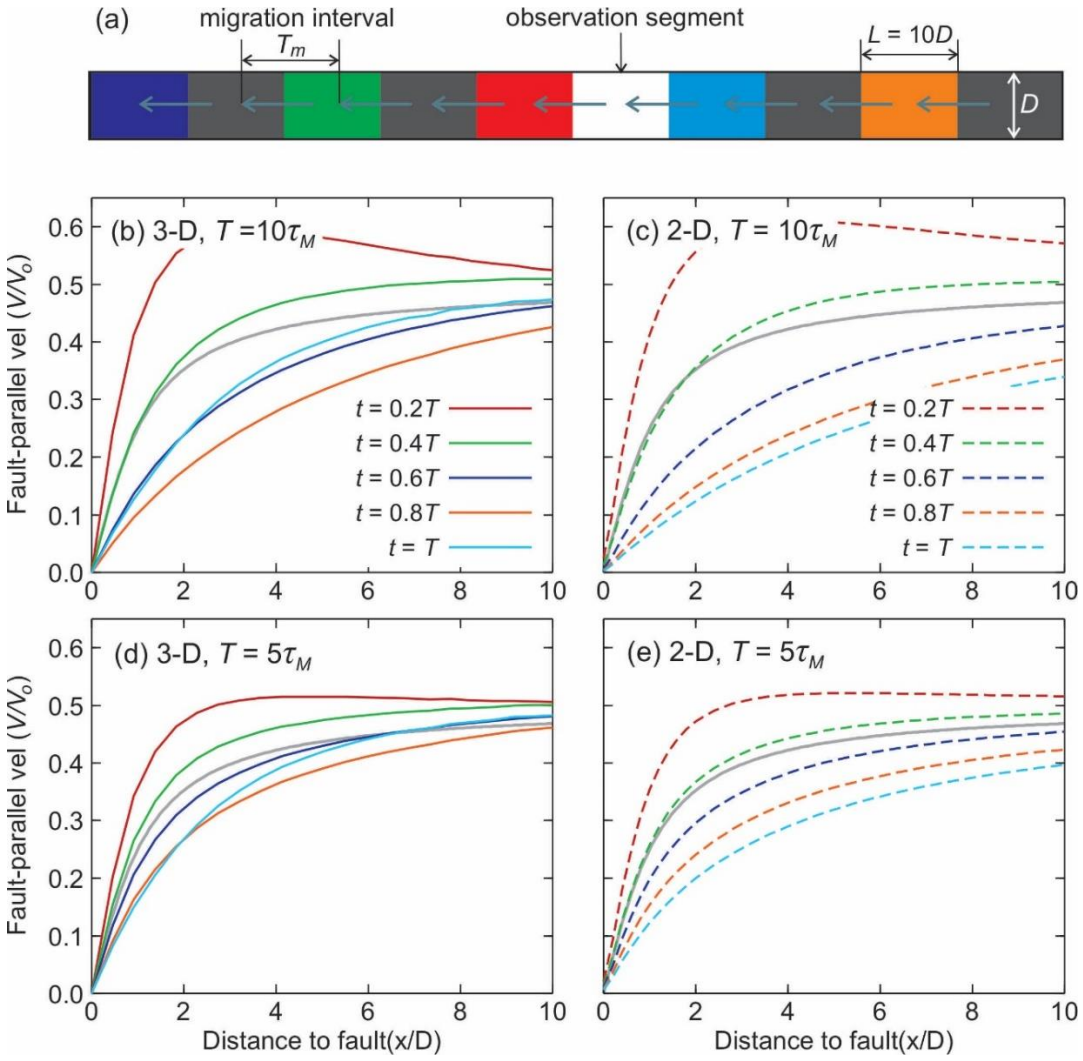

Figure 5.3. Effects of sequential rupture of nearby segments of the same fault on interseismic deformation in a Maxwell model. The elastic dislocation model is shown for comparison (gray line). (a) The 10 segments in this model. From right to left, they rupture one after another with migration interval $T_m = 0.1T$. The sequence repeats after a "super cycle" of 10 events. (b) Deformation along a fault-normal profile crossing the centre of the observation segment for a model with $T = 10\tau_M$. Time counting starts from the last rupture of the observation segment ($t = 0$). Each curve is the velocity distribution $0.1T$ after the rupture of the segment of the same colour as in (a), just before the rupture of the next segment. (c) A 2-D model with $T = 10\tau_M$ (observation segment is infinitely long) for comparison with (b). (d) and (e) The same as (b) and (c), respectively, except for a shorter $T = 5\tau_M$.

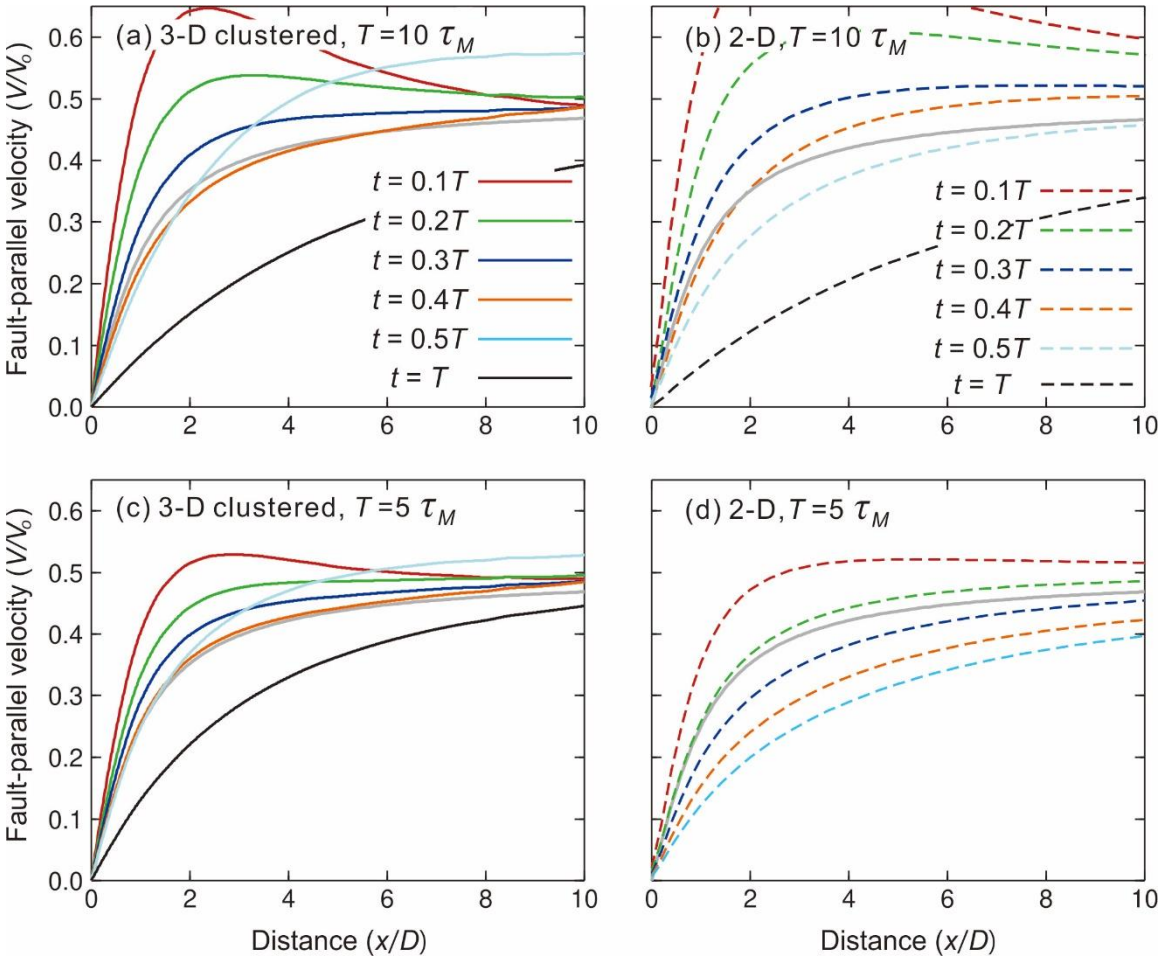

Figure 5.4. Effects of temporally clustered rupture of nearby segments of the same fault on interseismic deformation in a Maxwell model, with the elastic dislocation model shown for comparison (gray line). (a) The 10 segments in this model. From right to left, they rupture one after another with migration interval $T_m = 0.05T$. After the completion of the 10 earthquakes in $0.5T$, the entire fault stays locked for another $0.5T$, before the sequence repeats itself. (b) Deformation along a fault-normal profile crossing the centre of the observation segment for a model with $T = 10\tau_M$. Time counting starts from the last rupture of the observation segment ($t = 0$). Each curve is the velocity distribution $0.05T$ after the rupture of the segment of the same colour as in (a), just before the rupture of the next segment. (c) A 2-D model with $T = 10\tau_M$ (observation segment is infinitely long) for comparison with (b). (d) and (e) The same as (b) and (c), respectively, except for a shorter $T = 5\tau_M$.

The third type of migrating-rupture model is similar to the first type but consists of 5 segments of equal length $L = 20D$. T_m is assumed to be $0.2T$, so that the length of the "super cycle" is still T. Here the 3rd segment is chosen to be the observation segment

(white segment in Figure 5.5a). Time counting follows the same strategy as in the first model but at $0.2T$ after the rupture of the segment of the same colour (before the rupture of the next segment). The comparison between the third type of model and the corresponding 2-D model shows that nearby ruptures still enhance localization (Figures 5.5b and 5.5d), but the effects are less pronounced than the first type (Figure 5.3) because of the longer migration interval T_m. The results illustrate that the reinforcement of localization around the observation segment by neighbouring earthquakes is related to the frequency of neighbouring earthquakes. More frequent rupture of nearby segments reinvigorates the viscous flow in the viscoelastic substrate in a way similar to a shorter recurrence interval in a 2-D fault (Section 4.2), although the flow is 3-D and varies along-strike.

The comparison between the type-III migrating-rupture results for $T = 10\tau_M$ (Figure 5.6b) and $5\tau_M$ (Figure 5.6d) re-emphasize the effects of T is still valid in the 3-D models.

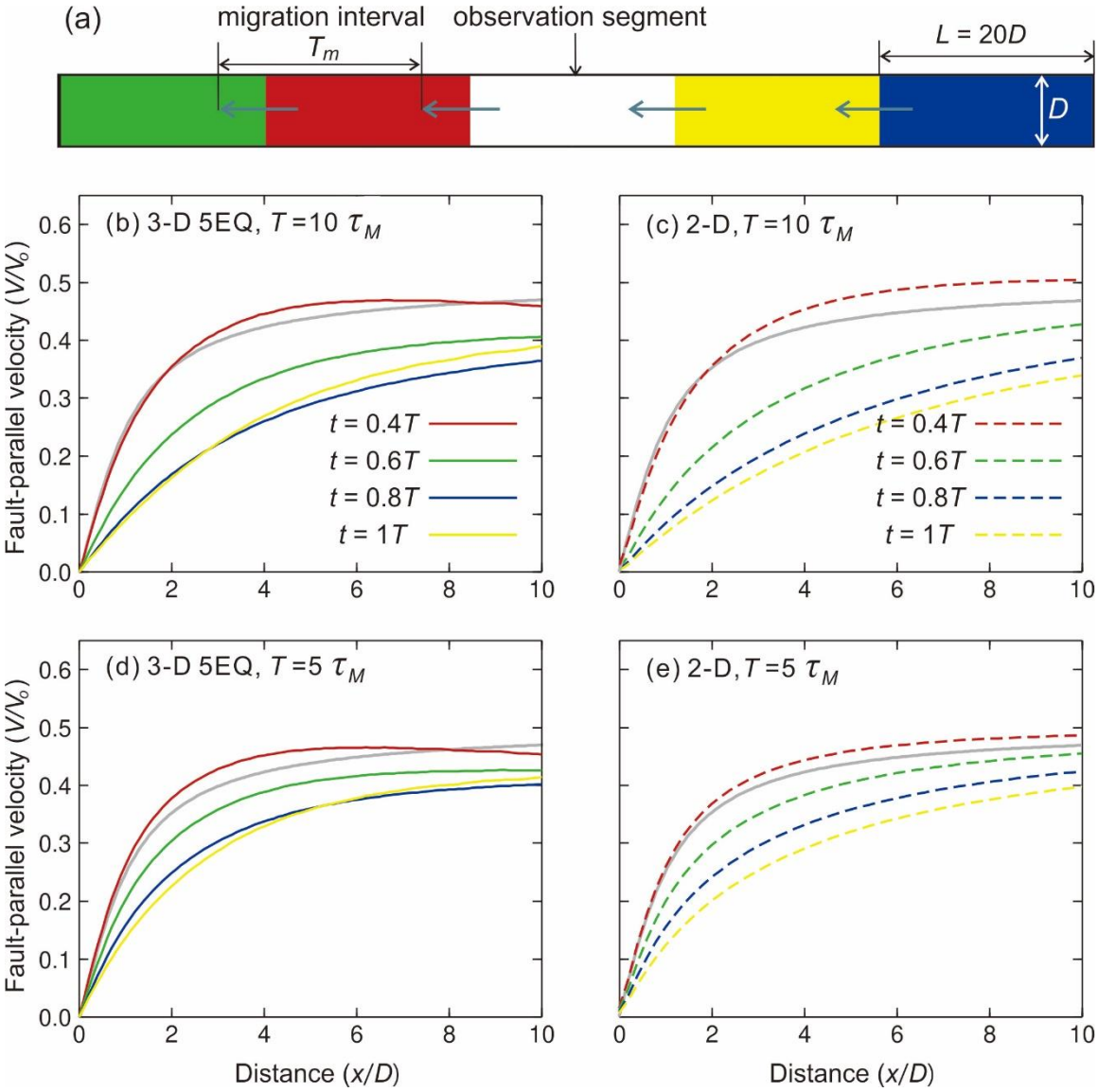

Figure 5.5. Effects of sequential rupture of nearby segments of the same fault on interseismic deformation in a Maxwell model, similar to the models in Figure 5.3 but with only five segments each with a longer rupture length $L = 20D$. The elastic dislocation model is shown for comparison (gray line). (a) The 5 segments in this model. From right to left, they rupture one after another with migration interval $T_m = 0.2T$. The sequence repeats after a "super cycle" of 5 events. (b) Deformation along a fault-normal profile crossing the centre of the observation segment for a model with $T = 10\tau_M$. Time counting starts from the last rupture of the observation segment ($t = 0$). Each curve is the velocity distribution $0.2T$ after the rupture of the segment of the same colour as in (a), just before the rupture of the next segment. (c) A 2-D model with $T = 10\tau_M$ (observation segment is infinitely long) for comparison with (b). (d) and (e) The same as (b) and (c), respectively, except for a shorter $T = 5\tau_M$.

5.3. Neighbouring Segments With Very Frequent Ruptures

Full-rate creep is simply the extreme end-member of localization of deformation, and at distances greater than about $1D$ from the fault, full-rate creeping is similar to the effect of $T \to 0$. Here I use very frequent ruptures to approximate the effect of full-rate creeping and investigate how they affect deformation around a neighbouring locked segment. It is physically implausible to expect sustained full-rate creep against the impedance of neighbouring locked segments, but the model used here is meant to illustrate hypothetical end-member effects.

I consider a central fault segment ($L = 10$ or $30D$) hosting periodic ruptures with a relatively long T (e.g., $T = 5$ or $25\tau_M$) between two segments of infinite length with a very short T (e.g., $T = 0.5\tau_M$). The long segments behave like creeping at full slip rate if observed away from the fault, so that the model can be compared with the first case considered in Section 3.2 (Figure 3.7a). Note there is no fault below D, which differs from the model shown in Figure 3.7a. Models with $T = 5$ and $25\tau_M$ for the central segment are tested, and velocities are shown along a fault-normal profile crossing the centre of this segment.

Comparison with the corresponding 2-D model (dashed lines in Figure 5.6), in which the central segment is infinitely long, delineates that very frequent rupture (representing full-rate creep) of the neighbouring segments can reinforce the localization of deformation around the central segment of a short length (e.g., $L = 10D$), especially in the late-interseismic stage (e.g., blue lines in Figure 5.6). Increasing the length of the central segment weakens the effect, as illustrated by the comparison between the results with $L = 10D$ (Figures 5.6a and 5.6b) and $L = 30D$ (Figures 5.7c and 5.7d). However, when T of the earthquake segment is long (e.g., $T = 25\tau_M$), the neighbouring segments will greatly promote localization of deformation even with a long length ($L = 30D$) (Figure 5.6d).

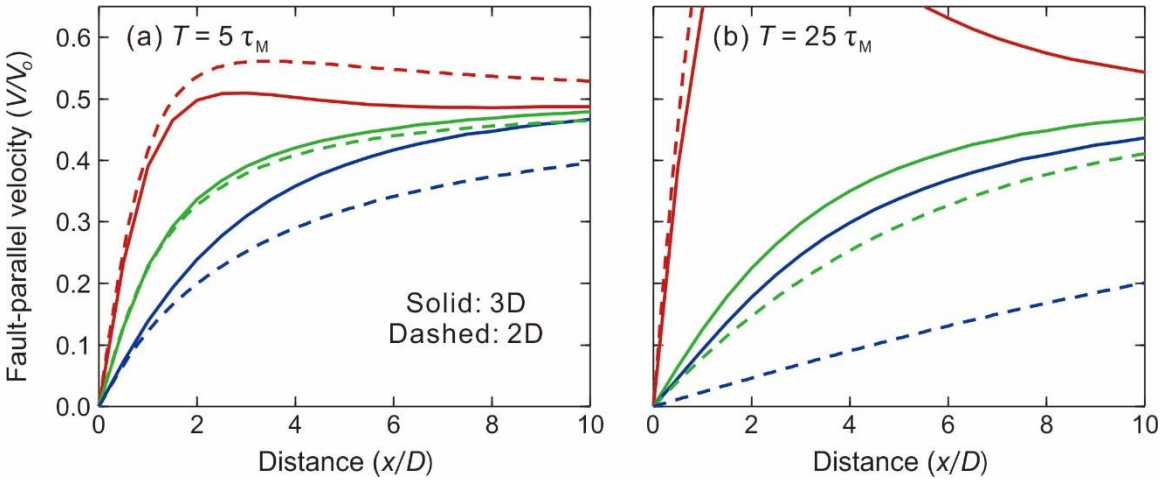

Figure 5.6. Fault-parallel velocities along a fault-normal profile across the central locked segment which is surrounded by two infinitely long and full-rate creeping segments (solid), compared with 2-D models (dashed). Colours represent different stages in an earthquake cycle: red for $t = 0.1T$, green for $t = 0.5T$ and blue for $t = T$. (a) and (b) velocity profiles where the recurrence interval T of the central locked segment is $T = 5$ and $25\tau_M$, respectively, compared with the corresponding 2-D models.

5.4. Earthquake Cycles in Oblique Faults

Real strike-slip faults are usually not perfectly vertical and may accommodate fault-normal motion in addition to strike-slip motion, such as NAF (Şengör et al., 2005), SAF (Molnar, 1992) and XSH (Zheng et al., 2017). Conversely, thrust and normal faults can also host strike-slip motion. To investigate the interseismic deformation associated with oblique faulting, I construct viscoelastic earthquake cycle models similar to what is employed for **Chapter 4** but with oblique faults (Figure 5.7). These models feature identical model geometry as the 2-D strike-slip model (Section 2.1) except for the fault dip. The background deformation field V_1 is modelled by assuming back-slip on the fault (Figure 5.7). The strike-slip component of the slip rate is still denoted V_o, but the thrust rate is denoted V_{o2}. A fault dip of 30° is tested first and will be compared with a 45° dip. A rake angle of 45° is assumed for all the oblique fault models.

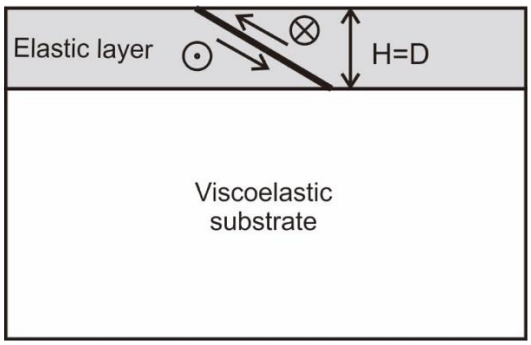

Figure 5.7. Schematic cross-section view of the viscoelastic earthquake cycle model associated with an oblique thrust fault (sinistral strike-slip motion).

Surface deformation of the oblique fault models of 30° dip is shown in Figure 5.8 with $T = 1, 5, 25\ \tau_M$. Velocities are taken along a fault-normal profile and on both sides of the fault since the model is no longer symmetric. As shown in Figures 5.8a and 5.8b, mid- and late-interseismic fault-parallel velocities show a similar trend to purely strike-slip models (Figures 4.1): small T leads to more localized deformation, and large T leads to distributed deformation. This trend also applies to the fault-normal velocities as shown by Figures 5.8c and 5.8d, where the pattern of deformation is still controlled by T when τ_M is fixed. Whatever the fault motion is, an earthquake will induce viscous flow in the fault motion direction. As illustrated in Section 4.2, frequent earthquakes reinvigorate the viscous flow along the fault motion direction which localizes the interseismic deformation. Changing the dip angle does not affect the conclusion, as shown in Figure 5.9.

The small "fluctuation" near the fault trace ($x = 0$) in fault-normal velocity profiles is caused by the lower edge of the dipping fault. If we increase the dip from 30° to 45° while fix the depth of the lower edge, the lower edge and hence the location of the small fluctuation is closer to the fault trace (Figures 5.9c and 5.9d).

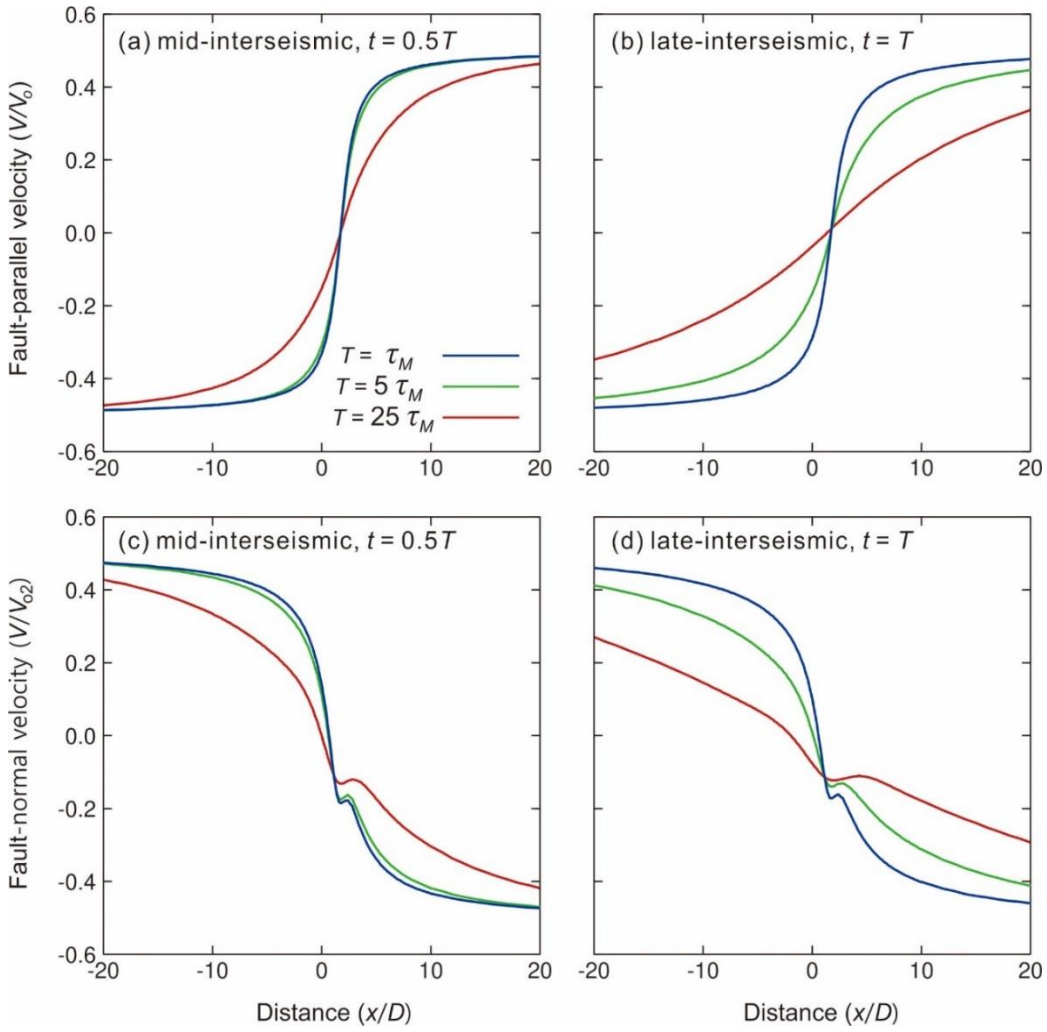

Figure 5.8. Surface velocities along a fault-normal profile crossing the trace of the oblique fault of 30° dip. Models with different T are as labelled in (a). (a) and (b) Mid- and late-interseismic fault-parallel velocity profiles normalized by each model's own strike-slip rate (V_o). (c) and (d) Similar to (a) and (b), respectively, bur for fault-normal velocities. All velocities are normalized by each model's own fault-normal rate V_{o2}.

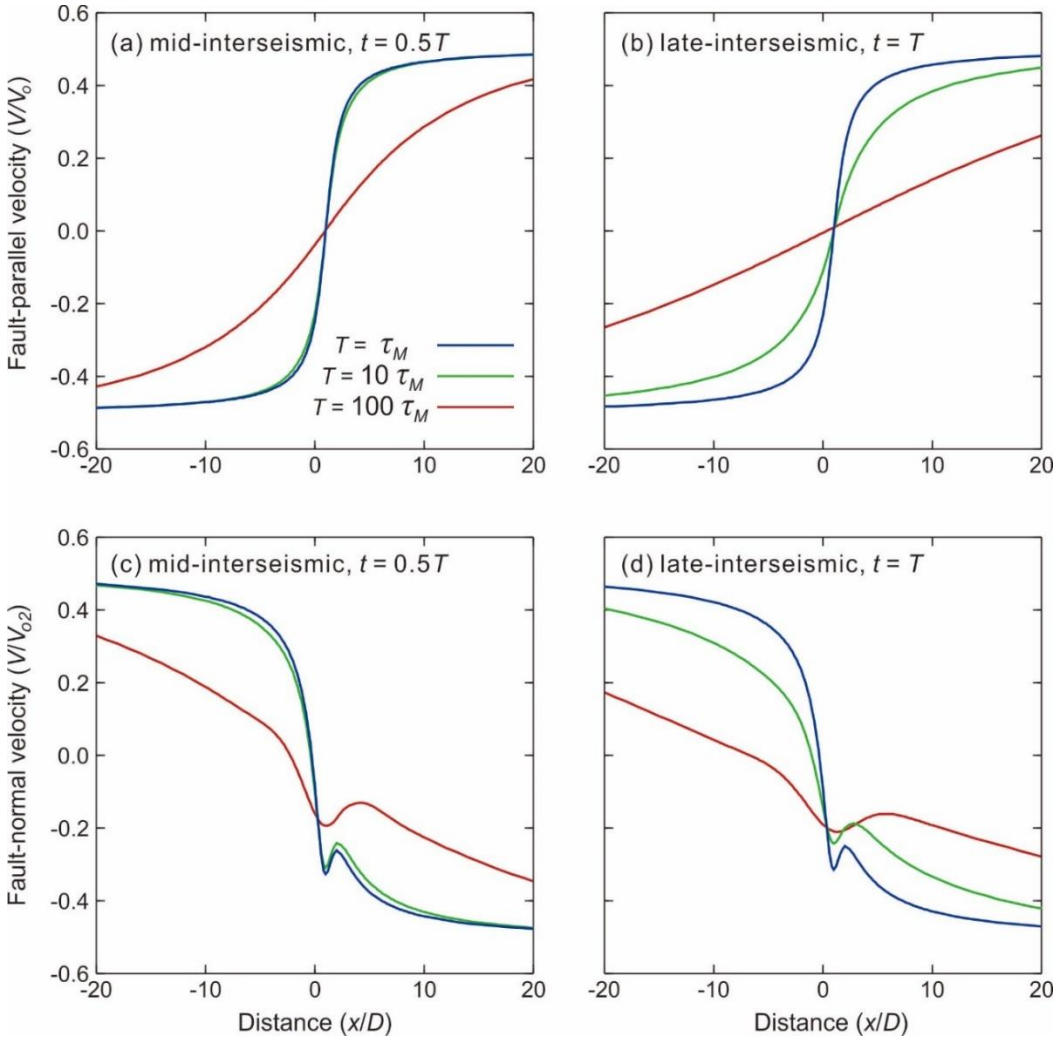

Figure 5.9. Similar to Figure 5.8 but for fault dip of 45°.

The Longmenshan Fault Zone (LFZ) shown in Figure 1.6 is an oblique fault which accommodates both dextral and thrust deformation as described in Section 1.2. It is dipping northwest with an average angle of around 45° (Shen et al., 2009). Fault-parallel velocities around LFZ before the 2008 Wenchuan Earthquake are displayed in Figure 1.6b. The recurrence interval for LFZ is ~4000 yr (Burchfiel et al., 2008; Shen et al., 2009). Assuming $\tau_M = 50$ yr, T should be ~$80\tau_M$. A late-interseismic deformation pattern of an oblique fault model of 45° dip, $T = 80\tau_M$ and $V_o = 1.0$ mm/yr is shown in Figure 5.10a, together with the GNSS data. For the fault-normal velocities, I assume $V_{o2} = 3.0$ mm/yr, the upper limit of the geological rate (Shen et al., 2009). The predicted late-interseismic velocity is the red line shown in Figure 5.10b. Unfortunately, it is

difficult to make a meaning comparison with the data which show very large scatter.

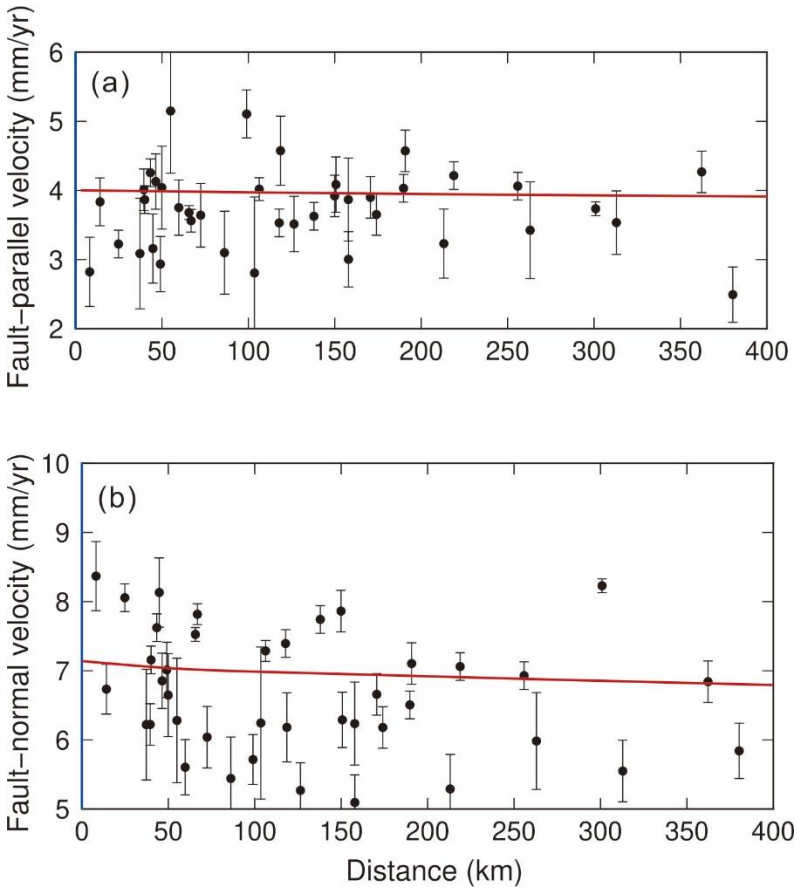

Figure 5.10. Velocities from the oblique fault model and GNSS observations around the Longmenshan Fault (LFZ). The GNSS data are the same as Figure 1.6. Only data east of the fault are shown and the reason is explained in Section 1.2. (a) and (b) Fault-parallel and -normal velocities. The red curves represent the late-interseismic deformation of the oblique fault model with a dip angle of 45°, $T = 80\tau_M$, $V_o = 1$ mm/yr and $V_{o2} = 3$ mm/yr.

Chapter 6. Conclusions and Recommendations for Future Research

6.1. Conclusions

In this thesis study, I have used the simplest models to re-examine the basic mechanics of interseismic deformation around a locked strike-slip fault. First, I have used elastic models to revisit the limited contributions from far-field loading alone. Then I have employed simple Maxwell viscoelastic earthquake-cycle models to explore the contributions from previous earthquakes to driving interseismic deformation. I have also used slightly more complex models involving transient rheology, a shear zone below the fault, limited earthquake rupture length, a migrating rupture sequence, neighbouring segments of frequent earthquake rupture, or oblique faulting to test the effects of various complicating factors. Based on the model results, I draw the following conclusions. Some of these conclusions can also be inferred from earlier viscoelastic earthquake cycle studies, but it is worth reiterating them from a new perspective on the basis of my new results.

1. Past earthquakes localize interseismic deformation by repeatedly reinvigorating localized viscous shear flow beneath the brittle fault (Section 4.2). Far-field tectonic loading alone cannot localize deformation unless some local weakness around or beneath the fault is introduced, but the effect of these local weaknesses is rather limited (**Chapter 3**).

2. The degree of localization decreases with increasing length of the earthquake recurrence interval T (**Chapters 4** and **5**). Decreasing asthenospheric viscosity has the same effect, but lack of significant localization (e.g., Figures 1.4 and 1.5) is often better explained by a long T. Unless the recurrence interval is very short (e.g., $T = \tau_M$), deformation becomes more distributed over the interseismic period. If T is extremely long, past earthquakes have little effect on late-interseismic deformation, similar to a system driven by far-field loading alone.

3. Nearby earthquakes along the same fault may increase localization around a locked segment. If the overall recurrence interval is very long, a nearby recent standalone event (Section 5.1) may cause near-fault perturbation to a background distributed slow deformation (Figure 5.2). If the overall recurrence interval is not very long, frequent

occurrence of nearby events enhances localization around the locked segment (e.g., Section 5.2). If the strike length of the locked segment is very long, the localization of deformation dependents mainly on its own recurrence interval.

4. The mechanism of localization deduced from strike-slip fault models also applies to oblique fault models. T controls the interseismic deformation pattern of not only the fault-parallel component but also the fault-normal component.

5. Natural faults exhibit a wide range of V_o and T. The apparent universality of localized interseismic deformation in the literature may reflect an observational bias: more and better geodetic observations are obtained from high-V_o and short-T faults. Misidentification of mid-interseismic deformation or the effect of a recent nearby earthquake as late-interseismic deformation may add to the bias.

6. Because deformation is localized to different degrees at different stages of the interseismic period, variable geodetic locking depths can be obtained by fitting present deformation data, especially if V_o is not independently constrained.

7. Geodetic observations only constrain velocities over a time window but not how much strain has been accumulated since the last earthquake. Faults that exhibit distributed and slow interseismic velocities today may have already accumulated adequate strain for large earthquakes.

6.2. Recommendations for Future Research

I have only employed the simplest viscoelastic earthquake-cycle models with linear rheology to account for the effects of past events. Future studies can address the effects of more complex but realistic features in the earthquake-cycle models. For example, instead of artificially assuming periodic coseismic ruptures and uniform interseismic locking on the fault, rate-and-state dependent friction law may be a good alternative to investigate the effects of spontaneous earthquakes and stress-controlled locking and creeping.

Although I have used weak shear zone models to simulate the effects of non-linear rheology, it will be important future work to directly incorporate non-linear rheology in earthquake-cycle models with a focus on the effects of T to compare with our weak shear-zone models.

As demonstrated in Section 4.4, the value of geodetic locking depth D_G inferred from equation (1.1) should not be considered as the real D. Factors that can affect the value of D_G, such as recurrence interval or nearby creeping and seismic events, may be responsible for the inconsistency between D_G and seismological determined D. For individual faults, better approximations of T based on combinations of paleoseismic studies and geodetic studies as well as postseismic effects of nearby events are needed to better constrain D for hazard assessment.

In **Chapter 5**, I have used a simple 2-D two-layer model to verify that the effects of T are also applicable to oblique faults. In the real Earth, megathrust faults in subduction zones are the most active faults associated with complex rheological structures. What is learned from this study may give insights to understanding the interseismic deformation around subduction zones. Previous studies employing earthquake cycles tended to focus on vertical deformations (e.g., Sato and Matsu'ura, 1988; Johnson and Tebo, 2018). Future studies may use earthquake-cycle models involving typical structures of subduction zones to investigate the pattern of interseismic horizontal deformation.

Based on a commonly obtained steady-state mantle wedge viscosity value of around 10^{19} Pa s from modelling subduction zone postseismic deformation (Wang et al., 2012), the effect of past megathrust earthquakes is considered unimportant and not included in models of contemporary interseismic deformation, including those for the Cascadia subduction zone (Wang et al., 2012; Li et al., 2018). If the viscosity value continues to increase after the earthquake, the value of 10^{19} Pa s may not be representative of the entire interseismic period. With a greater viscosity, the effect of past earthquakes may not be negligible. This issue should be investigated in future subduction zone earthquake cycle or interseismic models.

Additional effort can be made on observations. Due to limited geodetic observations around locked strike-slip faults with long T and small V_o, I only present two examples of widely-distributed interseismic deformation which are both located in China. Though such faults usually do not show geodetic signals as strong as fast faults, they are also capable of generating destructive earthquakes. More observations around these faults in the future can help improve hazard assessment in these regions.

Bibliography

Al Tarazi, E., Abu Rajab, J., Gomez, F., Cochran, W., Jaafar, R., & Ferry, M. (2011). GPS measurements of near-field deformation along the southern Dead Sea Fault System. *Geochemistry, Geophysics, Geosystems*, *12*(12).

Allen, C. R., Zhuoli, L., Hong, Q., Xueze, W., Huawei, Z., & Weishi, H. (1991). Field study of a highly active fault zone: The Xianshuihe fault of southwestern China. *Geological Society of America Bulletin*, *103*(9), 1178-1199.

Bacques, G., De Michele, M., Raucoules, D., & Aochi, H. (2018). The locking depth of the Cholame section of the San Andreas Fault from ERS2-Envisat InSAR. *Remote Sensing*, *10*(8), 1244.

Barka, A. (1999). The 17 august 1999 Izmit earthquake. *Science*, *285*(5435), 1858-1859.

Bilham, R., et al. (2016). Surface creep on the North Anatolian Fault at Ismetpasa, Turkey, 1944–2016. *Journal of Geophysical Research: Solid Earth*, *121*, 7409–7431.

Bradley, K. E., Feng, L., Hill, E. M., Natawidjaja, D. H., & Sieh, K. (2017). Implications of the diffuse deformation of the Indian Ocean lithosphere for slip partitioning of oblique plate convergence in Sumatra. *Journal of Geophysical Research: Solid Earth*, *122*, 572–591.

Burchfiel, B.C., Royden, L.H., van der Hilst, R.D., Hager, B.H., Chen, Z., King, R.W., Li, C., Lu, J., Yao, H., Kirby, E., 2008. A geological and geophysical context for the Wenchuan earthquake of 12 May 2008, Sichuan, People's Republic of China. GSA Today 18, 4–11. doi:10.1130/GSATG18A.1.

Bürgmann, R., & Dresen, G. (2008). Rheology of the lower crust and upper mantle: Evidence from rock mechanics, geodesy, and field observations. *Annual Review of Earth and Planetary Sciences*, *36*.

Cetin, E., Cakir, Z., Meghraoui, M., Ergintav, S., & Akoglu, A. M. (2014). Extent and distribution of aseismic slip on the Ismetpasa segment of the North Anatolian Fault (Turkey) from Persistent Scatterer InSAR. *Geochemistry, Geophysics, Geosystems*, *15*, 2883–2894.

Chen, Q. F., & Wang, K. (2010). The 2008 Wenchuan earthquake and earthquake prediction in China. *Bulletin of the Seismological Society of America*, *100*(5B), 2840-2857.

Chéry, J. (2008). Geodetic strain across the San Andreas fault reflects elastic plate thickness variations (rather than fault slip rate). *Earth and Planetary Science Letters*, *269*(3-4), 352-365.

Chuang, R. Y., & Johnson, K. M. (2011). Reconciling geologic and geodetic model fault slip-rate discrepancies in Southern California: Consideration of nonsteady mantle flow and lower crustal fault creep. Geology, 39(7), 627-630.

Cohen, S. C., & Kramer, M. J. (1984). Crustal deformation, the earthquake cycle, and models of viscoelastic flow in the asthenosphere. *Geophysical Journal International*, *78*(3), 735-750.

Dolan, J. F., & Meade, B. J. (2017). A comparison of geodetic and geologic rates prior to large strike-slip earthquakes: A diversity of earthquake cycle behaviors?. *Geochemistry, Geophysics, Geosystems, 18*, 4426–4436.

Ergintav, S., McClusky, S., Hearn, E., Reilinger, R., Cakmak, R., Herring, T., ... & Tari, E. (2009). Seven years of postseismic deformation following the 1999, M= 7.4 and M= 7.2, Izmit-Düzce, Turkey earthquake sequence. *Journal of Geophysical Research: Solid Earth*, *114*(B7).

Ferry, M., Meghraoui, M., Abou Karaki, N., Al-Taj, M., Amoush, H., Al-Dhaisat, S., & Barjous, M. (2007). A 48-kyr-long slip rate history for the Jordan Valley segment of the Dead Sea Fault. *Earth and Planetary Science Letters*, *260*(3-4), 394-406.

Gan, W., Zhang, P., Shen, Z. K., Niu, Z., Wang, M., Wan, Y., ... & Cheng, J. (2007). Present-day crustal motion within the Tibetan Plateau inferred from GPS measurements. *Journal of Geophysical Research: Solid Earth*, *112*(B8).

Hamiel, Y., Piatibratova, O., & Mizrahi, Y. (2016). Creep along the northern Jordan Valley Section of the Dead Sea Fault. *Geophysical Research Letters*, *43*, 2492–2501.

Hamiel, Y., Piatibratova, O., Mizrahi, Y., Nahmias, Y., & Sagy, A. (2018). Crustal deformation across the Jericho Valley section of the Dead Sea Fault as resolved by detailed field and geodetic observations. *Geophysical Research Letters*, *45*(7), 3043-3050.

Hearn, E. H., McClusky, S., Ergintav, S., & Reilinger, R. E. (2009). Izmit earthquake postseismic deformation and dynamics of the North Anatolian Fault Zone. *Journal of Geophysical Research: Solid Earth*, *114*(B8).

Hearn, E. H., & Thatcher, W. R. (2015). Reconciling viscoelastic models of postseismic and interseismic deformation: Effects of viscous shear zones and finite length ruptures. *Journal of Geophysical Research: Solid Earth*, *120*(4), 2794-2819.

Hetland, E. A., & Hager, B. H. (2005). Postseismic and interseismic displacements near a strike-slip fault: A two-dimensional theory for general linear viscoelastic

rheologies. *Journal of Geophysical Research: Solid Earth*, *110*(B10).

Hetland, E. A., & Hager, B. H. (2006). Interseismic strain accumulation: Spin-up, cycle invariance, and irregular rupture sequences. *Geochemistry, Geophysics, Geosystems*, *7*(5).

Hu, Y. (2004). 2-D and 3-D viscoelastic finite element models for subduction earthquake deformation. M.Sc. thesis, University of Victoria, Victoria, British Columbia, Canada.

Hu, Y. (2011). Deformation Processes in Great Subduction Zone Earthquake Cycles, PhD thesis, University of Victoria, Victoria, British Columbia, Canada.

Hu, Y., & Freymueller, J. T. (2019). Geodetic Observations of Time-Variable Glacial Isostatic Adjustment in Southeast Alaska and Its Implications for Earth Rheology. *Journal of Geophysical Research: Solid Earth*, *124*(9), 9870-9889.

Huang, W. (1993). Morphologic patterns of stream channels on the active Yishi Fault, southern Shandong Province, Eastern China: implications for repeated great earthquakes in the Holocene. *Tectonophysics*, *219*(4), 283-304.

Hussain, E., Wright, T. J., Walters, R. J., Bekaert, D. P., Lloyd, R., & Hooper, A. (2018). Constant strain accumulation rate between major earthquakes on the North Anatolian Fault. *Nature communications*, *9*(1), 1392.

James, T. S., Clague, J. J., Wang, K., & Hutchinson, I. (2000). Postglacial rebound at the northern Cascadia subduction zone. *Quaternary Science Reviews*, *19*(14-15), 1527-1541.

Jiang, W., Zhang, J., Han, Z., Tian, T., Jiao, Q., Wang, X., & Jiang, H. (2017). Characteristic slip of strong earthquakes along the Yishu fault zone in east China evidenced by offset landforms. *Tectonics*, *36*(10), 1947-1965.

Johnson, K. M. (2013). Slip rates and off-fault deformation in Southern California inferred from GPS data and models. Journal of Geophysical Research: Solid Earth, 118, 5643-5664.

Johnson, K. M., & Segall, P. (2004). Viscoelastic earthquake cycle models with deep stress-driven creep along the San Andreas fault system. Journal of Geophysical Research: Solid Earth, 109, B10403, doi:10.1029/2004JB003096.

Johnson, K. M., & Tebo, D. (2018). Capturing 50 years of postseismic mantle flow at Nankai subduction zone. *Journal of Geophysical Research: Solid Earth*, *123*(11), 10-091.

Jolivet, R., Cattin, R., Chamot-Rooke, N., Lasserre, C., & Peltzer, G. (2008). Thin-plate modelling of interseismic deformation and asymmetry across the Altyn Tagh fault zone. *Geophysical Research Letters*, *35*(2).

Kaneko, Y., Fialko, Y., Sandwell, D. T., Tong, X., & Furuya, M. (2013). Interseismic deformation and creep along the central section of the North Anatolian fault (Turkey): InSAR observations and implications for rate-and-state friction properties. *Journal of Geophysical Research: Solid Earth*, *118*, 316–331.

Lachenbruch, A. H., & Sass, J. H. (1980). Heat flow and energetics of the San Andreas fault zone. *Journal of Geophysical Research: Solid Earth*, *85*(B11), 6185-6222.

Li, S., Wang, K., Wang, Y., Jiang, Y., & Dosso, S. E. (2018). Geodetically inferred locking state of the Cascadia megathrust based on a viscoelastic Earth model. *Journal of Geophysical Research: Solid Earth*, *123*(9), 8056-8072.Li, V. C., & Rice, J. R. (1987). Crustal deformation in great California earthquake cycles. Journal of Geophysical Research: Solid Earth, 92(B11), 11533-11551.

Li, Y., Qu, C., Shan, X., Song, X., Zhang, G., Gan, W., ... & Wang, Z. (2015). Deformation of the Haiyuan-Liupanshan fault zone inferred from the denser GPS observations. *Earthquake Science*, *28*(5-6), 319-331.

Lindsey, E. O., Sahakian, V. J., Fialko, Y., Bock, Y., Barbot, S., & Rockwell, T. K. (2014). Interseismic strain localization in the San Jacinto fault zone. *Pure and Applied Geophysics*, *171*(11), 2937-2954.

Ma, B., Su, G., Hou, Z. H., & Shu, S. (2005). Late Quaternary slip rate in the central part of the Longmenshan fault zone from terrace deformation along the Minjiang River. *Seismology and Geology*, *27*(2), 234-242.

Meade, B. J., Klinger, Y., & Hetland, E. (2013). Inference of multiple earthquake-cycle relaxation timescales from irregular geodetic sampling of interseismic deformation. *Bulletin of the Seismological Society of America, 103*, 2824–2835.

Molnar, P. (1992). Brace-Goetze strength profiles, the partitioning of strike-slip and thrust faulting at zones of oblique convergence, and the stress-heat flow paradox of the San Andreas fault. In *International Geophysics* (Vol. 51, pp. 435-459). Academic Press.

Molnar, P., & Dayem, K. E. (2010). Major intracontinental strike-slip faults and contrasts in lithospheric strength. *Geosphere*, *6*(4), 444-467.

Nur, A., & Mavko, G. (1974). Postseismic viscoelastic rebound. *Science*, *183*(4121), 204-

206. https://doi.org/10.1126/science.183.4121.204

Okada, Y. (1985), Surface deformation due to shear and tensile faults in a half-space, *Bulletin of the Seismological Society of America*, *75*, 1135-1154.

Okada, Y. (1992), Internal deformation due to shear and tensile faults in a half-space, *Bulletin of the Seismological Society of America*, *82*, 1,018-1,040.

Papaleo, E., Cornwell, D., & Rawlinson, N. (2018). Constraints on North Anatolian Fault Zone width in the crust and upper mantle from S wave teleseismic tomography. *Journal of Geophysical Research: Solid Earth*, *123*(4), 2908-2922.

Peltier, W. R., Wu, P., & Yuen, D. A. (1981). The viscosities of the Earth's mantle. *Anelasticity in the Earth*, *4*, 59-77.

Pollitz, F. F. (1992), Postseismic relaxation theory on the spherical Earth, *Bulletin of the Seismological Society of America*, *82*, 422-453.

Pollitz, F. F. (1997), Gravitational-viscoelastic postseismic relaxation on a layered spherical Earth, *Journal of Geophysical Research*, *102*, 17,921-17,941.

Pollitz, F. F. (2003). Transient rheology of the uppermost mantle beneath the Mojave Desert, California. *Earth and Planetary Science Letters*, *215*(1-2), 89-104.

Pollitz, F. F. (2005). Transient rheology of the upper mantle beneath central Alaska inferred from the crustal velocity field following the 2002 Denali earthquake. *Journal of Geophysical Research: Solid Earth*, *110*(B8).

Reilinger, R., McClusky, S., Vernant, P., Lawrence, S., Ergintav, S., Cakmak, R., ... & Nadariya, M. (2006). GPS constraints on continental deformation in the Africa-Arabia-Eurasia continental collision zone and implications for the dynamics of plate interactions. *Journal of Geophysical Research: Solid Earth*, *111*(B5).

Ryder, I., Bürgmann, R., & Pollitz, F. (2011). Lower crustal relaxation beneath the Tibetan Plateau and Qaidam Basin following the 2001 Kokoxili earthquake. *Geophysical Journal International*, *187*(2), 613-630.

Savage, J. C. (2000). Viscoelastic-coupling model for the earthquake cycle driven from below. *Journal of Geophysical Research: Solid Earth*, *105*(B11), 25525-25532.

Sadeh, M., Hamiel, Y., Ziv, A., Bock, Y., Fang, P., & Wdowinski, S. (2012). Crustal deformation along the Dead Sea Transform and the Carmel Fault inferred from 12 years of GPS measurements. *Journal of Geophysical Research: Solid Earth*, *117*(B8).

Savage, J. C., & Burford, R. O. (1973). Geodetic determination of relative plate motion in central California. *Journal of Geophysical Research*, *78*, 832–845.

Savage, J. C., & Prescott, W. H. (1978a). Asthenosphere readjustment and the earthquake cycle. *Journal of Geophysical Research: Solid Earth*, *83*(B7), 3369-3376.

Savage, J. C., & Prescott, W. H. (1978b). Comment [on "Nonlinear stress propagation in the Earth's upper mantle" by HJ Melosh]. *Journal of Geophysical Research: Solid Earth*, *83*(B10), 5005-5007.

Şengör, A. M. C., Tüysüz, O., Imren, C., Sakınç, M., Eyidoğan, H., Görür, N., ... & Rangin, C. (2005). The North Anatolian fault: A new look. *Annual Review of Earth Planetary Sciences*, *33*, 37-112.

Shen, L., Hooper, A., Elliott, J., & Wright, T. (2018). Interseismic deformation along the Altyn Tagh fault, Tibet: Implications for shallow creep. In *EGU General Assembly Conference Abstracts* (Vol. 20, p. 1191).

Shen, Z. K., Lü, J., Wang, M., & Bürgmann, R. (2005). Contemporary crustal deformation around the southeast borderland of the Tibetan Plateau. *Journal of Geophysical Research: Solid Earth*, *110*(B11).

Shen, Z. K., Sun, J., Zhang, P., Wan, Y., Wang, M., Bürgmann, R., ... & Wang, Q. (2009). Slip maxima at fault junctions and rupturing of barriers during the 2008 Wenchuan earthquake. *Nature geoscience*, *2*(10), 718-724.

Shimamoto, T., & Noda, H. (2014). A friction to flow constitutive law and its application to a 2-D modelling of earthquakes. *Journal of Geophysical Research: Solid Earth*, *119*(11), 8089-8106.

Smith, B., & Sandwell, D. (2004). A three-dimensional semianalytic viscoelastic model for time-dependent analyses of the earthquake cycle. *Journal of Geophysical Research: Solid Earth*, *109*(B12).

Smith-Konter, B. R., Sandwell, D. T., & Shearer, P. (2011). Locking depths estimated from geodesy and seismology along the San Andreas Fault System: Implications for seismic moment release. *Journal of Geophysical Research: Solid Earth*, *116*(B6).

Sylvester, A. G. (1988). Strike-slip faults. *Geological Society of America Bulletin*, *100*(11), 1666-1703.

Takeuchi, C. S., & Fialko, Y. (2012). Dynamic models of interseismic deformation and stress transfer from plate motion to continental transform faults. *Journal of*

Geophysical Research: Solid Earth, *117*, B05403.

Tao, W., & Shen, Z. (2008). Heat flow distribution in Chinese continent and its adjacent areas. *Progress in Natural Science*, *18*(7), 843-849.

Tatar, O., Poyraz, F., Gürsoy, H., Cakir, Z., Ergintav, S., Akpınar, Z., ... & Polat, A. (2012). Crustal deformation and kinematics of the Eastern Part of the North Anatolian Fault Zone (Turkey) from GPS measurements. *Tectonophysics*, *518*, 55-62.

Thatcher, W. (1975). Strain accumulation and release mechanism of the 1906 San Francisco earthquake. *Journal of Geophysical Research*, *80*(35), 4862-4872.

Titus, S. J., DeMets, C., & Tikoff, B. (2006). Thirty-five-year creep rates for the creeping segment of the San Andreas Fault and the effects of the 2004 M 6.0 Parkfield earthquake: Constraints from alignment arrays, continuous GPS, and creepmeters. *Bulletin of Seismological Society of America*, *96*, S250–S268.

Titus, S. J., Dyson, M., DeMets, C., Tikoff, B., Rolandone, F., & Bürgmann, R. (2011). Geologic versus geodetic deformation adjacent to the San Andreas fault, central California. *Geological Society of America Bulletin*, *123*, 794–820.

Traoré, N., Le Pourhiet, L., Frelat, J., Rolandone, F., & Meyer, B. (2014). Does interseismic strain localization near strike-slip faults result from boundary conditions or rheological structure?. *Geophysical Journal International*, *197*(1), 50-62.

Turcotte, D. L., & Spence, D. A. (1974). An analysis of strain accumulation on a strike slip fault. Journal of Geophysical Research, 79 (29), 4407-4412.

Vaghri, A., & Hearn, E. H. (2012). Can lateral viscosity contrasts explain asymmetric interseismic deformation around strike-slip faults?. *Bulletin of the Seismological Society of America*, *102*(2), 490-503.

Vernant, P. (2015). What can we learn from 20 years of interseismic GPS measurements across strike-slip faults?. *Tectonophysics*, *644*, 22-39.

Wang, F., Wang, M., Wang, Y., & Shen, Z. K. (2015). Earthquake potential of the Sichuan-Yunnan region, western China. *Journal of Asian Earth Sciences*, *107*, 232-243.

Wang, H., Wright, T. J., & Biggs, J. (2009). Interseismic slip rate of the northwestern Xianshuihe fault from InSAR data. *Geophysical Research Letters*, *36*(3).

Wang, K., Hu, Y., & He, J. (2012). Deformation cycles of subduction earthquakes in a

viscoelastic Earth. Nature, 484(7394), 327–332.

Wang, M., & Shen, Z.-K. (2020). Present-day crustal deformation of continental China derived from GPS and its tectonic implications. *Journal of Geophysical Research: Solid Earth*, *125*, e2019JB018774.

Watts, A. B., & Burov, E. B. (2003). Lithospheric strength and its relationship to the elastic and seismogenic layer thickness. *Earth and Planetary Science Letters*, *213*(1-2), 113-131.

Wright, T. J., Elliott, J. R., Wang, H., & Ryder, I. (2013). Earthquake cycle deformation and the Moho: Implications for the rheology of continental lithosphere. *Tectonophysics*, *609*, 504-523.

Yamasaki, T., Wright, T. J., & Houseman, G. A. (2014). Weak ductile shear zone beneath a major strike-slip fault: Inferences from earthquake cycle model constrained by geodetic observations of the western North Anatolian Fault Zone. *Journal of Geophysical Research: Solid Earth, 119*, 3678–3699.

Yu, Z., Zhang, P., Min, W., Wei, Q., & Liu, Y. (2018). Late Holocene slip rate and average recurrence interval of great earthquakes on the Shangzhi segment of the Yilan-Yitong Fault Zone, northeastern China: Constraints from paleo-earthquakes and historical written records. *Island Arc*, *27*(1), e12231.

Zeng, Y., & Shen, Z. K. (2014). Fault network modelling of crustal deformation in California constrained using GPS and geologic observations. *Tectonophysics*, *612*, 1-17.

Zhang, X., & Sagiya, T. (2018). Intraplate Strike-Slip Faulting, Stress Accumulation, and Shear Localization of a Crust-Upper Mantle System With Nonlinear Viscoelastic Material. *Journal of Geophysical Research: Solid Earth*, *123*(10), 9269-9285.

Zheng, G., Wang, H., Wright, T. J., Lou, Y., Zhang, R., Zhang, W., ... & Wei, N. (2017). Crustal deformation in the India-Eurasia collision zone from 25 years of GPS measurements. *Journal of Geophysical Research: Solid Earth*, *122*(11), 9290-9312.

Zielke, O., Arrowsmith, J. R., Ludwig, L. G., & Akçiz, S. O. (2010). Slip in the 1857 and earlier large earthquakes along the Carrizo Plain, San Andreas fault. Science, 327(5969), 1119–1122.